Establishment of the Yucatan Minipig as a Preclinical Animal Model for Carpal Instabilities in the Human Wrist

by

Quianna Vaughan

B.S., College of Engineering and Computing at Florida International University, 2021

A dissertation submitted in partial fulfillment of the requirements for the degree of Doctor of Philosophy in the Biomedical Engineering program, a joint program in the Division of Biology and Medicine and the School of Engineering at Brown University

Providence, Rhode Island

May 24th, 2026

This dissertation by Quianna Vaughan is accepted in its present form by the Biomedical Engineering program, a joint program in the Division of Biology and Medicine and the School of Engineering, as satisfying the dissertation requirement for the degree of Doctor of Philosophy.

Date 04/22/2026 | 7:15 AM EDT Signed by: Joseph J. Crisco 3A9C5AE99F484B9...

Joseph J. Crisco, Advisor

Recommended to the Graduate Council

Date 04/21/2026 | 2:20 PM EDT DocuSigned by: Eric Darling 46DB889F981A404...

Eric M. Darling, Reader

Date 04/21/2026 | 2:23 PM EDT DocuSigned by: Braden Fleming 2D68E442E7F6430...

Braden C. Fleming, Reader

Date 04/21/2026 | 2:29 PM EDT Signed by: Haneesh Kesari 17AF9E4DB65E423...

Haneesh Kesari, Reader

Approved by the Graduate Council

Date _____

David P. Lindstrom, Dean of the Graduate School

Curriculum Vitae

Education

Brown University, Providence, RI, USA May 2026 (Defended April 2026)
Ph.D., Biomedical Engineering

Florida International University, Miami, FL, USA April 2021
B.S., Biomedical Engineering

Research Experience

Bioengineering Laboratory Department of Orthopaedics,
Brown University
Primary Investigator: Dr. Joseph J. Crisco
September 2021- Present

Establishing the Yucatan Minipig (YMP) Carpus as a Preclinical Animal Model for the Human Wrist

Microscopic Histology

- Utilized OARSI guidelines to assess proximal and distal articulations of the radial carpal bone (RCB) and opposing articular surfaces in the YMP after ligament injury or small bone replacement to evaluate cartilage damage after 12 weeks. These findings are under review by the Journal of Osteoarthritis and Cartilage OPEN.

Biomechanics of the YMP Carpus

- Analyzed the biomechanics of the YMP RCB after ligament transection, RCB extraction, and re-stabilization with a hemiarthroplasty (RCBH) using a KUKA robotic simulator to compare range of motion, neutral zone, final stiffness, and RCB rotation across each condition. These findings are under review by the Journal of Biomechanics.

YMP Carpus Osteophyte Volume and Joint Space

- Computed osteophyte volume and joint distance from micro-CT images of carpal bones in the contralateral and surgical limbs of YMP's at 12 weeks postoperatively. These findings are under review by the Journal of Osteoarthritis and Cartilage OPEN.

YMP Spatiotemporal Gait Analysis

- Conducted gait analysis on YMP's using a Tekscan pressure mat to assess biomechanical changes post-ligament injury and RCBH implantation at 0, 3, 6, 9, and 12 weeks postoperatively. Metrics recorded included maximum strike force, peak pressure, and impulse to evaluate gait asymmetry. These findings are under review by the Journal of Osteoarthritis and Cartilage OPEN.

Radial Carpal Bone (RCB) Implant

- Developed a cobalt chrome small bone arthroplasty for the RCB in YMPs to investigate post-implantation effects on cartilage degradation, bone morphology, and animal gait. Implant development and validation was published in Institution of Mechanical Engineers, Part H: Journal of Engineering in Medicine.

Soft Tissue Artifacts in the Wrist

- Conducted biomechanics research analyzing differences in center of rotation, contact patterns, and ulnar variance between healthy wrists, total wrist arthroplasty, and distal radioulnar joints affected by soft tissue artifacts; utilized biplanar video radiography and optical motion capture to create 3D wrist models during flexion, extension, and rotational movements.

Medical Photonics Laboratory, Florida International University
Primary Investigator: Dr. Jessica Ramella-Roman
August 2020-April 2021

Optical Phantoms for the Skin

- Conducted tissue engineering research to develop advanced skin phantoms by evaluating decellularization and tissue-clearing methods, performing Monte Carlo simulations to compare optical scattering and absorption with conventional phantoms, and executing decellularization procedures on rat skin flaps to preserve vascular and 3D skin structures.

Projects

Rhode Island Hospital Orthopaedic Foundation, *Providence, RI*
May 2022- July 2024

Biomechanical Evaluation of an Orthobiologic in a Chicken Flexor Tendon Repair Model

- Evaluated tendon healing in a chicken flexor tendon repair model using gliding and uniaxial tensile testing with an Instron ElectroPuls E3000 testing machine to assess mechanical properties following gene therapy treatment.

Mechanical Testing of Relaxin treated Rat ACL

- Designed custom test fixtures in Solidworks and performed pull-to-failure mechanical testing with an Instron ElectroPuls E1000 on rat ACLs to investigate the relationship between Relaxin and ligament biomechanics.

Mechanical Testing of Anchor Line Fixation System and Predicate Devices

- Evaluated the mechanical performance of orthopedic bone anchor fixation systems using cyclic loading and post-cyclic uniaxial pullout testing with an Instron ElectroPuls E1000 in accordance with ASTM standards and FDA guidance.

Biomechanical Evaluation of a Laxity-Minimizing Suture in a Cadaveric Supraspinatus Model

- Assessed rotator cuff repair performance in a human cadaveric shoulder model by quantifying contact pressure and contact area using a TekScan 5800 thin-film pressure sensors.

Mechanical Testing of Surgical Mesh Tack and Tendon Anchor

- Evaluated the mechanical performance of surgical mesh tacks and tendon anchors through uniaxial tensile and shear strength testing using an Instron ElectroPuls E10000 in accordance with ASTM standards to assess comparative device performance.

Mechanical Testing of Cranial Bone Screws

- Performed ASTM-compliant insertion/removal torque and torque-to-failure with an MTS Bionix torsion test system, and axial pull-out testing with an Instron ElectroPuls E1000 to evaluate the mechanical performance of cranial bone screws.

Biomechanical Evaluation of Bone Samples from Hormone Therapy-Treated Rats

- Conducted biomechanical testing of rat bones following hormone therapy using three-point bend, femoral head compression, and vertebral compression-to-failure methods.

Florida International University, *Miami, FL*

Emergency Cervical Collar with XPF Auxetic Foam Fall 2020- Spring 2021
Team Leader

- Designed and prototyped an emergency cervical collar to mitigate excessive head and neck motion, validating feasibility through verification and validation testing using auxetic foam.

Computational Model of the Cardiovascular System
Spring 2019

- Solved differential equation models of the circulatory system to simulate pressure, flow, and volume, predicting cardiovascular responses to disorders such as cardiac arrest, stenosis, and anxiety.

First Author Publications

Vaughan QM, Morton AM, Moore D, Akelman E, Crisco JJ. Development of small bone implants using a mean shape bone in a porcine model for carpal bone replacement. *Proc Inst Mech Eng H*. 2025;239(8):755-765. doi:10.1177/09544119251355382

Vaughan QM, Morton AM, Moore DC, Molino J, Akelman E, Crisco JJ. Small Bone Replacement Leads to Greater Gait Asymmetry, Cartilage Damage, and Osteophyte Formation Than Ligament injury in a Porcine Wrist Model. (UNDER REVIEW: *Osteoarthritis and Cartilage OPEN).*

Vaughan QM, Badida R, Molino J, Akelman E, Crisco JJ. In Vitro Biomechanics of the Yucatan Minipig Carpus After Ligament Transection, Bone Resection, and Small Bone Replacement. (PENDING SUBMISSION: *Journal of Biomechanics).*

Co-Authored Publications

Altieri MK, Badida R, **Vaughan QM**, Molino J, Akelman E, Crisco JJ. Biomechanical evaluation of the porcine carpus as a potential preclinical animal model for the human carpus. *J Biomech*. 2024;177:112429. doi:10.1016/j.jbiomech.2024.112429

Conference Presentations

Vaughan, Q.M., Morton, A.M., Moore, D.C., Molino, J., Akelman, E., Crisco, J.J. (2026, March) Osteophyte Growth and Joint Space Distance in the Yucatan Minipig Carpus: An Animal Model for Ligament Injury and Small Bone Replacement. [Poster presentation]. Orthopaedic Research Society Annual Meeting, Charlotte, NC.

Vaughan, Q.M., Morton, A.M., Moore, D.C., Molino, J., Akelman, E., Crisco, J.J. (2025, November) Osteophyte Growth and Joint Space Distance in the Yucatan Minipig Carpus: An Animal Model for Ligament Injury and Small Bone Replacement. [E-Poster presentation]. Brown University Health Research Day, Providence, RI.

Vaughan, Q.M., Morton, A.M., Moore, D.C., Crisco, J.J. (2025, August) Development of Small Bone Implants in a Porcine Model for Carpal Bone Replacement. [Poster presentation]. American Society of Biomechanics Annual Meeting, Pittsburgh, PA.

Vaughan, Q.M., Badida, R., Morton, A.M., Moore, D.C., Crisco, J.J. (2025, February) Biomechanics of the Yucatan Minipig Wrist After Carpal Bone Resection. [Poster presentation]. Orthopaedic Research Society Annual Meeting, Phoenix, AZ.

Vaughan, Q.M., Morton, A.M., Moore, D.C., Crisco, J.J. (2025, February) Can Age and Weight Predict Radial Carpal Bone Size in a Porcine Forelimb Model? [Poster presentation]. Orthopaedic Research Society Annual Meeting, Phoenix, AZ.

Vaughan, Q.M., Morton, A.M., Moore, D.C., Crisco, J.J. (2024, November) Can Age and Weight Predict Radial Carpal Bone Size in a Porcine Forelimb Model? [E-Poster presentation]. Rhode Island Hospital Research Day, Providence, RI.

Altieri, M.K., Badida, R., **Vaughan, Q.M**., Akelman, E., Crisco, J.J. (2024, August) Porcine Carpal Biomechanics: Feasibility as a Preclinical Animal Model for the Human Wrist Joint. [Short talk presentation]. International Society of Technology in Arthroplasty Annual Meeting, Nashville, TN.

Vaughan, Q.M., Sordilla, S.L., Morton, A.M., Moore, D.C., Akelman, E., Crisco, J.J. (2024, February) The Yucatan Minipig as a Potential Preclinical Animal Model for Carpal Bone Arthroplasty [Poster presentation]. Orthopaedic Research Society Annual Meeting, Long Beach, CA.

Vaughan, Q.M., Morton, A.M., Hayda, T., Crisco, J.J. (2023, October) Skin Motion Artifact of Radiopaque Bead Tracking Relative to Markerless Bone Tracking [E-Poster presentation]. Rhode Island Hospital Research Day, Providence, RI.

Vaughan, Q.M., Morton, A.M., Hayda, T., Crisco, J.J. (2023, February) Skin Motion Artifact of Radiopaque Bead Tracking Relative to Markerless Bone Tracking [Poster presentation]. Orthopaedic Research Society Annual Meeting, Dallas, TX.

Vaughan, Q.M., Morton, A.M., Hayda, T., Crisco, J.J. (2022, February) Skin Motion Artifact of Radiopaque Bead Tracking Through Motion Relative to Markerless Bone Tracking [Oral presentation]. Biomedical Engineering Society Annual Meeting, San Antonio, TX.

Vaughan, Q.M., Ramella-Roman, J. (2020, November) Optical Phantoms for the Skin Through the Process of Decellularization [Virtual Poster presentation]. Annual Biomedical Research Conference for Minority Students, Miami, FL.

Vaughan, Q.M., Ramella-Roman, J. (2020, September) Optical Phantoms for the Skin Through the Process of Decellularization [Poster presentation]. Undergraduate Research Day, Miami, FL.

Awards

"Third Place Ortho Implant Poster," Awarded by Orthopaedic Research Society Ortho Implants Section for work titled "The Yucatan Minipig as a Potential Preclinical Animal Model for Carpal Bone Arthroplasty." (2024, February) Orthopaedic Research Society Annual Meeting, Long Beach, CA.

Teaching Experience

- Teaching Assistant, Stem Cell January-May 2023

Preface and Acknowledgments

The time has finally come to an end. The past five years have been filled with many ups and downs. At times I was discouraged and told this wasn't the path for me, but through the support, encouragement, and love of those around me, and a lot of stubbornness, I am proud of the work I have accomplished.

First, I would like to thank my advisor, Dr. Joseph Crisco, for giving me the opportunity five years ago to join the lab and work on this amazing project. I would also like to thank my committee members, Dr. Braden Fleming, Dr. Eric Darling, and Dr. Haneesh Kesari, all of whom were always available to answer questions, guide me through this journey, and challenge me on every aspect of this work to ensure I became an expert in this field.

Next, I would like to thank all of those who made this work truly possible. To Amy Morton, words cannot describe how much your mentorship and support have meant to me during this journey. You always took the time to teach me new software, listen to my ideas and methodologies, and be an amazing shoulder to lean on during difficult times. You also gave me the tough love I needed when I thought I couldn't continue and was ready to quit. Without you, I truly don't know where I would have ended up, and I am a better engineer because of the confidence you helped me find.

To Douglas Moore, thank you for being someone I could go to for anything and everything. Our conversations, especially when you played devil's advocate, pushed me to become a better researcher and taught me to approach problems from every perspective. You were by my side throughout this entire animal study, helping me navigate everything from managing a live study to publishing our work. Every weekday and weekend editing session was deeply appreciated.

To everyone who assisted with the live animal study, from animal ordering, surgery, to animal care, I am incredibly grateful. Without your help, I truly would not have been able to complete this project. To Anushka Jerez, Allison D'Amario, and Dr. Anne Merley, thank you for all the girl talks during animal surgeries. Sometimes a girl just needs to vent, and you were always there with a listening ear and a great support system outside of lab.

To Scott McAllister, what can I say Scotty, you're finally getting rid of me bossing you around. I hope you enjoyed our time together with the pigs as much as I did.

To my lab sisters, Dr. Josephine Kalshoven and Dr. Dominique Barnes, I don't even know where to begin. I was so lucky to have you both in my corner. You saw me through some of the hardest moments of my life, losing my grandmother in my

first year, walking out of meetings in tears feeling like I didn't belong, and questioning whether I should leave this path entirely. I can never thank you enough for your constant encouragement and for believing in me even when I didn't believe in myself.

I also cannot forget my favorite mentee, Landon Begin. When you first joined the lab, I made it a priority to ensure your experience was different from mine. Whether it was teaching you software, walking through methodologies, or helping with your animal study, I hope I helped you gain valuable experiences. And thank you for reminding me that I don't always have to be a "yes" person and that it's okay to stand up for myself when needed.

To my best friends, Emily Escobar and Jocelyn De La Rosa, you have been by my side since elementary school. You listened to me complain when things were hard and celebrated every accomplishment along the way. You gave me the breaks I needed to reset and have always been my biggest cheerleaders. Moving to Florida from New York gave me lifelong best friends, the sisters I never knew I needed, and I can't wait to see what the rest of life brings us.

To my cousins, aunts, and uncles, I am blessed to come from a large, loud, and loving Hispanic family. You have all been there for every accomplishment and have always been proud of me. I am grateful for the strong support system I can always turn to. To my younger cousins, Vicky, Suly, Aidan, and Deedee, I am especially grateful that graduate school brought me closer to you all. Our late-night conversations, froyo dates, and food runs made everything lighter.

To all the women in my family who helped shape who I am today: Tía Ani, from whom I inherited my freckles and Type A planning personality; Tía Kelly, who reminds me to have fun and not take everything so seriously; Tía Ana, for always making sure I had enough hair products, food, and tea; and Tía Norma and Abuelita Zoila, por invitarme siempre a comer, reír, bochinchar, y compartir comida ecuatoriana, siempre que lo necesitaba.

To my dad, Ernesto Vaughan, thank you, Popster, for always reminding me not to take life so seriously, even when I was stressed and called to vent about my project. Thank you for always making time to help me move and for our father-daughter food adventures in New York, even when it meant driving across boroughs.

To my mom, Katherine Santiago, what can I say, Momma, I finally did it. I can't fully express how grateful I am for the life you have given me. From sporting events, Girl Scouts, robotics competitions (which I know you never fully understood), school events, and award ceremonies, you were always there. It wasn't always easy, and we had our ups and downs, but you saw something in me

and pushed me to be my best, even when I resisted every step of the way. I am who I am today because of you.

And last, to my grandmother, Juana Santiago, ya han pasado cuatro años desde que falleciste, y te extraño tanto que cada día duele. Fuiste mi mejor amiga y mi mayor apoyo en la vida; extraño todos los recuerdos que creamos juntos en cada viaje de verano que hice a Puerto Rico. Todavía recuerdo cómo te echárselas de que su negrita era ingeniera y estaba estudiando para obtener su doctorado; bueno, ¡por fin lo logré, mamá! Y espero que, dondequiera que estés, siempre te esté haciendo sentir orgullosa. Te amaré por siempre, mamá.

Dedications

Le dedico esto a mi abuela Juana Esther Medina Santiago y a mi madre Katherine Elizabeth Santiago, las dos personas que me han convertido en la mujer que soy hoy.

Table of Contents

List of Tables

List of Illustrations

radius and ulna are fixed to the base using an L-shaped fixture and the metacarpals are secured to the end-effector of the robot. Force springs are attached to the flexor and extensor tendons. Fiducial collars used for digitization to register the specimen in the robotic coordinate system are included in the metacarpal and radius/ulna potting mixtures.

Figure 3.3. Average range of motion envelopes across the 28 motion directions for each condition: (A) intact, (B) all ligaments cut (ALC), (C) no radial carpal bone (RCB), and (D) small bone replacement with a radial carpal bone hemiarthroplasty (RCBH). Significant differences (p-values < 0.05) relative to intact are shown with a dot (•) and relative to ALC are shown with an asterisk (*).

Figure 3.4. Average stiffness envelopes across the 28 motion directions for each condition: (A) intact, (B) all ligaments cut (ALC), (C) no radial carpal bone (RCB), and (D) small bone replacement with a radial carpal bone hemiarthroplasty (RCBH). Significant differences (p-values < 0.05) relative to intact are shown with a dot (•) and relative to ALC are shown with an asterisk (*).

Figure 3.5. Pronation and supination at neutral and maximum range of motion (UF75) (average ± 95% confidence intervals) of the four testing conditions: intact, all ligaments cut (ALC), no radial carpal bone (RCB), and small bone replacement with a radial carpal bone hemiarthroplasty (RCBH). Significant differences (p-values < 0.05) are shown with an asterisk (*).

Figure 3.6. Average volar and dorsal translation ± 95% confidence intervals of the metacarpals relative to the radius and ulna for the four testing conditions:

intact, all ligaments cut (ALC), no radial carpal bone (RCB), and radial carpal bone hemiarthroplasty (RCBH). Significant differences (p-values < 0.05) are shown with an asterisk (*).

Figure 4.1. Bone models (dorsal view) of the YMP carpus depicting the ligament injury (LI) and small bone replacement (SBR) experimental groups. The YMP carpus consists of four metacarpals, two distinct rows of carpal bones, the radius and ulna. The ligament injury group (left) is a transection of the radial intermediate ligament (RIL) and dorsal intercarpal ligament (DIC), identified as homologous to the stabilizing ligaments of the human wrist. The small bone replacement group (right) shows the replacement of the radial carpal bone (RCB), homologous to the scaphoid, with a small bone implant (blue). The implant design includes a tendon port, drill guide, and suture through-holes.

Figure 4.2. Bone models of the YMP carpus and the sectioning planes used for histopathological analysis. The carpus was divided into a dorsal block (left) and a radial block (right) with dashed lines indicating the planes of section. Red boxes denote the articular surfaces scored for histology for each experimental group (Figure 4.4). For the ligament injury group, scored surfaces included the distal radius, proximal and distal RCB, and proximal CB2/CB3. For the small bone replacement group, scored surfaces included the distal radius and proximal CB2/CB3.

Figure 4.3. Mean gait ratios (surgical/contralateral) ± 95% confidence intervals over the 12-week study for the ligament injury (blue) and small bone replacement (red) groups for (A) max force, (B) impulse, (C) stance time, (D) stride velocity.

Significant differences within the small bone replacement group at each timepoint compared to preoperative are indicated by letters (*a* = p ≤ 0.0001; *b* = p ≤ 0.001; *c* = p ≤ 0.01; *d* = p ≤ 0.05). Significant differences between the ligament injury (LI) and small bone replacement (SBR) groups at each timepoint are indicated by asterisks (* = p ≤ 0.05; ** = p ≤ 0.01; *** = p ≤ 0.001; **** = p ≤ 0.0001).

Figure 4.4. Safranin-O/Fast Green staining of representative right carpal sections from the ligament injury (left) and small bone replacement (right) groups. The small bone replacement group demonstrated severe cartilage degeneration of the distal radius and proximal CB2/CB3, characterized by structural erosion, decreased chondrocyte density, and loss of Safranin-O staining. In contrast, the ligament injury group exhibited minimal structural disruption with mild reduction in Safranin-O staining.

Figure 4.5. Mean total OARSI scores ± 95% confidence intervals for the articular surfaces scored in the ligament injury and small bone replacement groups. Results are displayed for contralateral (black) and operated (grey) limbs. Significant differences are indicated by asterisks (* = p ≤ 0.05; ** = p ≤ 0.01).

Figure 5.1. 3D model of the right YMP carpus generated from micro-CT images, depicting the radius (RAD), ulna, two carpal rows, and metacarpals. Carpal bones are represented in their inertial coordinate system, while the radius, ulna, and metacarpals are represented in their anatomical coordinate systems. Standardized orientation of the coordinate systems is indicated by the axes: dorsal (positive X; red), proximal (positive Y; green), and ulnar (positive Z; blue).

Figure 5.2. The contralateral bone model is registered to the experimental bone model, and a Boolean subtraction is performed on the co-registered models to yield the osteophyte model.

Figure 5.3. Dorsal-radial view of the RCB, with eight cubes positioned at the origin of the RCB inertial coordinate system depicting the eight anatomical regions of the RCB osteophyte bone model separately analyzed for osteophyte development. The dorsal-distal-radial (DorDistRad) location of the RCB osteophyte model is displayed.

Figure 5.4. Articular surfaces (purple) analyzed for joint space (mm) for the ligament injury and small bone replacement groups. For the small bone replacement group, surfaces articulating with the RCB were excluded (RCB-RAD and RCB-CB2/CB3).

Figure 5.5. 3D models of the manually identified articular surfaces between the RCB (purple) and the radius (blue), used to compute joint space.

Figure 5.6. Osteophyte volume (average and SD) as a percentage of contralateral bone volume for the ligament injury group (n=4; blue), and the small bone replacement group (n=4; red). Osteophyte volume was significantly more extensive in the small bone replacement group after harvest at 12 weeks. For comparison, the volume of the bone differences of the control group (n=6; black) were significantly smaller in 3 bones compared to the ligament injury group and 6 bones compared to the small bone replacement group. Significant differences are denoted by an asterisk (* = $p<0.05$; ** = $p<0.01$; *** = $p<0.001$; **** = $p<0.0001$).

Supplementary Figure 5.1. Osteophyte models of the carpal bones for the ligament injury group (left column) and the small bone replacement group (right column), with colormaps depicting the distance (mm) from each osteophyte model to the surface of the corresponding contralateral bone model.

Supplementary Figure 5.2. Radial (left), dorsal (middle), and ulnar (right) views of a right YMP carpus following formalin fixation. Gapping is observed between the distal and proximal carpal rows, the proximal carpal row and the radius/ulna, suggesting the carpus was fixed in a minimally flexed orientation.

Chapter 1: Introduction

1.1. Motivation

Hand and upper extremity injuries and diseases contribute substantially to the burden of orthopedic conditions and can lead to painful osteoarthritis, functional disability, and reduced quality of life. Between 2018-2022, the most common wrist injuries reported in the National Electronic Injury Surveillance System (NEISS) database included lacerations, fractures, contusions, and sprains.[1] Among these, fractures, bony instability, and ligament injuries are at increased risk of developing post-traumatic osteoarthritis (OA).[2,3]

Despite the clinical and economic burden of wrist injuries, treatment outcomes remain worse than those for the hip, knee, or shoulder.[4] This disparity is partly attributed to the scarcity of studies and data on the wrist, which has impeded a thorough understanding of its anatomical, biomechanical, and functional complexity.[5,6] As a result, both conservative and surgical interventions for carpal osteoarthritis remain suboptimal. In the early stages of osteoarthritis, management is primarily conservative, including splinting, physical therapy, and nonsteroidal anti-inflammatory drugs.[7] While these approaches may alleviate symptoms, they do not halt disease progression. In advanced stages, surgical intervention is often required, with options such as partial or total wrist arthrodesis, proximal row carpectomy, and total wrist arthroplasty.[8–10] These procedures, however, have important limitations, including reduced upper extremity function after fusion and risks of component loosening or failure in arthroplasty.[11–17] Although they can provide acceptable long-term outcomes,[18–20] surgical interventions are inherently invasive and may further compromise

function, for example by restricting range of motion and reducing grip strength. Consequently, the absence of a validated preclinical animal model that accurately captures wrist biomechanics has limited the development of less invasive therapies. Addressing this gap is essential for facilitating the preclinical assessment of new osteoarthritis treatments.

1.2. Background

1.2.1. Use of Animal Models for Osteoarthritis Progression and Therapeutics

The use of animal models to study osteoarthritis dates back to 1963, initially employing inbred laboratory mice and rats.[21] Research has progressed from small animal models, including guinea pigs[22] and rabbits,[23–25] to larger species such as canines,[26–28] sheep,[29] goats,[30,31] pigs,[32–34] and horses.[35–40] Despite this trend, small animal models remain widely used because of their rapid disease progression, lower cost, and ease of housing.[21,24] These models are well suited for evaluating therapeutic effects on cartilage damage, but their small carpal bone anatomy limits their utility for investigating novel implants. In contrast, large animal models are often preferred due to their anatomical and biomechanical similarities to humans, particularly with respect to bone size and cartilage structure.[21,37,41,42]

Among available large animal models, the porcine is particularly advantageous, as it does not require specialized handling associated with zoonotic disease risks (e.g., Q fever) observed in livestock such as sheep and goats,[43] and is more feasible to house compared to larger species such as horses. Domestic pig breeds have limitations for preclinical studies due to rapid growth, large body size, and

potential aggressive or noisy behavior, which can complicate handling and housing.[44,45] These challenges are largely mitigated by miniature and micropig models, which avoid rapid growth phases, are easier to handle,[37] and reach skeletal maturity typically between 18 and 24 months.[46] The bone morphology, healing capacity, and macrostructural remodeling of pig bone closely resemble those of human bone,[42] although trabecular microstructure differs.[47] Collectively, these characteristics support the porcine model as a suitable and promising platform for studying human wrist pathologies.

Animal models have been extensively used to study osteoarthritis progression in large joints, particularly the knee, using chemical, mechanical, and surgical induction methods.[41,48] Surgical approaches typically target the stifle joint, homologous to the human knee, and include medial meniscal tear replication,[49] partial,[49] or total meniscectomy,[50,51] and anterior cruciate ligament transection.[23,51–54] Despite the widespread use of these models in large joints, comparatively few studies have investigated osteoarthritis progression or the development of treatment strategies in the wrist.

1.2.2. Anatomy of the Yucatan Minipig

The Yucatan minipig (YMP) carpus has been identified as a potential preclinical animal model for the human wrist due to similarities in size, anatomy, bone composition, and cartilage physiology.[33,55] Although the YMP is a weight-bearing animal, supporting approximately 60% of its weight on the forelimbs,[56] it represents a worst-case scenario for the human wrist.

The YMP forelimb consists of a radius, ulna, two carpal rows, and four metacarpals. The proximal carpal row includes the radial carpal bone (RCB), intermediate carpal bone (ICB), ulnar carpal bone (UCB), and accessory carpal bone (ACB), while the distal carpal row consists of 4 carpal bones (CB1-4) (**Figure 1.1**). The RCB has been identified as homologous to the human scaphoid based on imaging and perfusions studies demonstrating similar anatomy and blood supply.[55] The RCB consists of two articulating facets: a proximal facet that articulates with the radius and a distal facet that articulates with CB2 and CB3.

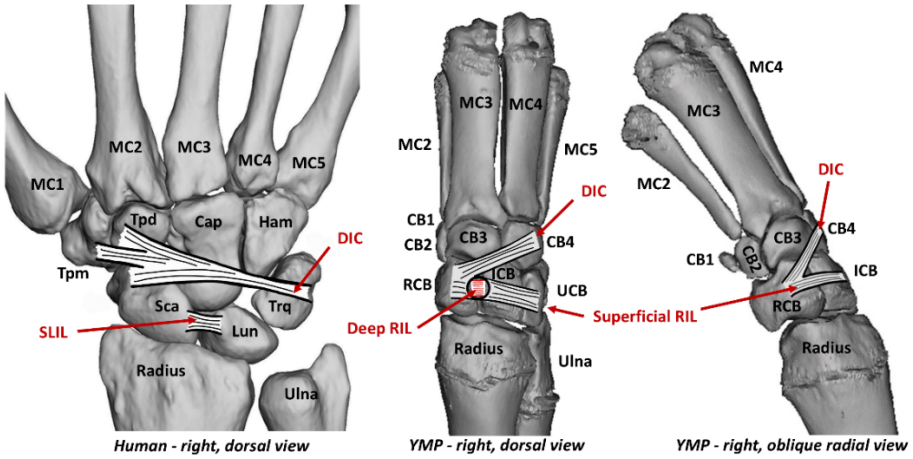

Human	YMP Minipig
Metacarpals (MC1-5)	Metacarpals (MC2-4)
Trapezium (Tpm)	1st carpal bone (CB1)
Trapezoid (Tpd)	2nd carpal bone (CB2)
Capitate (Cap)	3rd carpal bone (CB3)
Hamate (Ham)	4th carpal bone (CB4)
Scaphoid (Sca)	Radial carpal bone (RCB)
Lunate (Lun)	Intermediate carpal bone (ICB)
Triquetrum (Trq)	Ulnar carpal bone (UCB)
Pisiform (*not visible*)	Accessory carpal bone (*not visible*)

Figure 1.1. Computed tomography derived bone models of human and porcine (YMP) wrists illustrating proximal and distal carpal rows and ligament anatomy. The radial carpal bone (RCB) and intermediate carpal bone (ICB) are bound by deep and superficial aspects of the radial intermediate ligament (RIL); the superficial RIL spans the proximal carpal row, and the dorsal intercarpal ligament (DIC) extends distally from the RCB to the fourth carpal bone (CB4).

The ligamentous anatomy of the YMP carpus, particularly the structures associated with the RCB, is comparable to the primary and secondary stabilizers of the human wrist. The scapholunate interosseous ligament (SLIL), a primary stabilizer, contains dorsal and volar components that connect the scaphoid and

lunate.[6,57,58] The dorsal intercarpal ligament (DIC), a secondary stabilizer, spans the proximal carpal row and inserts distally on the scaphoid dorsal ridge, trapezium, and trapezoid.[6] In the YMP, the radial intermediate ligament (RIL) has been identified as homologous to the SLIL, with a deep insertion between the lateral RCB and medial ICB and a superficial component spanning the dorsal aspect of the proximal carpal row from the RCB to the UCB. The homologous YMP DIC extends obliquely from the dorsal RCB to CB4, connecting the proximal and distal carpal row (**Figure 1.1**).

1.3. Specific Aims

Our overall goal is to establish the YMP as a preclinical model for developing and validating innovative therapeutics, including carpal bone hemiarthroplasty, to treat ligament injuries and severe OA of the wrist. To achieve this, we aim to quantify YMP carpus biomechanics *in vitro* and evaluate OA progression *in vivo* following either ligament injury or implantation of a radial carpal bone hemiarthroplasty (RCBH). In Aim 1, we will design a YMP-specific RCBH using an established dataset of YMP wrist computed tomography (CT) scans and develop a surgical implant fixation technique in collaboration with a hand and wrist surgeon. In Aim 2 (*in vitro*), we will evaluate YMP carpus biomechanics under four conditions: intact, transection of all ligamentous attachments to the RCB, RCB resection, and RCBH implantation. In Aim 3 (*in vivo*), we will assess OA progression and severity following ligament injury induced by transection of the radial intermediate and dorsal intercarpal ligaments, as well as RCBH implantation. Together, these studies will define the functional and structural

characteristics of the YMP carpus and establish its potential as a preclinical animal model for the human wrist to support the development of novel therapeutics and implantable devices.

Specific Aim 1: Design a radial carpal bone hemiarthroplasty (RCBH) and evaluate a surgical approach for implantation.

Aim 1.1: Determine the shape and size variations of the RCB associated with bone volume, animal weight, and animal age from segmented CT scans of 35 YMP wrists.

Aim 1.2: Using a statistical shape model, determine the mean shape of the RCBs derived from the established YMP wrist dataset.

Design Criteria: The RCBH must have design features that assist with implant fixation, articulating surfaces that minimize cartilage degeneration, and the material must be biocompatible.

Specific Aim 2: Quantify YMP carpal biomechanics during intact, after transection of all ligamentous connections securing the RCB, after removal of the RCB, and after re-stabilization with a RCBH, *in vitro*.

Hypothesis 2.1: YMP wrist range of motion (ROM) will increase following transection of all ligaments connected to the RCB and further increase after RCB resection.

Hypothesis 2.2: YMP wrist ROM will restore to intact values following stabilization with a RCBH.

Specific Aim 3: Determine OA severity resulting from inducing carpal instability through ligament transection and re-stabilization with a RCBH in the YMP carpus 12-weeks postoperative, *in vivo*.

Aim 3.1: Quantify gait asymmetry and cartilage damage following ligament transection and small bone replacement with a RCBH.

Hypothesis 3.1: The ligament injury group will exhibit greater gait asymmetry and more severe histological cartilage degeneration than the small bone replacement group.

Aim 3.2: Characterize osteophyte formation and joint space changes following ligament transection and small bone replacement with a RCBH following the completion of a 12-week *in vivo* study.

Hypothesis 3.2: Animals in the ligament injury group will exhibit greater osteophyte formation and a narrower joint space in the operated limb than those in the small bone replacement group.

Completion of these aims will establish a foundation for the use of the YMP in preclinical studies of carpal bone hemiarthroplasty, supporting the development of therapies for carpal instability and OA while informing the design of next-generation wrist implants.

1.4. References

1. Aceto M, Shaylor J, Zumsteg J. Most Common Consumer Products Associated With Hand and Wrist Injuries Presenting to US Emergency Departments: An NEISS Database Analysis. *Hand*. Published online November 27, 2025:15589447251392939. doi:10.1177/15589447251392939
2. Kitay A, Wolfe SW. Scapholunate instability: current concepts in diagnosis and management. *J Hand Surg*. 2012;37(10):2175-2196. doi:10.1016/j.jhsa.2012.07.035
3. Peterson B, Szabo RM. Carpal osteoarthrosis. *Hand Clin*. 2006;22(4):517-528; abstract vii. doi:10.1016/j.hcl.2006.07.001
4. de Putter CE, Selles RW, Polinder S, Panneman MJM, Hovius SER, van Beeck EF. Economic impact of hand and wrist injuries: health-care costs and productivity costs in a population-based study. *J Bone Joint Surg Am*. 2012;94(9):e56. doi:10.2106/JBJS.K.00561
5. Rainbow MJ, Wolff AL, Crisco JJ, Wolfe SW. Functional kinematics of the wrist. *J Hand Surg Eur Vol*. 2016;41(1):7-21. doi:10.1177/1753193415616939
6. Wolfe SW, Kakar S. Chapter 13: Carpal Instability. In: Wolfe SW, Pederson WC, Kozin SH, Cohen MS, eds. *Green's Operative Hand Surgery*. Eighth Edition. Elsevier Health Sciences; 2022:488-497.
7. De Smet L, Degreef I, Robijns F, Truyen J, Deprez P. Salvage procedures for degenerative osteoarthritis of the wrist due to advanced carpal collapse. *Acta Orthop Belg*. 2006;72(5):535-540.
8. Adams BD, Kleinhenz BP, Guan JJ. Wrist Arthrodesis for Failed Total Wrist Arthroplasty. *J Hand Surg*. 2016;41(6):673-679. doi:10.1016/j.jhsa.2016.02.012
9. Kay HF, Kang HP, Alluri R, Azad A, Ghiassi A. Proximal Row Carpectomy Versus 4-Corner Fusion: Incidence, Conversion to Fusion, and Cost. *J Hand Surg*. Published online February 20, 2020. doi:10.1016/j.jhsa.2019.12.010
10. Wagner ER, Srnec JJ, Fort MW, Barras LA, Rizzo M. Outcomes of Revision Total Wrist Arthroplasty. *J Am Acad Orthop Surg Glob Res Rev*. 2021;5(3). doi:10.5435/JAAOSGlobal-D-21-00035
11. Krukhaug Y, Lie SA, Havelin LI, Furnes O, Hove LM. Results of 189 wrist replacements. A report from the Norwegian Arthroplasty Register. *Acta Orthop*. 2011;82(4):405-409. doi:10.3109/17453674.2011.588858
12. Harlingen D van, Heesterbeek PJC, J de Vos M. High rate of complications and radiographic loosening of the biaxial total wrist arthroplasty in rheumatoid arthritis: 32 wrists followed for 6 (5–8) years. *Acta Orthop*. 2011;82(6):721-726. doi:10.3109/17453674.2011.636669
13. Takwale VJ, Nuttall D, Trail IA, Stanley JK. Biaxial total wrist replacement in patients with rheumatoid arthritis. Clinical review, survivorship and radiological analysis. *J Bone Joint Surg Br*. 2002;84(5):692-699.

14. Cavaliere CM, Chung KC. A systematic review of total wrist arthroplasty compared with total wrist arthrodesis for rheumatoid arthritis. *Plast Reconstr Surg*. 2008;122(3):813-825. doi:10.1097/PRS.0b013e318180ece3
15. Nair R. Review article: Total wrist arthroplasty. *J Orthop Surg Hong Kong*. 2014;22(3):399-405.
16. Ward CM, Kuhl T, Adams BD. Five to ten-year outcomes of the Universal total wrist arthroplasty in patients with rheumatoid arthritis. *J Bone Joint Surg Am*. 2011;93(10):914-919. doi:10.2106/JBJS.H.01614
17. Lorei MP, Figgie MP, Ranawat CS, Inglis AE. Failed total wrist arthroplasty. Analysis of failures and results of operative management. *Clin Orthop*. 1997;(342):84-93.
18. Chim H, Moran SL. Long-Term Outcomes of Proximal Row Carpectomy: A Systematic Review of the Literature. *J Wrist Surg*. 2012;1(2):141-148. doi:10.1055/s-0032-1329547
19. Eschweiler J, Li J, Quack V, et al. Total Wrist Arthroplasty-A Systematic Review of the Outcome, and an Introduction of FreeMove-An Approach to Improve TWA. *Life Basel Switz*. 2022;12(3):411. doi:10.3390/life12030411
20. Andronic O, Nagy L, Burkhard MD, et al. Long-term outcomes of the four-corner fusion of the wrist: A systematic review. *World J Orthop*. 2022;13(1):112-121. doi:10.5312/wjo.v13.i1.112
21. McCoy AM. Animal Models of Osteoarthritis: Comparisons and Key Considerations. *Vet Pathol*. 2015;52(5):803-818. doi:10.1177/0300985815588611
22. Jimenez PA, Glasson SS, Trubetskoy OV, Haimes HB. Spontaneous osteoarthritis in Dunkin Hartley guinea pigs: histologic, radiologic, and biochemical changes. *Lab Anim Sci*. 1997;47(6):598-601.
23. Batiste DL, Kirkley A, Laverty S, Thain LMF, Spouge AR, Holdsworth DW. Ex vivo characterization of articular cartilage and bone lesions in a rabbit ACL transection model of osteoarthritis using MRI and micro-CT. *Osteoarthritis Cartilage*. 2004;12(12):986-996. doi:10.1016/j.joca.2004.08.010
24. Serra CI, Soler C. Animal Models of Osteoarthritis in Small Mammals. *Veterinary Clin North Am Exot Anim Pract*. 2019;22(2):211-221. doi:10.1016/j.cvex.2019.01.004
25. Yoshioka M, Coutts RD, Amiel D, Hacker SA. Characterization of a model of osteoarthritis in the rabbit knee. *Osteoarthritis Cartilage*. 1996;4(2):87-98. doi:10.1016/s1063-4584(05)80318-8
26. Brandt KD. Transection of the anterior cruciate ligament in the dog: a model of osteoarthritis. *Semin Arthritis Rheum*. 1991;21:22-32.
27. Little D, Johnson S, Hash J, et al. Functional outcome measures in a surgical model of hip osteoarthritis in dogs. *J Exp Orthop*. 2016;3(1):17. doi:10.1186/s40634-016-0053-5
28. Pond MJ, Nuki G. Experimentally-induced osteoarthritis in the dog. *Ann Rheum Dis*. 1973;32(4):387-388. doi:10.1136/ard.32.4.387
29. Cake MA, Read RA, Corfield G, et al. Comparison of gait and pathology outcomes of three meniscal procedures for induction of knee osteoarthritis

in sheep. *Osteoarthritis Cartilage*. 2013;21(1):226-236. doi:10.1016/j.joca.2012.10.001
30. Olson EJ, Wentorf FA, McNulty MA, Parker JB, Carlson CS, LaPrade RF. Assessment of a goat model of posterolateral knee instability. *J Orthop Res Off Publ Orthop Res Soc*. 2008;26(5):651-659. doi:10.1002/jor.20529
31. Ko JY, Lee J, Lee J, Im GI. Intra-articular Xenotransplantation of Adipose-Derived Stromal Cells to Treat Osteoarthritis in a Goat Model. *Tissue Eng Regen Med*. 2017;14(1):65-71. doi:10.1007/s13770-016-0010-5
32. Pinette MP, Molino J, Proffen BL, Murray MM, Fleming BC. Effects of Male and Female Sex on the Development of Posttraumatic Osteoarthritis in the Porcine Knee After Anterior Cruciate Ligament Surgery. *Am J Sports Med*. 2022;50(9):2417-2423. doi:10.1177/03635465221102118
33. Stoeckl BD, Zlotnick HM, Farrell MJ, et al. The porcine accessory carpal bone as a model for biologic joint replacement for trapeziometacarpal osteoarthritis. *Acta Biomater*. 2021;129:159-168. doi:10.1016/j.actbio.2021.05.011
34. Zhao R, Dong Z, Wei X, et al. Inflammatory factors are crucial for the pathogenesis of post-traumatic osteoarthritis confirmed by a novel porcine model: “Idealized” anterior cruciate ligament reconstruction" and gait analysis. *Int Immunopharmacol*. 2021;99:107905. doi:10.1016/j.intimp.2021.107905
35. McIlwraith CW, Frisbie DD, Kawcak CE. The horse as a model of naturally occurring osteoarthritis. *Bone Jt Res*. 2012;1(11):297-309. doi:10.1302/2046-3758.111.2000132
36. Cook JL, Hung CT, Kuroki K, et al. Animal models of cartilage repair. *Bone Jt Res*. 2014;3(4):89-94. doi:10.1302/2046-3758.34.2000238
37. Teeple E, Jay GD, Elsaid KA, Fleming BC. Animal models of osteoarthritis: challenges of model selection and analysis. *AAPS J*. 2013;15(2):438-446. doi:10.1208/s12248-013-9454-x
38. Lampropoulou-Adamidou K, Lelovas P, Karadimas EV, et al. Useful animal models for the research of osteoarthritis. *Eur J Orthop Surg Traumatol Orthop Traumatol*. 2014;24(3):263-271. doi:10.1007/s00590-013-1205-2
39. Bendele AM. Animal models of osteoarthritis. *J Musculoskelet Neuronal Interact*. 2001;1(4):363-376.
40. Oláh T, Cucchiarini M, Madry H. Subchondral bone remodeling patterns in larger animal models of meniscal injuries inducing knee osteoarthritis - a systematic review. *Knee Surg Sports Traumatol Arthrosc Off J ESSKA*. 2023;31(12):5346-5364. doi:10.1007/s00167-023-07579-6
41. Longo UG, Papalia R, De Salvatore S, Picozzi R, Sarubbi A, Denaro V. Induced Models of Osteoarthritis in Animal Models: A Systematic Review. *Biology*. 2023;12(2):283. doi:10.3390/biology12020283
42. Pearce AI, Richards RG, Milz S, Schneider E, Pearce SG. Animal models for implant biomaterial research in bone: a review. *Eur Cell Mater*. 2007;13:1-10. doi:10.22203/ecm.v013a01
43. Patil SM, Regunath H. Q Fever. In: *StatPearls*. StatPearls Publishing; 2026. Accessed March 24, 2026. http://www.ncbi.nlm.nih.gov/books/NBK556095/

44. Newman E, Turner AS, Wark JD. The potential of sheep for the study of osteopenia: current status and comparison with other animal models. *Bone*. 1995;16(4 Suppl):277S-284S. doi:10.1016/8756-3282(95)00026-a
45. Swindle MM, Smith AC, Hepburn BJ. Swine as models in experimental surgery. *J Investig Surg Off J Acad Surg Res*. 1988;1(1):65-79. doi:10.3109/08941938809141077
46. Murray MM, Magarian EM, Harrison SL, Mastrangelo AN, Zurakowski D, Fleming BC. The effect of skeletal maturity on functional healing of the anterior cruciate ligament. *J Bone Joint Surg Am*. 2010;92(11):2039-2049. doi:10.2106/JBJS.I.01368
47. Mosekilde L, Weisbrode SE, Safron JA, et al. Calcium-restricted ovariectomized Sinclair S-1 minipigs: an animal model of osteopenia and trabecular plate perforation. *Bone*. 1993;14(3):379-382. doi:10.1016/8756-3282(93)90167-9
48. Lampropoulou-Adamidou K, Lelovas P, Karadimas EV, et al. Useful animal models for the research of osteoarthritis. *Eur J Orthop Surg Traumatol Orthop Traumatol*. 2014;24(3):263-271. doi:10.1007/s00590-013-1205-2
49. Bendele AM. Animal models of osteoarthritis. *J Musculoskelet Neuronal Interact*. 2001;1(4):363-376.
50. Matsui Y, Iwasaki N, Kon S, et al. Accelerated development of aging-associated and instability-induced osteoarthritis in osteopontin-deficient mice. *Arthritis Rheum*. 2009;60(8):2362-2371. doi:10.1002/art.24705
51. Hayami T, Pickarski M, Zhuo Y, Wesolowski GA, Rodan GA, Duong LT. Characterization of articular cartilage and subchondral bone changes in the rat anterior cruciate ligament transection and meniscectomized models of osteoarthritis. *Bone*. 2006;38(2):234-243. doi:10.1016/j.bone.2005.08.007
52. Proffen BL, McElfresh M, Fleming BC, Murray MM. A comparative anatomical study of the human knee and six animal species. *The Knee*. 2012;19(4):493-499. doi:10.1016/j.knee.2011.07.005
53. Kamekura S, Hoshi K, Shimoaka T, et al. Osteoarthritis development in novel experimental mouse models induced by knee joint instability. *Osteoarthritis Cartilage*. 2005;13(7):632-641. doi:10.1016/j.joca.2005.03.004
54. Karamchedu NP, Murray MM, Sieker JT, et al. Bridge-Enhanced Anterior Cruciate Ligament Repair Leads to Greater Limb Asymmetry and Less Cartilage Damage Than Untreated ACL Transection or ACL Reconstruction in the Porcine Model. *Am J Sports Med*. 2021;49(3):667-674. doi:10.1177/0363546521989265
55. Behrends DA, Khendek L, Gao C, Zayed N, Henderson JE, Martineau PA. Characterization of a Pre-Clinical Mini-Pig Model of Scaphoid Non-Union. *J Funct Biomater*. 2015;6(2):407-421. doi:10.3390/jfb6020407
56. Kaiser EE, Waters ES, Fagan MM, et al. Characterization of tissue and functional deficits in a clinically translational pig model of acute ischemic stroke. *Brain Res*. 2020;1736:146778. doi:10.1016/j.brainres.2020.146778
57. Waters MS, Werner FW, Haddad SF, McGrattan ML, Short WH. Biomechanical Evaluation of Scaphoid and Lunate Kinematics Following

Selective Sectioning of Portions of the Scapholunate Interosseous Ligament. *J Hand Surg*. 2016;41(2):208-213. doi:10.1016/j.jhsa.2015.11.009

58. Rajan PV, Day CS. Scapholunate Interosseous Ligament Anatomy and Biomechanics. *J Hand Surg*. 2015;40(8):1692-1702. doi:10.1016/j.jhsa.2015.03.032

Chapter 2: Development of Small Bone Implants Using a Mean Shape Bone in a Porcine Model for Carpal Bone

Vaughan QM, Morton AM, Moore D, Akelman E, Crisco JJ. Development of small bone implants using a mean shape bone in a porcine model for carpal bone replacement. *Proc Inst Mech Eng H*. 2025;239(8):755-765. doi:10.1177/09544119251355382

2.1. Abstract

The development of innovative small bone replacements for the human wrist has been partially limited by the lack of a suitable preclinical animal model. This study explores the feasibility of using the Yucatan minipig (YMP) as a preclinical model for small bone replacement. Implants for the radial carpal bone (RCB), homologous to the human scaphoid, were developed for a pilot *in vivo* animal study. RCB size (volume, bounding box dimensions) was quantified (n=35), and relationships between animal age, weight, and RCB volume were investigated. Bounding box dimensions were also analyzed relative to RCB volume. A mean-shaped RCB model was generated using ShapeWorks Studio and scaled to create a set of implants. These implants were evaluated in the pilot *in vivo* study, where the distances between the explanted bone surface and both the predicted and surgeon-selected implant surfaces were recorded for each animal. Predicted implant distances (0.8 ± 0.2 mm), were larger ($p < 0.001$) than surgeon-selected implant distances (0.4 ± 0.1 mm) in three animals. In one animal, the predicted implant distances (0.3 ± 0.2 mm) were smaller ($p < 0.0001$) than the surgeon-selected implant distances (0.5 ± 0.3 mm). The set of implants generated provided the surgeon with options suitable for the range of animals in the *in vivo* study. This study presents a novel approach to generating small bone replacements by scaling a mean-shaped bone in a porcine model and further evaluates the YMP as a preclinical model for small bone replacement in the human wrist.

2.2. Introduction

Injuries and degenerative disease of the wrist present unique challenges in orthopedic treatment due to the anatomical complexity of the wrist.[1,2] These injuries can significantly impact a patient's quality of life by causing pain, disability, reduced range of motion, and potentially leading to osteoarthritis. If conservative treatments are ineffective, surgical options can help preserve wrist function while counteracting degenerative changes. Surgical treatment options include wrist fusion (arthrodesis),[3,4] proximal row carpectomy,[5–7] and total wrist replacement (arthroplasty),[8–11] but each has limitations, such as hardware failure,[4] decreased grip strength[6,7] and component loosening.[9–12] For active patients with viable articular cartilage on one joint surface, wrist hemiarthroplasties, which include individual replacement of carpal bones, offer motion-preserving alternatives to total wrist fusion or arthroplasty.[13,14]

Currently, "off-the-shelf" small bone replacements for wrist hemiarthroplasty are available in a range of sizes that fit a general population. These implants aim to restore function, relieve pain, and maintain the relationship of surrounding carpal bones.[15–17] The implants are composed of materials such as silicone,[15,18–21] polyurethane urea,[22] pyrolytic carbon,[15,21,23–26] or metal.[15,21,27] However, implants have been found to degrade over time, generating debris and leading to complications, such as silicone synovitis, cystic lesions in adjacent bones,[18,19,28] bone erosion,[29] and an increased risk of dislocation.[15,23,30] The design of a successful small bone replacement is further complicated by the intricate geometry of native carpal bones. [31]

Advancements in three-dimensional (3D) printing have revolutionized the development of patient-specific orthopedic implants by enabling replication of native bone geometry. These implants, typically derived from computed tomography (CT) scans,[32–39] provide a match to the anatomy of the patient and facilitate osteointegration when desired.[40–43] Various materials, including titanium,[33–35,38,44] tantalum,[32] polyetheretherketone (PEEK),[37] and polyethylene,[39] have been used in 3D-printed patient-specific scaphoid and lunate implant manufacturing. Studies have reported improved wrist biomechanics compared to preoperative results in patients treated with patient specific implants particularly in wrist range of motion, pinch and grasp strength.[32,34,35,38] However, the development of these implants requires extensive preoperative planning, complex modeling software, and longer lead time in manufacturing.[40,41,45]

The development of innovative small bone arthroplasty treatments has also been partially limited by the lack of a suitable preclinical animal model for the human wrist. The domestic pig has emerged as a promising model due to similarities in size, anatomy, and bone composition.[46] Studies have utilized domestic pig forelimbs for evaluating fixation methods in trapeziometacarpal arthroplasty,[47–49] trapeziometacarpal joint arthrodesis,[50] and for testing metacarpal and phalangeal fracture fixation locking plates.[51–55] Notably, the domestic pig is a weight-bearing animal that places approximately 60% of its weight on the forelimbs,[56] resulting in higher loads sustained by the domestic pig carpus. These characteristics make the domestic pig a desirable model for simulating “worst-case scenarios” for the human wrist. Specifically, the Yucatan minipig (YMP) carpus has been evaluated as a potential preclinical animal model

for the human carpus. For example, Altieri et al. quantified the biomechanics of the YMP carpus after radial intermediate ligament (RIL) and dorsal intercarpal ligament (DIC) transection, to model scapholunate interosseous ligament (SLIL) and DIC injury in the human wrist.[57] Previously, Stoeckl et al. used the accessory carpal bone of the YMP carpus in a biologic joint replacement study for trapeziometacarpal osteoarthritis,[58] and Behrends et al. used the YMP to model scaphoid nonunion.[59] However, the suitability of the YMP carpus as a model for small bone replacement remains unexplored.

Further evaluation of the YMP carpus as a preclinical animal model for the human wrist, particularly for small bone replacement, may advance the development and testing of innovative wrist hemiarthroplasties that mitigate complications associated with design, cost, and degradation. To investigate this potential, we explored the radial carpal bone (RCB) in the YMP as a model for the human scaphoid.[59] Our goal in this study was to develop an approach for generating a set of implants for RCB replacement for an *in vivo* study. First, the size of the RCB was quantified using metrics of volume and bounding box dimensions. We then evaluated the relationships between animal age, weight, and bone volume, as well as between bounding box dimensions and bone volume. Based on these relationships, we developed a model to generate a set of RCB implants and assessed how well they fit, as compared to surgeon-selected implants, in an *in vivo* pilot YMP study.

2.3. Methods

2.3.1. YMP Forelimb Sourcing to Generate an RCB Dataset

Twenty-three YMP forelimbs (11 pairs, 1 unpaired) were harvested from animals used in an unrelated meniscal tissue study. In this cohort, there were 9 females and 3 males ranging in age from 13.0 to 20.1 months (mean: 18.5 ± 1.8 months) and weight from 49.3 to 61.0 kilograms (kg) (mean: 54.0 ± 4.1 kg) (Premier BioSource, Ramona, CA). An additional 12 YMP forelimbs (6 pairs) were acquired from naive animals through purchase (Sinclair Bio-Resources, Windham, ME). These animals included 3 females and 3 males ranging in age from 32.1 to 41.3 months (mean: 38.1 ± 3.3 months) and weight from 66.0 to 99.9 kg (mean: 79.6 ± 14.9 kg). All the animals were acquired following IACUC review and approval. The CT imaged RCB models from these 35 YMP forelimbs (RCB dataset) were analyzed to 1) calculate bone volume as a function of animal age and weight, and 2) to inform the design of a size-varied set of RCB implants (**Figure 2.1**).

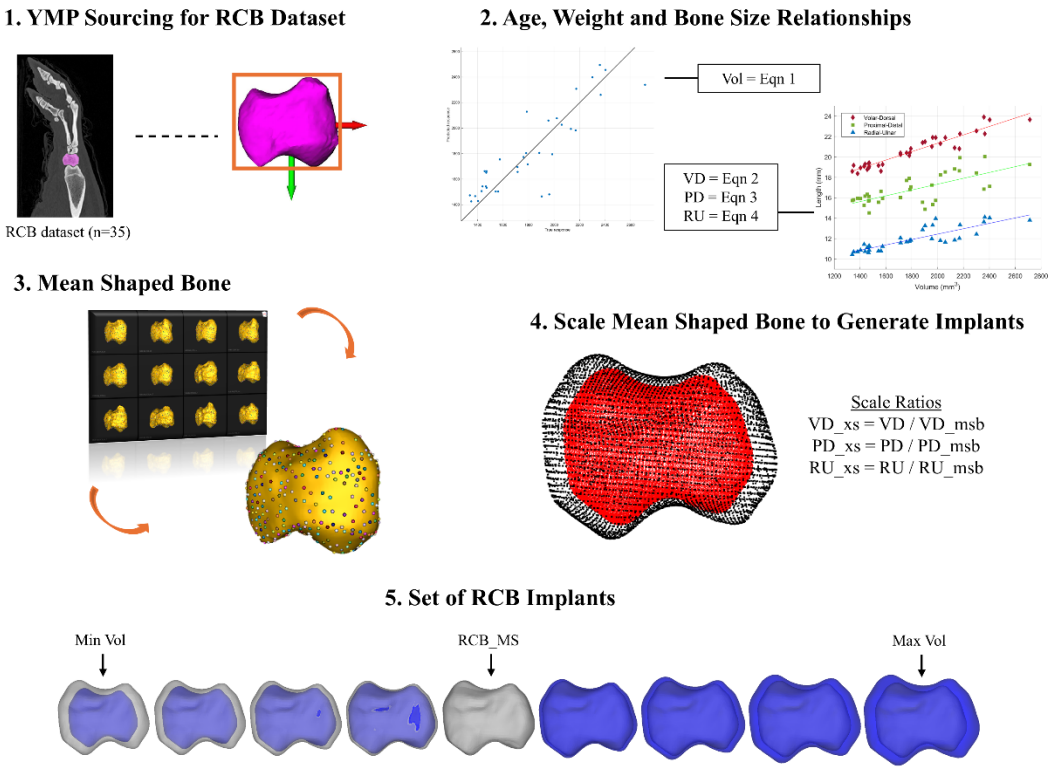

Figure 2.1. Flow chart of the steps to generate a set of implants. 1) Bone volume and bounding box dimensions (volar-dorsal (VD), proximal-distal (PD), radial-ulnar (RU)) were calculated from segmented RCB models (RCB dataset). 2) Bone size relationships were analyzed to model RCB volume as a function of animal age and weight, and bounding box dimensions as a function of volume. 3) A mean shaped bone (RCB_MS) was generated from the RCB dataset and the bounding box dimensions were recorded (VD_msb, PD_msb, RU_msb). 4) The RCB_MS was scaled by the ratio of the estimated dimensions [Eqn 2-4] to the corresponding RCB_MS dimension to generate a set of RCB implants. An example of the scaled implant model (black) and the RCB_MS model (red) is shown. 5) A set of 9 RCB implants was generated with linearly spaced increments from the RCB_MS to encompass small and large animals.

2.3.2. CT Imaging and Bone Size Analysis

All forelimbs were imaged using a clinical CT scanner (GE Healthcare, Chicago, IL) with an image resolution of 0.4 mm x 0.4 mm in-plane and 0.625 mm slice thickness.[60] The radial carpal bone (RCB) in each image was segmented in MIMICS v22 (Materialise, Leuven, Belgium) using a density-based threshold and

manual editing to ensure the mask accurately captured the bone's outer cortical surface. Three-dimensional (3D) models of the RCB cortical bone surfaces were exported as closed triangular meshes with no triangle reduction and minimal smoothing (iterations: 1; smooth factor: 0.030). All left forelimb RCB models were mathematically mirrored to the right for consistent orientation. Coordinate systems for each RCB were constructed by calculating the bones' geometric centroids as the origins and the principal inertial axes as the coordinate axes,[61,62] which generally aligned with the anatomical axes of the YMP forelimb. The directions of the RCB coordinate system axes were defined positive X in the dorsal direction, positive Y in the proximal direction, and positive Z in the ulnar direction, toward the intermediate carpal bone (ICB) (**Figure 2.2**). Bone volume and bounding box dimensions, defined as the lengths between the minimum and maximum extents along each coordinate system axes, were calculated for each RCB using custom-written code. The bone volumes and bounding box dimensions of the RCB were averaged between the paired forelimbs (17 paired) and 1 unpaired.

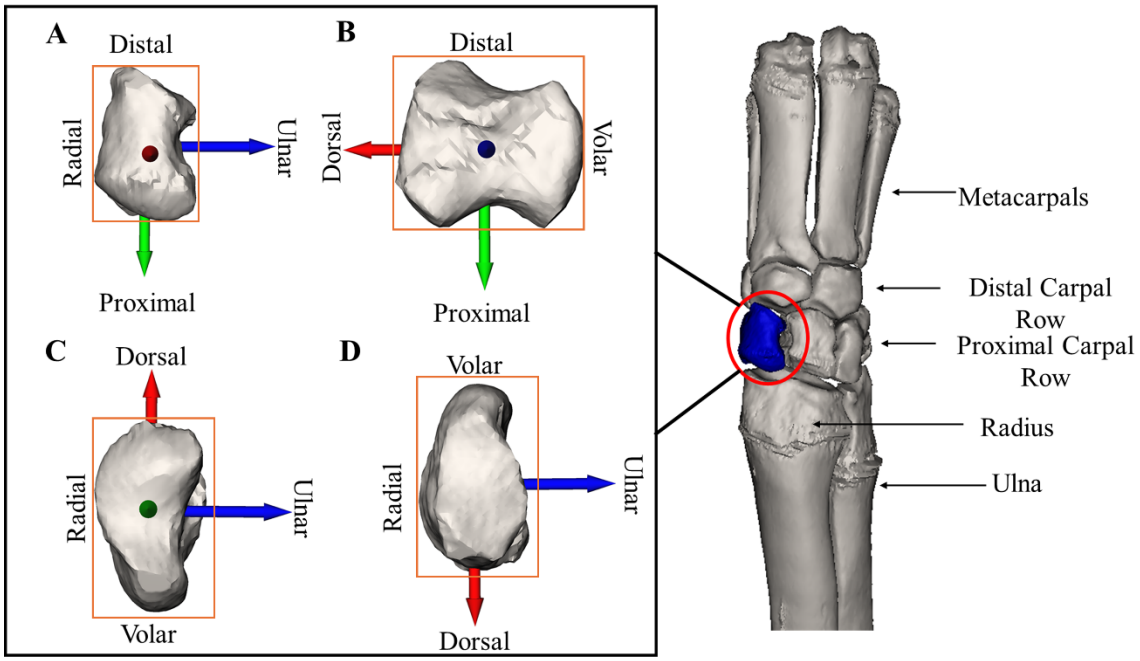

Figure 2.2. Right YMP 3D carpus model with the RCB inertial coordinate system from four different views: (A) dorsal, (B) ulnar, (C) proximal, and (D) distal. Standardized orientation is depicted with axes: dorsal (positive X; red), proximal (positive Y; green), and ulnar (positive Z; blue). Bounding box outline in orange.

2.3.3. Age, Weight and Bone Size Relationships

Multiple linear regression was performed to express RCB volume (dependent variable) as a function of animal age (months) and weight (kg) [Eqn 1].

$$Vol = -1455 + Age*67.18 + Weight*51.85 + Age*Weight*-0.9950 \quad [Eqn\ 1]$$

The respective volar-dorsal (VD), proximal-distal (PD), and radial-ulnar (RU) bounding box dimension values computed from the RCB dataset were linearly regressed independently against RCB volume [Eqn 2-4] and R^2 values were calculated (**Figure 2.3**).

$$VD = 0.004158*Vol + 13.03 \quad \text{[Eqn 2]}$$

$$PD = 0.002850*Vol + 11.65 \quad \text{[Eqn 3]}$$

$$RU = 0.002606*Vol + 7.23 \quad \text{[Eqn 4]}$$

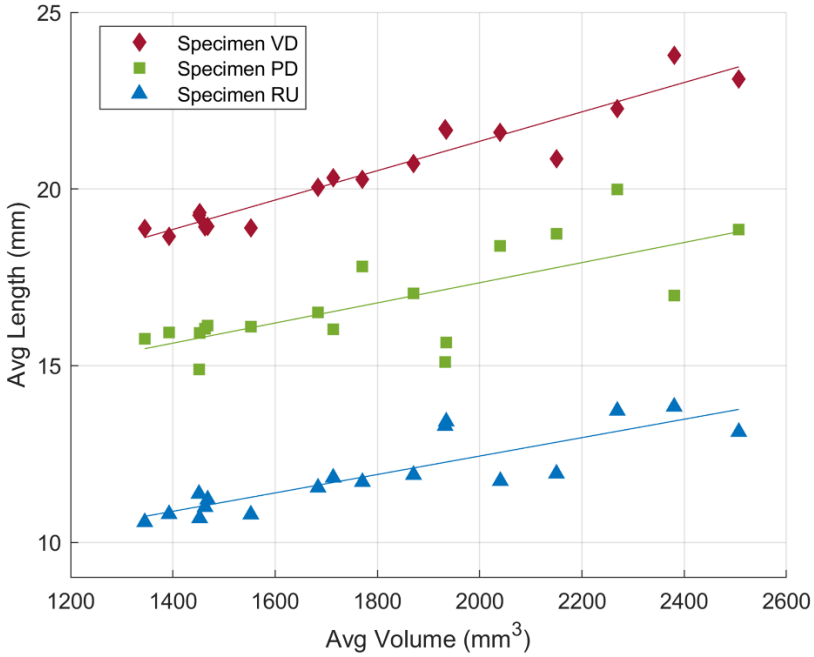

Figure 2.3. Linear regression analyses of the relationship between RCB volume and each bounding box dimension across the RCB dataset (n=18).

2.3.4. Mean Shaped Bone and Implant Development

A set of RCB implants was created by scaling a mean shaped bone generated from the RCB dataset. The mean shaped bone (RCB-MS) was generated using ShapeWorks Studio v6.2.1 (University of Utah, Salt Lake City, UT).[63] The segmented RCB models were expressed in their inertial coordinate system for initial co-registration alignment. In ShapeWorks, each RCB surface was represented as a set of particles, with correspondence across models. Particle counts and weights were iterated and resultant model remeshing distortion was

assessed. 512 particles with an initial relative weight of 1 resulted in minimal model distortion and a mean shape of the RCB, which was exported in STL format. Volume and bounding box dimensions of the RCB-MS were computed.

Our goal was to generate a set of various sized implants that at least encompassed the range of bone volumes and bounding box dimensions in the RCB dataset. First, we established discrete target volume values for the implant set. To start, we assumed that the largest animal in the *in vivo* study would be at least 24 months old (skeletally mature) and weigh 110 kg, ~10% greater than the heaviest animal in our YMP dataset. Using equation 1, the estimated RCB volume for a 24 months, 110 kg animal established an upper bound of implant target volumes. The difference between the estimated largest RCB volume and the RCB-MS volume was then divided by four to determine the volume increment for a set of 5 implants (**Table 2.1**). An additional four volumes smaller than the RCB-MS were calculated using the same volume increment to ensure the set of implants covered smaller animals.

Table 2.1. Target volumes for desired implant sizes with the bounding box dimensions (volar-dorsal, proximal-distal, radial-ulnar) and volumes of the implant models generated by scaling the RCB-MS.

	Predicted Volume (mm^3)	Volar-Dorsal Length (mm)	Proximal-Distal Length (mm)	Radial-Ulnar Length (mm)	Calculated Volume (mm^3)
Implant 1	843	16.6	14.0	9.4	986.9
Implant 2	1174.3	17.9	15.0	10.3	1247.1
Implant 3	1506.5	19.3	15.9	11.1	1549.0
Implant 4	1838.8	20.7	16.9	12.0	1895.7
Implant 5	2171	22.0	17.8	12.9	2290.4
Implant 6	2503.3	23.4	18.8	13.8	2736.1
Implant 7	2835.5	24.8	19.7	14.6	3235.8
Implant 8	3167.8	26.1	20.7	15.5	3792.8
Implant 9	3500	27.5	21.6	16.4	4410.0

The resulting set of 9 RCB implant models were generated via anisotropic scaling of the RCB-MS model. To do so, the RCB-MS model was scaled independently in the volar-dorsal, proximal-distal, and radial-ulnar directions using scale factors determined from equations 2 through 4. Volumes and bounding box dimensions of the resultant implant models were calculated.

2.3.5. Evaluation of Implant Sizing

Our implant size prediction method was evaluated by comparing both model-predicted implants and surgeon-selected implants to micro-CT segmented RCBs from animals in a pilot *in vivo* study. The *in vivo* study evaluated the RCB as a potential model for small bone hemiarthroplasty. Eight animals were randomly assigned to two groups, one in which the radial intercarpal ligament (RIL) and the dorsal intercarpal ligament (DIC) connected to the RCB were transected (n=4;

ligament transection group), the other in which the RCB was replaced with an implant (n=4; implant group). The implants were manufactured out of Cobalt-Chrome (CoCr) via direct metal laser sintering (3D printing), hand polished of the articulating surfaces to a mirror-like finish (~0.5 μm), cleaned, and sterile packaged prior to surgery use. The primary outcomes of that study, which include spatiotemporal gait analysis and histology assessment of cartilage health, will be reported elsewhere. In this paper, we report how the implants compared to the RCBs of the *in vivo* animals. The animals included 4 females and 4 males ranging in age from 24.4 to 29.8 months (mean: 25.7 ± 1.8 months) and weight from 56.9 to 101.2 kg (mean: 84.2 ± 13.6 kg). All surgeries were performed on the right forelimb by a board-certified hand surgeon. All live animal work was reviewed and approved by the IACUC.

For the four animals in the implant group, a "Predicted RCB Implant" was determined before surgery using the animal's age and weight as inputs in equation 1. The predicted volume estimated from equation 1 was compared to the volumes of our list of implants and the implant whose volume was closest to the predicted volume was selected as the Predicted RCB Implant. The final "Surgeon-Selected Implant" used in each animal was determined by the surgeon at the time of surgery, based on his subjective assessment of fit and joint manipulation.

At the end of the 12-week study, the left and right carpus were harvested from each animal by sectioning the distal end of the radius/ulna and the proximal end of the metacarpals. The implant was removed from the right carpus and 3D images of the left and right carpus were generated using a SKYSCAN 1276 scanner (Bruker,

Billerica, MA) with an image resolution of 0.1205 mm voxel size. The RCBs were segmented from the images of each left carpus using MIMICS v22, yielding 3D models of the RCB cortical bone surfaces. The left RCB models were mirrored to the right for consistent orientation and the inertial based coordinate system for each RCB was constructed. Volume and bounding box dimensions for each RCB were calculated for the *in vivo* animals.

Implant sizing was evaluated by comparing digital models of the mirrored left RCB (Reference RCB) to the Predicted RCB Implant and Surgeon-Selected Implant to examine how well the implants fit. The Predicted RCB Implant model and Reference RCB model were co-registered based on their inertial coordinate systems. Following co-registration of the Predicted RCB Implant and Reference RCB models based on their inertial coordinate systems, distances between the surfaces were computed. For each Reference RCB node (triangular surface mesh vertices) along its corresponding node surface normal, the nearest neighbor node on the Predicted RCB Implant model was resolved and node-to-node distance was computed (dist2surf; iso2mesh) [64]. The process was repeated to compare the Surgeon-Selected Implants to the Reference RCBs of each respective animal in the implant group (n=4). The calculated distances between the surfaces of the Predicted RCB Implant and the Surgeon-Selected Implant compared to the Reference RCB model were visualized as heat maps across the implant surface.

2.3.6. Statistical Analysis

Descriptive statistics (mean and SD) were calculated for volume and bounding box dimensions of the RCB dataset and the RCB-MS. A two-tailed Wilcoxon matched-pairs signed-rank test was performed with a significance threshold of $p < 0.05$ to determine if the calculated distances between the surfaces differed for the Predicted RCB Implant and Surgeon-Selected Implant comparison to the Reference RCB model.

2.4. Results

2.4.1. RCB Size Variability

The volumes of the RCBs from the YMP dataset ranged from 1345.0 to 2506.8 mm^3 (mean: 1798.7 ± 359.8 mm^3). The bounding box dimensions ranged in length between 18.7 to 23.8 mm in the volar-dorsal dimension (mean: 20.5 ± 1.6 mm), 14.9 to 20.0 mm in the proximal-distal dimension (mean: 16.8 ± 1.4 mm), and 10.6 to 13.8 in the radial-ulnar dimension (mean: 11.9 ± 1.1 mm). The volume of the RCB-MS was 2171 mm^3 with bounding box dimensions of 21.8 mm in the volar-dorsal dimension, 17.9 mm in the proximal-distal dimension, and 12.3 mm in the radial-ulnar dimension.

2.4.2. Age, Weight and Bone Size Relationships

The relationship between animal age and weight and RCB volume had an R^2 of 0.83 as determined by the multiple linear regression.

The linear regression for the three bounding box dimensions and RCB volume explained 91% of the variance in the volar-dorsal dimension ($R^2 = 0.91$, $p < 0.001$),

74% in the radial-ulnar dimension (R^2 = 0.74, p < 0.001), and 52% in the proximal-distal dimension (R^2 = 0.52, p < 0.001) (**Figure 2.3**).

2.4.3. Implant Sizes

The volume for the RCB of the largest animal that might be enrolled in our study was estimated to be 3266 mm^3, using equation 1 and age and weight of 24 months and 110 kg, respectively. The estimated volume of 3266 mm^3 was rounded up to 3500 mm^3, to provide some margin for error. The difference between the estimated largest RCB volume and the RCB-MS volume was 1329 mm^3. The volume increment between the 5 implants that spanned the volumes between the RCB-MS (2171 mm^3) and largest anticipated implant size (3500 mm^3) was 332.3 mm^3. To ensure the implants covered small to large animals, the target implant volumes ranged from 842 to 3500 mm^3. The generated set of implants had calculated volumes ranging from 986.9 to 4410.0 mm^3 (mean: 2460.4 ± 1176.6 mm^3) with bounding box dimensions ranging from 16.6 to 27.5 mm in the volar-dorsal dimension (mean: 22.0 ± 3.7 mm), 14.0 to 21.6 mm in the proximal-distal dimension (mean: 17.8 ± 2.6 mm), and 9.4 to 16.4 mm in the radial-ulnar dimension (mean: 12.9 ± 2.4 mm) (**Table 2.1**).

2.4.4. Validation of Implant Sizes

The average maximum distance between the Predicted RCB Implants and the Reference RCBs was 2.0 ± 0.4 mm (n=8) (**Figure 2.4**).

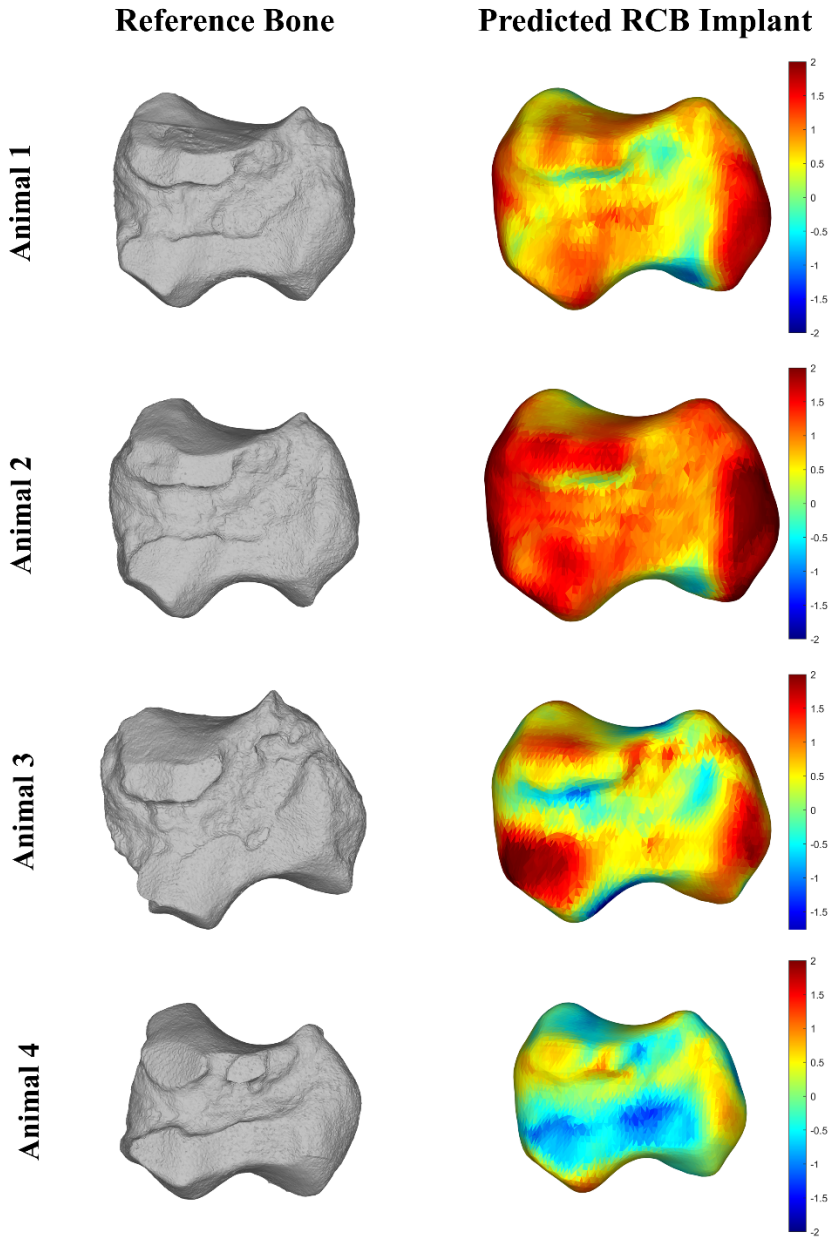

Figure 2.4. Heat maps were generated to reflect the calculated distances (mm) between the surfaces of the Predicted RCB implant and the Reference RCB for animals in the ligament transection group (n=4) of the *in vivo* study. Differences are displayed on the implant surface.

For the animals that received a CoCr implant, the average maximum distance between the Surgeon-Selected Implants and the Reference RCBs was 1.5 ± 0.2 mm (n=4) (**Figure 2.5**). The distance values between the implant surfaces and the Reference RCBs were smaller ($p < 0.001$) for the Surgeon-Selected Implants relative to the Predicted RCB Implants in three animals (Animals 5-7) and larger ($p < 0.0001$) in one animal (Animal 8).

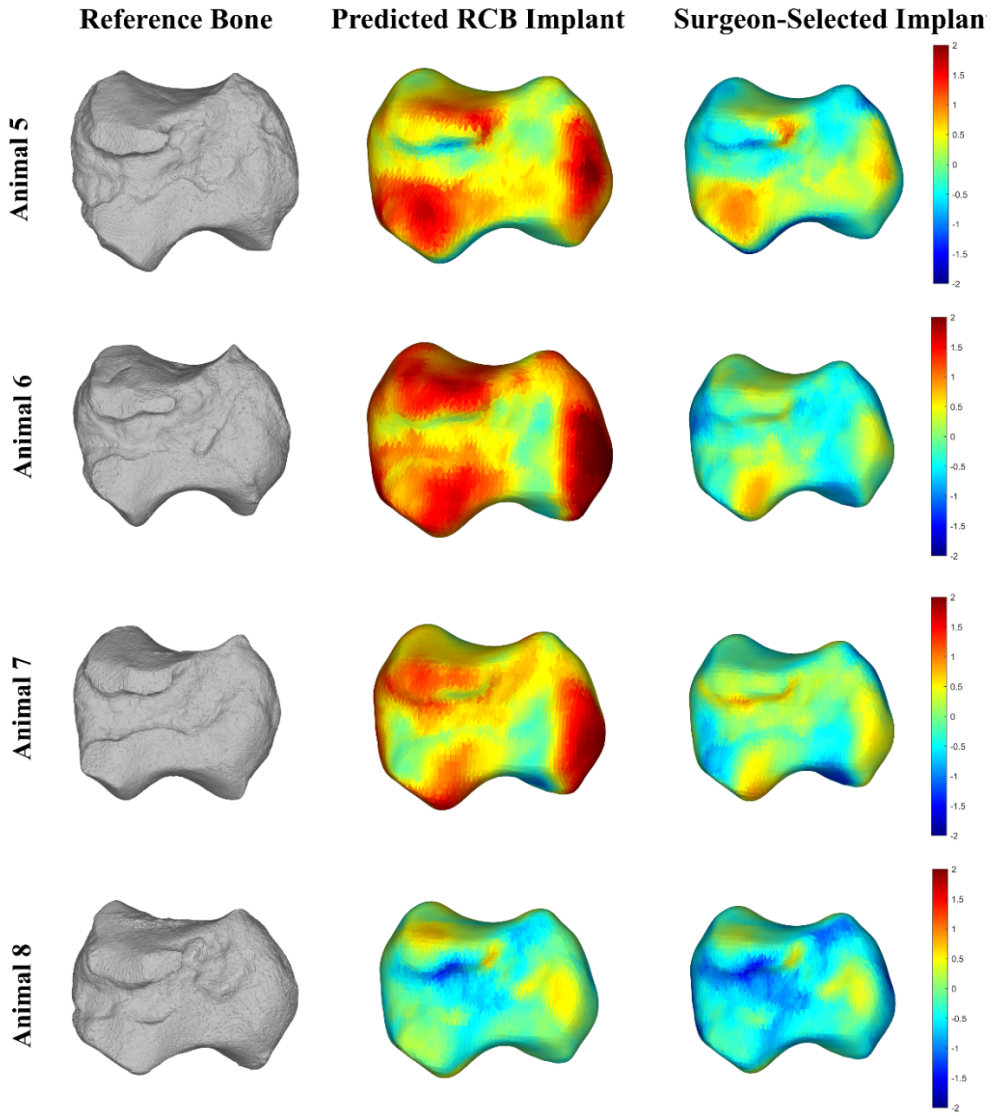

Figure 2.5. Heat maps of the distances between the Predicted RCB Implant and the Surgeon-Selected Implant compared to the Reference RCB for the animals in the implant group (n=4) of the *in vivo* study.

2.5. Discussion

The purpose of this study was to develop an approach for generating a set of implants for RCB replacement in the YMP as a model for human small bone hemiarthroplasty. To do so, we quantified the size of 35 YMP RCBs and then used multiple linear regression to define a relationship for estimating RCB volume from animal age and weight [Eqn 1]. We then generated a RCB-MS from the RCB dataset and scaled it using the linear regression equations [Eqn 2-4] to generate a set of 9 implants for our *in vivo* study. Finally, we examined how well our predicted implants fit in the animals from our *in vivo* study.

The 9 implants fabricated in this study encompassed the RCB dataset, providing a suitable size range for the animals included in the *in vivo* study (**Figure 2.6**). Of these, 5 implants fell within the bounding box dimensions of the 35 RCB dataset. To consider potential variations in animal size, an additional 4 implants were generated, 1 smaller and 3 larger (**Figure 2.6**). The bounding box dimensions across the set of implants increased incrementally by approximately 1 mm (mean: VD= 1.4 mm; PD= 0.9 mm; RU= 0.9 mm), a size scale comparable to commercially available small bone implants. For example, the Amandys pyrocarbon implant is available in eight sizes, with lengths ranging from 24 to 26 mm and with thickness sizes of 9 mm (small), 10.7 mm (medium), 12.4 mm (large), and 14.1 mm (extra-large) (Tornier SAS-Bioprofile Grenoble, France).[65,66] Similarly, the Adaptive Proximal Scaphoid Implant (APSI) varies in length from 16 to 18 mm and in height from 8 to 10 mm (Tornier SAS-Bioprofile Grenoble, France).[23,67]

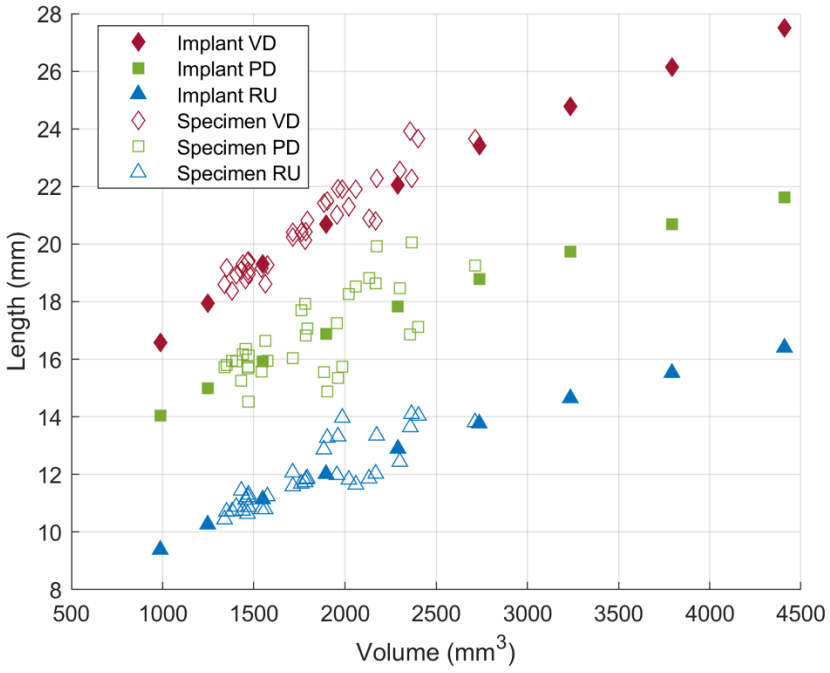

Figure 2.6. Volume and bounding box dimensions of the generated implants (n=9; filled diamonds) compared to the RCB dataset (n=18; open circles). The bounding box dimensions are represented by volar-dorsal (red), proximal-distal (green), and radial-ulnar (blue).

The motivation behind our approach was to design and determine implant size when preoperative imaging and animal specific implant fabrication are unfeasible due to constraints such as lead time and cost. Therefore, we investigated the use of age and weight to predict implant sizes for a RCB replacement in a porcine model. Similar approaches have been successfully applied to human knee and hip arthroplasty.[68–72] In the knee, height, weight, and gender have been identified as predictors for total knee component sizes, with a significant linear correlation observed between these demographic variables and femoral and tibial sizes, both with and without preoperative templating.[69,71] Shoe size and height were also found to be strong predictors for femoral and tibial components.[68,70] In the hip, a positive correlation was observed between templated and implanted acetabular

cup sizes, and between templated and implanted femoral stem sizes, using shoe size as a predictive variable.[72] Building on previous studies, our study found a strong correlation between demographic variables (animal age and weight) and RCB volume. However, the Predicted RCB Implant selected based on the animals age and weight was larger when compared to the Reference RCB model for each animal (**Figure 2.4-2.5**). Thus, our surgeon elected not to use the Predicted RCB Implant and instead selected a smaller implant compared to the Reference RCB model to avoid overpacking the joint which could increase the risk of implant instability. The use of a mean shaped bone has previously been suggested as a scalable template for implant design. Vafaeian et al. demonstrated that the mean shape of the talus, derived using statistical shape modeling, exhibited minimal variation across a population, supporting its use as a template for universal talar implants.[73] Islam et al. employed a volume-based isotropic scaling approach to categorize talus implants into standardized sizes, finding bone volume to be a reliable predictor of implant fit.[74] Our study built upon the methodologies of Vafaeian et al. and Islam et al. by using ShapeWorks Studio to generate a RCB-MS model that we then scaled to generate a set of 9 implants. Our scaling approach used a volume and linear regression of the bounding box dimensions [Eqn 2-4] to determine the anisotropic scaling factors. Although the approach yielded a total of 9 implants that encompass small and large animals expected in the YMP *in vivo* study, the calculated volume of the generated implant sizes overestimated the initial target implant volumes by an average of 10 % (**Table 2.1**).

Anisotropic scaling was applied to the RCB-MS using linear regression formulas [Eqn 2-4] that predict bounding box dimensions from volume. This approach was used because each bounding box dimension had a distinct relationship with volume, as indicated by the linear regression analyses. The analyses demonstrated that the volar-dorsal dimension accounted for most of the variation in RCB volume, suggesting that RCB bounding box dimensions do not develop uniformly. Similar to Islam et al.,[74] we also explored an isotropic scaling approach using the target implant volumes. The isotropic set of implants generated had calculated volumes that corresponded with the target implant volumes. The implants measured between 15.9 to 25.6 mm in the volar-dorsal dimension, 13.0 to 20.9 mm in the proximal-distal dimension, and 9.0 to 14.5 mm in the radial-ulnar dimension. However, as the implant sizes increased after the fifth largest implant, the increments in bounding box dimensions between implants were less than 1 mm. While isotropic scaling produced implants with calculated volumes equal to the target volumes, we aimed to ensure that each implant maintained approximately a 1 mm increment in each bounding box dimension, which favored the anisotropic approach.

This study has several limitations. First, the model's ability to accurately predict RCB volume for ages and weights outside the range used for the model development (age: 13.0–41.3 months; weight: 49.3–99.9 kg) remains uncertain, particularly since age and weight may be interdependent variables. Second, the relatively small sample size of the YMP RCB dataset (n=18) and the limited number of males (n=6) compared to females (n=12), likely could not capture sex

differences or bone variations, indicating the need for further validation with a larger dataset. Third, the sample size of the *in vivo* group that received a small bone replacement was limited (n=4), however the RCB dataset consisted of small incremental sizes which suggests the implant set generated is likely to fit the broad spectrum of YMP bones, though further validation with a larger sample size is needed. The generated set of implants also does not account for variations in RCB shape, for example differences in the curvatures of articulating surfaces, as it relies on scaling a RCB-MS. Additionally, potential implant designs derived from the modes of variation identified through statistical shape modeling were not explored. Future research should investigate combining different modes of variation to inform implant design. Lastly, the scaling ratios for each bounding box dimension were treated as independent variables due to the distinct relationship each dimension had with bone volume. After anisotropic scaling, the calculated implant volumes were larger than the target volumes (**Table 2.1**). Expressing the bounding box dimensions as interdependent, nonlinear variables could improve accuracy of fit and generate implants with calculated volumes closer to the target volume. Future studies should explore this alternative scaling approach.

2.6. Acknowledgments

The authors thank Scott Mc Allister for assistance in specimen acquisition and animal care and Janine Molino for consultation on the statistical analyses.

2.7. References

1. Rainbow MJ, Wolff AL, Crisco JJ, Wolfe SW. Functional kinematics of the wrist. *J Hand Surg Eur Vol*. 2016;41(1):7-21. doi:10.1177/1753193415616939
2. Wolfe SW, Kakar S. Chapter 13: Carpal Instability. In: Wolfe SW, Pederson WC, Kozin SH, Cohen MS, eds. *Green's Operative Hand Surgery*. Eighth Edition. Elsevier Health Sciences; 2022:488-497.
3. Adams BD, Kleinhenz BP, Guan JJ. Wrist Arthrodesis for Failed Total Wrist Arthroplasty. *J Hand Surg Am*. 2016;41(6):673-679. doi:10.1016/j.jhsa.2016.02.012
4. Rodriguez-Merchan EC, Tabeayo-Alvarez ED, Shojaie B, Kachooei AR. Total Wrist Arthrodesis: An Update on Indications, Technique and Outcomes. *Arch Bone Jt Surg*. 2023;11(3):144-153. doi:10.22038/ABJS.2022.65875.3154
5. Kay HF, Kang HP, Alluri R, Azad A, Ghiassi A. Proximal Row Carpectomy Versus 4-Corner Fusion: Incidence, Conversion to Fusion, and Cost. *J Hand Surg Am*. Published online February 20, 2020. doi:10.1016/j.jhsa.2019.12.010
6. Chim H, Moran SL. Long-Term Outcomes of Proximal Row Carpectomy: A Systematic Review of the Literature. *J Wrist Surg*. 2012;1(2):141-148. doi:10.1055/s-0032-1329547
7. Dacho AK, Baumeister S, Germann G, Sauerbier M. Comparison of proximal row carpectomy and midcarpal arthrodesis for the treatment of scaphoid nonunion advanced collapse (SNAC-wrist) and scapholunate advanced collapse (SLAC-wrist) in stage II. *J Plast Reconstr Aesthet Surg*. 2008;61(10):1210-1218. doi:10.1016/j.bjps.2007.08.007
8. Wagner ER, Srnec JJ, Fort MW, Barras LA, Rizzo M. Outcomes of Revision Total Wrist Arthroplasty. *J Am Acad Orthop Surg Glob Res Rev*. 2021;5(3). doi:10.5435/JAAOSGlobal-D-21-00035
9. Cavaliere CM, Chung KC. A systematic review of total wrist arthroplasty compared with total wrist arthrodesis for rheumatoid arthritis. *Plast Reconstr Surg*. 2008;122(3):813-825. doi:10.1097/PRS.0b013e318180ece3
10. Nair R. Review article: Total wrist arthroplasty. *J Orthop Surg (Hong Kong)*. 2014;22(3):399-405.
11. Carlson JR, Simmons BP. Total wrist arthroplasty. *J Am Acad Orthop Surg*. 1998;6(5):308-315.
12. Krukhaug Y, Lie SA, Havelin LI, Furnes O, Hove LM. Results of 189 wrist replacements. A report from the Norwegian Arthroplasty Register. *Acta Orthop*. 2011;82(4):405-409. doi:10.3109/17453674.2011.588858
13. Gaspar MP, Lou J, Kane PM, Jacoby SM, Osterman AL, Culp RW. Complications Following Partial and Total Wrist Arthroplasty: A Single-Center Retrospective Review. *J Hand Surg Am*. 2016;41(1):47-53.e4. doi:10.1016/j.jhsa.2015.10.021

14. Vance MC, Packer G, Tan D, Crisco JJT, Wolfe SW. Midcarpal hemiarthroplasty for wrist arthritis: rationale and early results. *J Wrist Surg*. 2012;1(1):61-68. doi:10.1055/s-0032-1323644
15. Carlson Strother CR, Moran SL, Rizzo M. Small Joint Arthroplasty of the Hand: An Update on Indications, Outcomes, and Complications. *J Am Acad Orthop Surg*. 2023;31(15):793-801. doi:10.5435/JAAOS-D-23-00034
16. Joyce TJ, Unsworth A. A literature review of "failures" of the Swanson finger prosthesis in the metacarpophalangeal joint. *Hand Surg*. 2002;7(1):139-146. doi:10.1142/s0218810402000881
17. Swanson AB, Swanson GG, Maupin BK, Hynes DE, Jindal P. Failed carpal bone arthroplasty: causes and treatment. *J Hand Surg Am*. 1989;14(2 Pt 2):417-424. doi:10.1016/0363-5023(89)90128-7
18. Rex JC, Crawford Z, Stout J, Stern PJ. Thirty-Three-Year Follow-up Following Silicone Scaphoid Arthroplasty: A Case Report. *JBJS Case Connect*. 2024;14(2):1-5. doi:10.2106/JBJS.CC.24.00027
19. Viljakka T, Tallroth K, Vastamäki M. Long-term outcome (22-36 years) of silicone lunate arthroplasty for Kienbock's disease. *J Hand Surg Eur Vol*. 2014;39(4):405-415. doi:10.1177/1753193413489460
20. Kistler U, Weiss APC, Simmen BR, Herren DB. Long-term results of silicone wrist arthroplasty in patients with rheumatoid arthritis. *J Hand Surg Am*. 2005;30(6):1282-1287. doi:10.1016/j.jhsa.2005.07.009
21. Papalia R, Tecame A, Torre G, D'Adamio S, Maffulli N, Denaro V. Small joints replacement for hand osteoarthritis: a systematic review. *Br Med Bull*. 2015;116:55-68. doi:10.1093/bmb/ldv024
22. Nilsson A, Wiig M, Alnehill H, et al. The Artelon CMC spacer compared with tendon interposition arthroplasty. *Acta Orthop*. 2010;81(2):237-244. doi:10.3109/17453671003635835
23. Ferrero M, Carità E, Giacalone F, et al. Prosthetic Replacement of the Scaphoid Proximal Pole: Should It Be the Future? *Hand (N Y)*. 2022;17(5):899-904. doi:10.1177/1558944720974120
24. Bellemère P. Pyrocarbon implants for the hand and wrist. *Hand Surg Rehabil*. 2018;37(3):129-154. doi:10.1016/j.hansur.2018.03.001
25. Henry M. Outcomes assessment of lunate replacement arthroplasty with intrinsic carpal ligament reconstruction in Kienböck's disease. *Hand (N Y)*. 2014;9(3):364-369. doi:10.1007/s11552-014-9624-z
26. Vitale MA, Taylor F, Ross M, Moran SL. Trapezium prosthetic arthroplasty (silicone, Artelon, metal, and pyrocarbon). *Hand Clin*. 2013;29(1):37-55. doi:10.1016/j.hcl.2012.08.020
27. Swanson AB, de Groot Swanson G, DeHeer DH, et al. Carpal bone titanium implant arthroplasty. 10 years' experience. *Clin Orthop Relat Res*. 1997;(342):46-58.
28. Kaarela OI, Raatikainen TK, Torniainen PJ. Silicone replacement arthroplasty for Kienböck's disease. *J Hand Surg Br*. 1998;23(6):735-740. doi:10.1016/s0266-7681(98)80086-7
29. Hagert CG, Eiken O, Ohlsson NM, Aschan W, Movin A. Metacarpophalangeal joint implants. I. Roentgenographic study on the

silastic finger joint implant, swanson design. *Scand J Plast Reconstr Surg*. 1975;9(2):147-157.
30. Hay EL, Bomberg BC, Burke C, Misenheimer C. Long-term results of silicone trapezial implant arthroplasty. *J Arthroplasty*. 1988;3(3):215-223. doi:10.1016/s0883-5403(88)80018-4
31. Huish Jr EG, Lum Z, Bamberger HB, Trzeciak MA. Failure of wrist hemiarthroplasty. *Hand*. 2017;12(4):369-375.
32. Zhang C, Chen H, Fan H, et al. Carpal bone replacement using personalized 3D printed tantalum prosthesis. *Front Bioeng Biotechnol*. 2023;11:1234052. doi:10.3389/fbioe.2023.1234052
33. Cioffi A, Rovere G, Bosco F, et al. Treatment of Scaphoid Non-Unions with Custom-Made 3D-Printed Titanium Partial and Total Scaphoid Prostheses and Scaphoid Interosseous Ligament Reconstruction. *Healthcare (Basel)*. 2023;11(24):3123. doi:10.3390/healthcare11243123
34. Rossello MI. A case of total scaphoid titanium custom-made 3D-printed prostheses with one-year follow-up. *Case Reports Plast Surg Hand Surg*. 2020;7(1):7-12. doi:10.1080/23320885.2019.1708203
35. Rossello MI. Short-term findings of a custom-made 3D-printed titanium partial scaphoid prosthesis and scapholunate interosseous ligament reconstruction. *BMJ Case Rep*. 2021;14(7):e241090. doi:10.1136/bcr-2020-241090
36. Lebowitz C, Massaglia J, Hoffman C, et al. The Accuracy of 3D Printed Carpal Bones Generated from Cadaveric Specimens. *Arch Bone Jt Surg*. 2021;9(4):432-438. doi:10.22038/abjs.2020.50236.2495
37. Honigmann P, Sharma N, Schumacher R, Rueegg J, Haefeli M, Thieringer F. In-Hospital 3D Printed Scaphoid Prosthesis Using Medical-Grade Polyetheretherketone (PEEK) Biomaterial. *Biomed Res Int*. 2021;2021:1301028. doi:10.1155/2021/1301028
38. Ma ZJ, Liu ZF, Shi QS, et al. Varisized 3D-Printed Lunate for Kienböck's Disease in Different Stages: Preliminary Results. *Orthop Surg*. 2020;12(3):792-801. doi:10.1111/os.12681
39. Xie M ming, Tang K lai, Yuan C song. 3D printing lunate prosthesis for stage IIIc Kienböck's disease: a case report. *Arch Orthop Trauma Surg*. 2018;138(4):447-451. doi:10.1007/s00402-017-2854-0
40. Sing SL, An J, Yeong WY, Wiria FE. Laser and electron-beam powder-bed additive manufacturing of metallic implants: A review on processes, materials and designs. *J Orthop Res*. 2016;34(3):369-385. doi:10.1002/jor.23075
41. Wong KC. 3D-printed patient-specific applications in orthopedics. *Orthop Res Rev*. 2016;8:57-66. doi:10.2147/ORR.S99614
42. He S, Zhu J, Jing Y, et al. Effect of 3D-Printed Porous Titanium Alloy Pore Structure on Bone Regeneration: A Review. *Coatings*. Published online April 19, 2025. doi:10.3390/coatings14030253
43. Kelly CN, Wang T, Crowley J, et al. High-strength, porous additively manufactured implants with optimized mechanical osseointegration. *Biomaterials*. 2021;279:121206. doi:10.1016/j.biomaterials.2021.121206

44. Viljakka T, Tallroth K, Vastamäki M. Long-Term Clinical Outcome After Titanium Lunate Arthroplasty for Kienböck Disease. *J Hand Surg Am*. 2018;43(10):945.e1-945.e10. doi:10.1016/j.jhsa.2018.02.009
45. Tack P, Victor J, Gemmel P, Annemans L. 3D-printing techniques in a medical setting: a systematic literature review. *Biomed Eng Online*. 2016;15(1):115. doi:10.1186/s12938-016-0236-4
46. Pearce AI, Richards RG, Milz S, Schneider E, Pearce SG. Animal models for implant biomaterial research in bone: a review. *Eur Cell Mater*. 2007;13:1-10. doi:10.22203/ecm.v013a01
47. Thillemann JK, Dremstrup L, Hansen TB, Stilling M. The mechanical fixation of a cementless conical cup in cortical versus cancellous trapezial bone: an experimental study. *J Hand Surg Eur Vol*. 2021;46(2):146-153. doi:10.1177/1753193420963255
48. Stilling M, Dremstrup L, Hansen TB, Thillemann JK. Superior bone fixation of conical compared with hemispherical trapezial cup design: an experimental radiostereometry study. *J Exp Orthop*. 2023;10(1):127. doi:10.1186/s40634-023-00692-y
49. Hansen TB, Homilius M. Failed total carpometacarpal joint prosthesis of the thumb: results after resection arthroplasty. *Scand J Plast Reconstr Surg Hand Surg*. 2010;44:171-174.
50. Sehjal R, Rusli W, Kedgley AE, Sagmeister ML, Williamson M, Smith A. Biomechanical Comparison of 5 Different Fixation Constructs in a Trapeziometacarpal Joint Arthrodesis Model. *J Hand Surg Am*. 2024;49(10):1036.e1-1036.e9. doi:10.1016/j.jhsa.2022.12.010
51. Waris E, Ashammakhi N, Lehtimäki M, et al. Long-term bone tissue reaction to polyethylene oxide/polybutylene terephthalate copolymer (Polyactive) in metacarpophalangeal joint reconstruction. *Biomaterials*. 2008;29(16):2509-2515. doi:10.1016/j.biomaterials.2008.02.013
52. Ochman S, Doht S, Paletta J, Langer M, Raschke MJ, Meffert RH. Comparison between locking and non-locking plates for fixation of metacarpal fractures in an animal model. *J Hand Surg Am*. 2010;35(4):597-603. doi:10.1016/j.jhsa.2010.01.002
53. Doht S, Jansen H, Meffert R, Frey S. Higher stability with locking plates in hand surgery? Biomechanical investigation of the TriLock system in a fracture model. *Int Orthop*. 2012;36(8):1641-1646. doi:10.1007/s00264-012-1524-7
54. Massengill JB, Alexander H, Parson JR, Schecter MJ. Mechanical analysis of Kirschner wire fixation in a phalangeal model. *J Hand Surg Am*. 1979;4(4):351-356. doi:10.1016/s0363-5023(79)80073-8
55. Massengill JB, Alexander H, Langrana N, Mylod A. A phalangeal fracture model--quantitative analysis of rigidity and failure. *J Hand Surg Am*. 1982;7(3):264-270. doi:10.1016/s0363-5023(82)80177-9
56. Kaiser EE, Waters ES, Fagan MM, et al. Characterization of tissue and functional deficits in a clinically translational pig model of acute ischemic stroke. *Brain Res*. 2020;1736:146778. doi:10.1016/j.brainres.2020.146778
57. Altieri MK, Badida R, Vaughan QM, Molino J, Akelman E, Crisco JJ. Biomechanical evaluation of the porcine carpus as a potential preclinical

animal model for the human carpus. *J Biomech*. 2024;177:112429. doi:10.1016/j.jbiomech.2024.112429
58. Stoeckl BD, Zlotnick HM, Farrell MJ, et al. The porcine accessory carpal bone as a model for biologic joint replacement for trapeziometacarpal osteoarthritis. *Acta Biomater*. 2021;129:159-168. doi:10.1016/j.actbio.2021.05.011
59. Behrends DA, Khendek L, Gao C, Zayed N, Henderson JE, Martineau PA. Characterization of a Pre-Clinical Mini-Pig Model of Scaphoid Non-Union. *J Funct Biomater*. 2015;6(2):407-421. doi:10.3390/jfb6020407
60. Badida R, Garcia-Lopez E, Sise C, Moore D, Crisco J. An Approach to Robotic Testing of the Wrist Using 3-D Imaging and a Hybrid Control Strategy. *J Biomech Eng*. 2020;142(6):064501. doi:10.1115/1.4046050
61. Coburn JC, Upal MA, Crisco JJ. Coordinate systems for the carpal bones of the wrist. *J Biomech*. 2007;40(1):203-209. doi:10.1016/j.jbiomech.2005.11.015
62. Crisco JJ, McGovern RD. Efficient calculation of mass moments of inertia for segmented homogeneous three-dimensional objects. *J Biomech*. 1998;31(1):97-101.
63. Cates J, Elhabian S, Whitaker R. Chapter 10 - ShapeWorks: Particle-Based Shape Correspondence and Visualization Software. In: Zheng G, Li S, Székely G, eds. *Statistical Shape and Deformation Analysis: Methods, Implementation and Applications*. Academic Press, an imprint of Elsevier; 2017:257-298. doi:10.1016/B978-0-12-810493-4.00012-2
64. Fang Q, Boas DA. Tetrahedral mesh generation from volumetric binary and grayscale images. In: IEEE; 2009:1142-1145.
65. Bellemère P, Maes-Clavier C, Loubersac T, Gaisne E, Kerjean Y. Amandys(®) implant: novel pyrocarbon arthroplasty for the wrist. *Chir Main*. 2012;31(4):176-187. doi:10.1016/j.main.2012.07.013
66. Bellemère P, Marcuzzi A. 28 Pyrocarbon Implants in the Wrist: Amandys and RCPI. In: *Arthroplasty in Hand Surgery*. 1. Edition. Thieme Verlag; 2021. doi:10.1055/b-0041-182712
67. Pequignot JR, Lussiez B, Allieu Y. Implant adaptatif du scaphoïde proximal. *Chirurgie de la Main*. 2000;19(5):276-285. doi:10.1016/S1297-3203(00)73492-5
68. Naylor BH, Butler JT, Kuczynski B, Bohm AR, Scuderi GR. Can Component Size in Total Knee Arthroplasty Be Predicted Preoperatively?-An Analysis of Patient Characteristics. *J Knee Surg*. 2023;36(9):965-970. doi:10.1055/s-0042-1748902
69. Bhowmik-Stoker M, Scholl L, Khlopas A, et al. Accurately Predicting Total Knee Component Size without Preoperative Radiographs. *Surg Technol Int*. 2018;33:337-342.
70. Rehman H, MacDonald DRW, Smith M, Zainudin S, Robertson G, Mitchell M. A novel technique for estimating component sizes in total knee arthroplasty. *Int J Surg*. 2018;52:7-10. doi:10.1016/j.ijsu.2018.01.048
71. Sershon RA, Courtney PM, Rosenthal BD, Sporer SM, Levine BR. Can Demographic Variables Accurately Predict Component Sizing in Primary

Total Knee Arthroplasty? *J Arthroplasty*. 2017;32(10):3004-3008. doi:10.1016/j.arth.2017.05.007

72. Sahemey R, Moores TS, Meacher H, Youssef B, Khan S, Evans CR. Anthropometric method for estimating component sizes in total hip arthroplasty. *World J Orthop*. 2021;12(11):859-866. doi:10.5312/wjo.v12.i11.859
73. Vafaeian B, Riahi HT, Amoushahi H, Jomha NM, Adeeb S. A feature-based statistical shape model for geometric analysis of the human talus and development of universal talar prostheses. *J Anat*. 2022;240(2):305-322. doi:10.1111/joa.13552
74. Islam K, Dobbe A, Duke K, et al. Three-dimensional geometric analysis of the talus for designing talar prosthetics. *Proc Inst Mech Eng H*. 2014;228(4):371-378. doi:10.1177/0954411914527741

Chapter 3: In Vitro Biomechanics of the Yucatan Minipig Carpus After Ligament Transection, Bone Resection, and Small Bone Replacement

Vaughan QM, Badida R, Molino J, Akelman E, Crisco JJ. In Vitro Biomechanics of the Yucatan Minipig Carpus After Ligament Transection, Bone Resection, and Small Bone Replacement. (PENDING SUBMISSION).

3.1. Abstract

Treatment options for carpal pathologies are limited, and the biomechanical effects of surgical interventions, particularly carpal bone replacement, remain poorly understood. Establishing a preclinical animal model may advance treatment development and inform implant designs that better restore native wrist motion. This study used the Yucatan minipig (YMP) carpus, specifically the YMP radial carpal bone (RCB) as a model for the human scaphoid, to quantify multidirectional biomechanics in the following conditions: intact, transection of all ligaments connected to the RCB (ALC), resection of the RCB (no RCB), and treatment with a 3D-printed polylactic acid radial carpal bone hemiarthroplasty (RCBH). Nine YMP forelimbs were tested in 28 range of motion (ROM) directions, pronation-supination, and volar-dorsal translation using a six-degree-of-freedom robotic system. Mixed models examined differences in direction and testing conditions. ROM increased ($p<0.05$) in 18 directions for ALC, 19 directions for no RCB, and 22 directions for RCBH conditions relative to intact. Of the four primary directions, extension (ALC= 17.4°; No RCB= 16.8°; RCBH= 18.5°) and radial deviation (ALC= 10.0°; No RCB= 10.8°; RCBH= 11.2°) increased compared to intact (extension= 9.4°; radial deviation= 3.3°). In all conditions: at neutral, pronation exceeded supination; at max ROM, supination exceeded pronation; volar translation increased; and dorsal translation decreased compared to intact. All conditions increased ROM relative to intact, and the implant did not restore native biomechanics. However, the similar elliptical motion envelope to humans suggests the potential of the YMP as a promising preclinical model of the wrist.

3.2. Introduction

Wrist ligament injuries can lead to carpal instability and eventual development of osteoarthritis (OA), significantly impacting patient quality of life. In end-stage disease, surgical treatments include wrist fusion (arthrodesis),[1,2] proximal row carpectomy,[3–5] and total wrist arthroplasty.[6–9] However, these treatment modalities can result in complications, such as hardware failure,[2] reduced grip strength,[4,5] and limited range of motion.[10,11] Hemiarthroplasty approaches, specifically carpal bone replacements, may provide a motion-preserving alternative due to reduced hardware and limited bone resection.[12,13] However, the biomechanical effects of carpal bone replacement have not been well characterized, highlighting the need for further research to define and develop effective, motion-preserving therapies for wrist OA.

Animal models and *in vitro* testing have been instrumental in developing successful treatments for joint degeneration, particularly in the knee. However, there is currently no well-established animal model for studying wrist biomechanics or implant design. While small animal models are commonly used for proof-of-concept studies,[14,15] their carpal bone size limits evaluation of implantable devices. Larger animal models, such as sheep and pigs, offer anatomical and biomechanical similarities to humans [15–17] that may better support translational wrist research.

The Yucatan minipig (YMP) has recently been proposed as a potential animal model for the human wrist based on similarities in carpal bone anatomy,[18] bone composition [17] and ligamentous anatomy.[19] Previous studies have used the YMP

radial carpal bone (RCB) to model scaphoid nonunion [18] and the YMP accessory carpal bone as a model for the human trapezium to investigate a biologic joint replacement for trapeziometacarpal OA.[20] Additionally, *in vitro* YMP biomechanics after transection of the radial intermediate and dorsal intercarpal ligaments, homologous to the human scapholunate interosseous and dorsal intercarpal ligaments, have been reported.[19] However, only minimal increases in range of motion were observed after these specific ligament transections, indicating that additional stabilizing structures may contribute to carpal stability in this model.

To further support the use of the YMP as a model for evaluating novel implant designs and implant biomechanics, the YMP carpus must be assessed under injured conditions and after stabilization with a carpal bone implant. To do so, this study quantified the biomechanics of the YMP carpus under intact, ligament transection, bone resection, and small bone replacement conditions. We hypothesized that range of motion (ROM) would (1) increase following transection of all ligaments connected to the RCB; (2) further increase after RCB resection; and (3) be restored to intact values following stabilization with a small bone replacement.

3.3. Methods

3.3.1. Specimen Acquisition and Preparation

Nine YMP forelimbs (3 pairs, 3 unpaired) were harvested from animals used in an unrelated study. The cohort included 3 females and 3 males aged 13.0 to 20.1 months (mean:18.5 ± 2.7 months) and weighing 50.5 to 61.0 kilograms (kg) (mean:

56.0 ± 4.4 kg) (Premier BioSource, Ramona, CA). All animals were acquired following IACUC review and approval.

Following harvest, forelimbs were prepared by removing the skin, disarticulating the phalanges, and trimming the radius and ulna at the radial glenoid cavity. The superficial dorsal extensor (SDE), superficial radial carpal flexor (SRCF), and the superficial ulnar carpal flexor (SUCF) were isolated and whip-stitched for biomechanical testing. The deep radial carpal flexor tendon (DRCFT) was additionally isolated for implant fixation. The distal metacarpals and proximal radius and ulna were potted in fast-setting urethane resin (SmoothOn, Macungie, PA). A fiducial collar with five non-coplanar holes was added to the potting fixtures to allow registration of the specimen-specific anatomical coordinate system to the global coordinate system of a robotic testing system (ROB_{GCS}).

3.3.2. CT Imaging and Post-Processing

Potted forelimbs were imaged using a clinical CT scanner (0.4 mm x 0.4 mm x 0.625 mm, GE Healthcare, Chicago, IL). The metacarpals, radius, ulna, and fiducial collars were segmented (Mimics v22, Materialise, Leuven, Belgium) using density-based thresholding with manual editing, and exported as three-dimensional (3D) surface models of the bones as closed triangular meshes with no triangle reduction and minimal smoothing (iterations: 1; smooth factor: 0.030). Surface models were imported into Geomagic Wrap (Geomagic Wrap 2021; 3D Systems, SC) to define specimen-specific anatomical coordinate systems using anatomical landmarks on the metacarpals, radius, and ulna, following previously

described methods for homologous human wrist testing.[21] Fiducial points on each potting fixture were labeled for registration of the specimen to the ROB_{GCS}.

3.3.3. Ligament Sectioning, Bone Resection, and Insertion of a Small Bone Implant

Each forelimb underwent sequential testing under four conditions: intact, all ligaments cut (ALC), RCB resection (no RCB), and re-stabilization with a polylactic acid 3D-printed small bone implant (RCBH) (**Figure 3.1**). For the ALC condition, a 2-inch sagittal capsular incision centered above the RCB and intermediate carpal bone (ICB) was made, and all ligamentous attachments to the RCB were transected. Complete transection was confirmed by temporary removal and replacement of the RCB, followed by capsular closure with interrupted sutures.

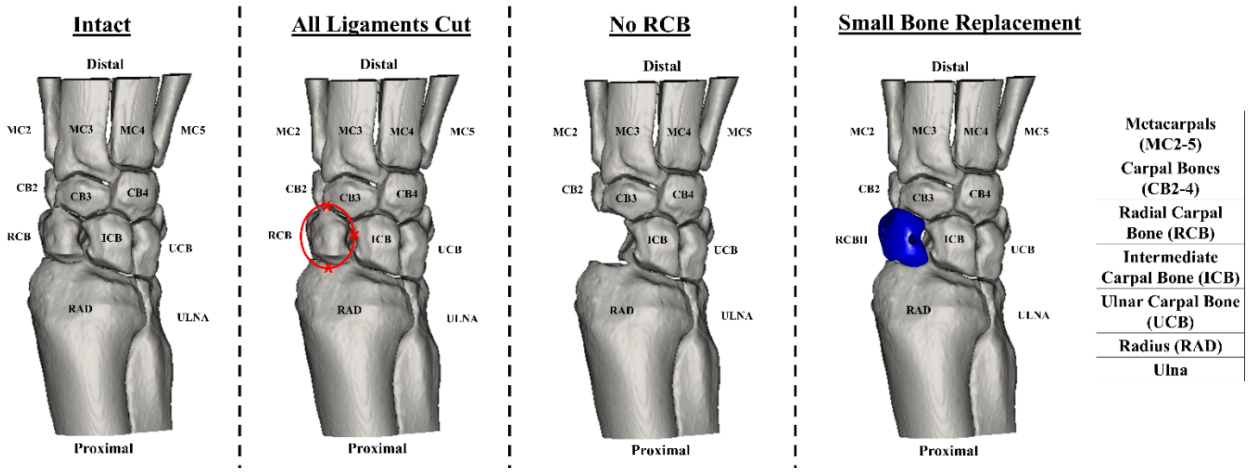

Figure 3.1. Bone models (dorsal view) of the YMP carpus depicting the testing conditions: (A) intact; (B) all ligaments cut (ALC) meaning transection of all ligaments connected to the radial carpal bone (RCB); (C) no RCB meaning the bone was resected from the carpus; and (D) replacement of the RCB with a radial carpal bone hemiarthroplasty (RCBH; blue). The testing procedure for multidirectional range of motion (MROM), pronation/supination range of motion (PSROM), and translational range of motion (TROM) was performed after each condition.

For the no RCB condition, the capsule was reopened, the RCB removed, and the capsule reclosed. For the RCBH condition, three predicted implant sizes were selected based on animal age and weight using a predictive model.[22] Optimal implant size was determined by subjective assessment of fit through joint manipulation and articulation with the distal radius and proximal CB2 and CB3. The implant was secured with a suture anchor (~3 mm length, ~2.5 mm diameter) placed into the ICB and the DRCFT was passed through the volar-dorsal tendon port and sutured to residual ligament on the dorsal face of the ICB. Anchor sutures were passed through radial-ulnar through-holes and secured using square knots. Following implant fixation, the capsule was closed. Robotic testing was performed after capsule closure for each condition.

3.3.4. Biomechanical Testing and Data Processing

Biomechanical testing of each forelimb was performed using a 6-DOF robot (KUKA KR6 R700, Augsburg, DE). The robot and load cell were registered using a LabView based software simVITRO (Cleveland Clinic, OH) and a 6-DOF digitizing probe (Optotrak, NDI, Ontario, CA). Specimens were mounted on an L-shaped fixture, with the radius/ulna secured to the robot base and the metacarpal to the end-effector. Constant force springs (4.45 N each; McMaster-Carr, Robbinsville, NJ) were attached to the whip-stitched tendons (SDE, SRCF, and SUCF) (**Figure 3.2**).

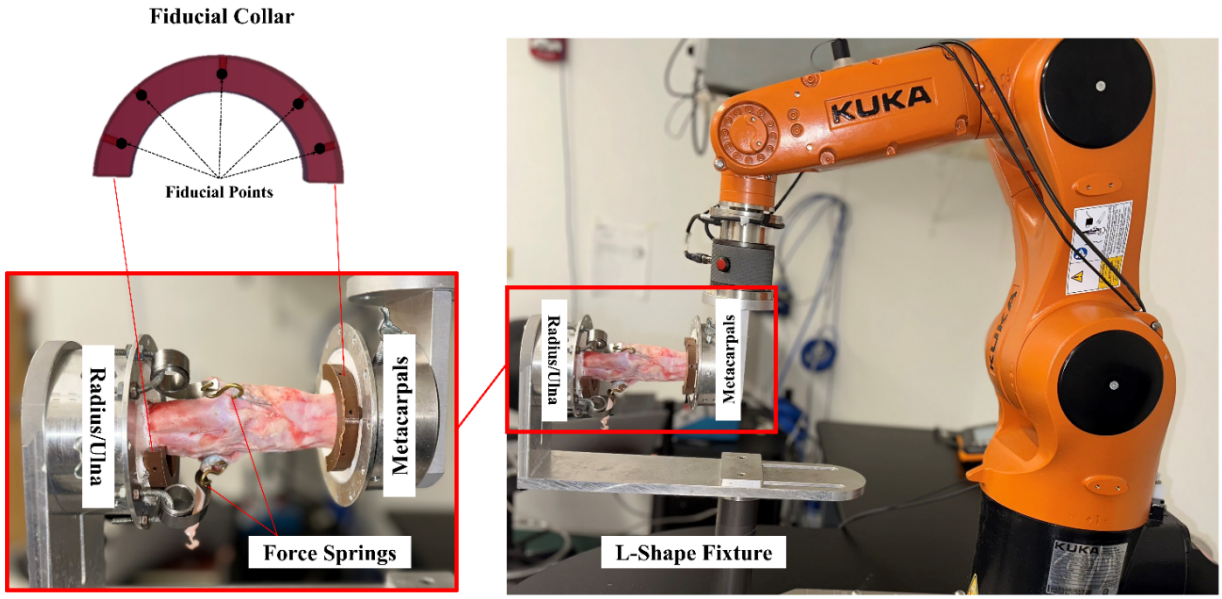

Figure 3.2. Right YMP forelimb mounted on the KUKA robot for multidirectional ROM, pronation and supination ROM, and volar/dorsal translation testing. The radius and ulna are fixed to the base using an L-shaped fixture and the metacarpals are secured to the end-effector of the robot. Force springs are attached to the flexor and extensor tendons. Fiducial collars used for digitization to register the specimen in the robotic coordinate system are included in the metacarpal and radius/ulna potting mixtures.

Fiducial markers on the metacarpals and radius/ulna were digitized to register specimen-specific anatomical coordinate systems to the ROB_{GCS}. Joint axes included flexion-extension (Z; radius fixed), pronation-supination (Y; metacarpals fixed), and a floating radioulnar deviation axis (X). The forelimb was positioned in a neutral configuration (0^0 flexion-extension, 0^0 radial-ulnar deviation, 0 Nm pronation-supination torque, 0 N forces), with residual forces and torques of less than ± 1 N and ± 0.05 Nm.

Three testing protocols were performed: multidirectional range of motion (MROM), pronation/supination ROM (PSROM), and translational ROM (TROM). In MROM, metacarpals were rotated in 28 directions (4 primary, 24 coupled) at

1°/sec until a resultant torque of 1 Nm was achieved; testing was manually stopped if fixture collision risked before reaching 1 Nm. Data were processed using a previously established methodology.[19]

For the MROM testing, ROM was computed as the resultant of flexion-extension and radial-ulnar deviation angles of the metacarpals relative to the radius/ulna with respect to the neutral position. Torque-rotation curves were fitted using fifth-order polynomials (MATLAB, MathWorks, Natick, MA) to quantify ROM and stiffness across all directions. ROM was defined as metacarpals rotation at 1 Nm, average stiffness was defined as the inverse of the ROM, and final stiffness was calculated as the slope of the fitted curve between 0.75 and 1 Nm. A total of 1008 tests were performed, 112 of which were manually stopped. Of the 112 manually stopped tests, 36 exceeded an established threshold of 0.5 Nm required for polynomial extrapolation to estimate ROM, while the remaining 76 were recorded as missing. For the PSROM protocol, pronosupination was performed at neutral and at maximum ROM previously identified in the ulnar-flexion direction (UF75; 75° from ulnar deviation in the flexion direction). At each orientation, the carpus was pronated and supinated at 1°/sec until a resultant torque of 1 Nm was reached. For the TROM protocol, the metacarpals were translated in the volar and dorsal directions at a rate of 1 mm/sec until a force of 30 N was achieved in each direction, while the carpus remained in the neutral position. For PSROM, ROM was defined as rotation about the pronation-supination axis at 1 Nm, whereas for TROM, ROM was defined as displacement at 30 N. Torque-rotation and load displacement curves were fitted using fifth-order polynomials, and final stiffness

was calculated as the slope of the fitted curves between 0.75 and 1 Nm for PSROM and between 22.5 and 30 N for TROM.

3.3.5. Statistical Analysis

Mixed models were utilized to evaluate the differences in ROM and stiffness (average and final) as a function of testing direction and testing condition (Intact, ALC, No RCB, RCBH). Mixed models were chosen for the analytic method as they allow appropriate handling of data structures associated with repeated measurements and maximize the information from specimens with missing observations. The outcome distribution and model residuals were examined to determine the distribution and link function to be applied to each model. To satisfy the assumption of normality, the outcomes were logarithmically transformed where necessary. Classical sandwich estimation was used to further protect against possible model misspecification. Pairwise comparisons between testing conditions (Intact, ALC, No RCB, RCBH) were conducted within the model via orthogonal contrasts. The Holm test was used to correct for multiple comparisons, maintaining a 2-tailed familywise alpha at 0.05 across the hypotheses tested. Adjusted p-values and model-based means and 95% confidence intervals (CIs) are reported. An adjusted p-value < 0.05 was used to determine statistical significance. All analyses were conducted in SAS version 9.4 (SAS Institute Inc., Cary, NC).

3.4. Results

3.4.1. All Ligaments Cut Biomechanics (ALC)

All specimen intact data were previously reported in a separate study.[19] Relative to intact, ALC ROM increased ($p<0.05$) in 18 out of 28 directions. The greatest ROM remained in the UF75 direction at 109.4^0 (CI: 95.7, 125.0), a 22.3^0 increase ($p<0.05$) from intact. Of the four primary anatomical directions, ROM increased in extension by (+8.0^0 to 17.4^0, CI: 14.2, 21.3; $p<0.05$) and radial deviation (+6.6^0 to 10.0^0, CI: 6.7, 14.7; $p<0.05$) (**Figure 3.3**). Average stiffness decreased in 16 of 28 directions, including extension (0.05 Nm/°, CI: 0.04, 0.06), radial deviation (0.11 Nm/°, CI: 0.09, 0.15), and ulnar deviation (0.09 Nm/°, CI: 0.06, 0.12) (**Figure 3.4**). Final stiffness increased ($p<0.05$) in 8 directions, including radial deviation (3.05 Nm/^{0}, CI: 1.82, 5.11) (**Table 3.1**).

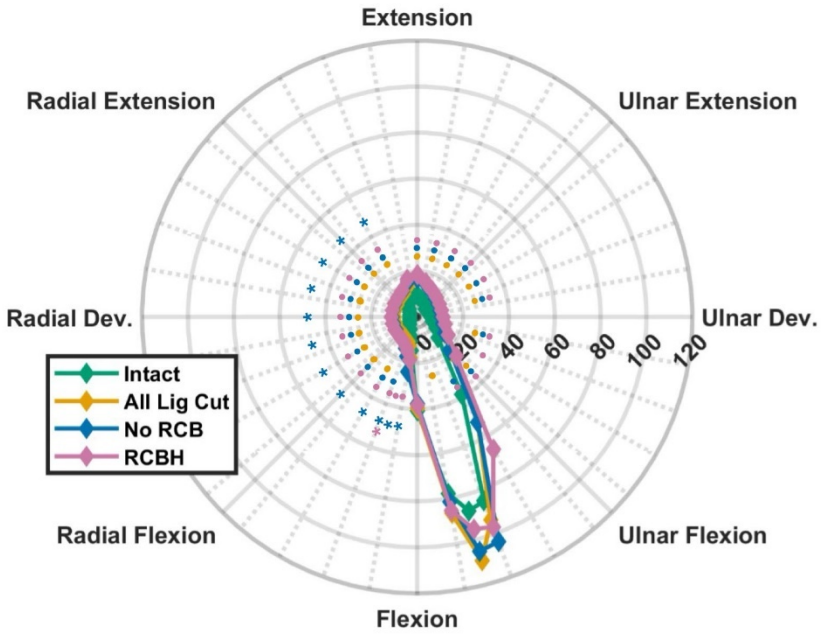

Figure 3.3. Average range of motion envelopes across the 28 motion directions for each condition: (A) intact, (B) all ligaments cut (ALC), (C) no radial carpal bone (RCB), and (D) small bone replacement with a radial carpal bone hemiarthroplasty (RCBH). Significant differences (p-values < 0.05) relative to intact are shown with a dot (•) and relative to ALC are shown with an asterisk (*).

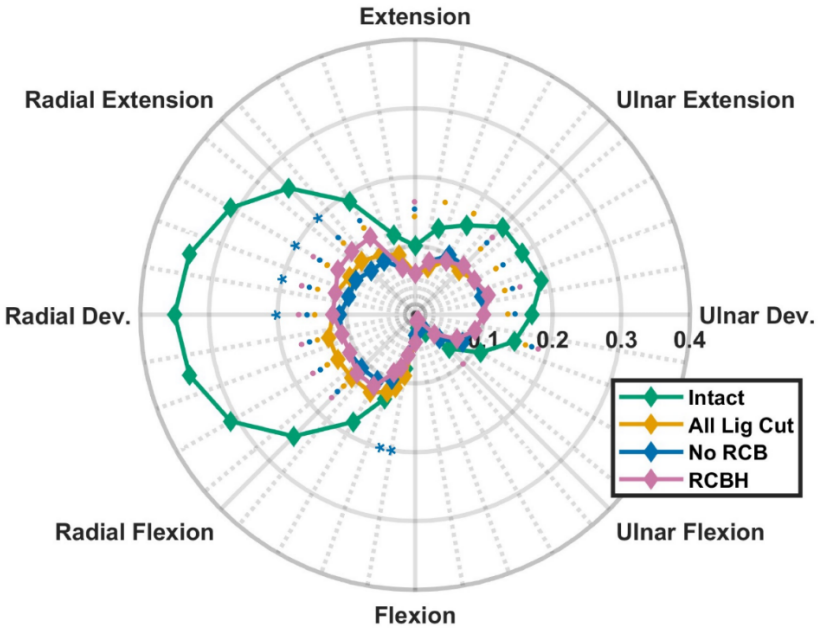

Figure 3.4. Average stiffness envelopes across the 28 motion directions for each condition: (A) intact, (B) all ligaments cut (ALC), (C) no radial carpal bone (RCB), and (D) small bone replacement with a radial carpal bone hemiarthroplasty (RCBH). Significant differences (p-values < 0.05) relative to intact are shown with a dot (•) and relative to ALC are shown with an asterisk (*).

Table 3.1. Estimated marginal mean final stiffness (Nm/°) (95% confidence interval) across the 28 motion directions for each condition: (A) intact, (B) all ligaments cut (ALC), (C) no radial carpal bone (RCB), and (D) small bone replacement with a radial carpal bone hemiarthroplasty (RCBH).

Direction	Condition			
	Intact	ALC	No RCB	RCBH
EX0	0.09 (0.03, 0.25)	0.09 (0.02, 0.36)	0.11 (0.03, 0.32)	0.09 (0.02, 0.30)
FE0	0.02 (0.00, 0.11)	0.02 (0.00, 0.15)	0.02 (0.00, 0.07)	0.02 (0.00, 0.07)
RD0	0.25 (0.11, 0.58)	3.05 (1.82, 5.11)*	0.62 (0.40, 0.98)*†	0.49 (0.13, 1.94)*
RE15	0.23 (0.09, 0.59)	0.88 (0.16, 4.90)*	0.48 (0.14, 1.59)*	0.30 (0.06, 1.40)
RE30	0.19 (0.07, 0.51)	0.44 (0.14, 1.35)*	0.79 (0.08, 8.28)	0.50 (0.07, 3.65)
RE45	0.15 (0.06, 0.37)	0.27 (0.08, 0.89)*	0.26 (0.05, 1.48)	0.27 (0.05, 1.57)
RE60	0.10 (0.05, 0.19)	0.17 (0.05, 0.58)	0.16 (0.03, 0.83)	0.12 (0.02, 058)
RE75	0.08 (0.03, 0.23)	0.07 (0.01, 0.41)	0.08 (0.02, 0.30)	0.08 (0.03, 0.20)
RF15	0.24 (0.10, 0.59)	1.31 (0.88, 1.93)*	0.54 (0.30, 0.99)†	0.58 (0.32, 1.06)*†
RF30	0.22 (0.09, 0.56)	0.65 (0.26, 1.62)*	0.73 (0.50, 1.08)	0.73 (0.33, 1.61)
RF45	0.19 (0.07, 0.48)	0.57 (0.12, 2.73)	0.39 (0.21, 0.74)	0.74 (0.26, 2.15)
RF60	0.14 (0.05, 0.39)	0.21 (0.09, 0.48)*	0.27 (0.10, 0.71)	0.53 (0.19, 1.44)
RF70	0.09 (0.03, 0.26)	0.16 (0.0.8, 0.33)*	0.29 (0.09, 0.89)	0.14 (0.02, 0.83)
RF75	0.07 (0.02, 0.23)	0.16 (0.10, 0.28)	0.21 (0.08, 0.59)	0.08 (0.02, 0.39)
RF80	0.05 (0.02, 0.18)	0.13 (0.06, 0.30)	0.07 (0.02, 0.31)	0.06 (0.02, 0.25)
UD0	0.14 (0.05, 0.35)	0.13 (0.03, 0.59)	0.21 (0.03, 1.47)	0.11 (0.02, 0.57)
UE15	0.16 (0.05, 0.49)	0.15 (0.03, 0.72)	0.28 (0.04, 2.14)	0.15 (0.03, 0.84)
UE30	0.16 (0.05, 0.53)	0.27 (0.04, 1.86)	0.50 (0.05, 5.16)	0.28 (0.04, 2.10)°

UE45	0.17 (0.06, 0.50)	0.24 (0.04, 1.40)	0.12 (0.02, 0.71)	0.24 (0.04, 1.41)
UE60	0.14 (0.05, 0.39)	0.19 (0.04, 0.93)	0.18 (0.02, 1.62)	0.17 (0.03, 0.93)
UE75	0.13 (0.04, 0.38)	0.12 (0.03, 0.46)	0.13 (0.03, 0.52)	0.12 (0.03, 0.47)
UF15	0.11 (0.04, 0.33)	0.10 (0.02, 0.42)	0.16 (0.02, 1.18)	0.09 (0.02, 0.49)
UF30	0.08 (0.03, 0.24)	0.09 (0.02, 0.49)	0.15 (0.02, 1.35)	0.09 (0.01, 0.66)
UF45	0.05 (0.02, 0.16)	0.04 (0.01, 0.20)	0.03 (0.01, 0.21)	0.03 (0.01, 0.21)
UF60	0.013 (0.006, 0.029)	0.01 (0.00, 0.03)	0.01 (0.00, 0.03)	0.01 (0.00, 0.05)
UF70	0.01 (0.004, 0.02)	0.01 (0.00, 0.02)	0.01 (0.00, 0.04)	0.01 (0.00, 0.03)
UF75	0.01 (0.00, 0.02)	0.01 (0.00, 0.02)	0.01 (0.00, 0.04)	0.01 (0.00, 0.03)
UF80	0.02 (0.00, 0.05)	0.014 (0.006, 0.032)	0.014 (0.008, 0.025)	0.02 (0.00, 0.10)

* $p<0.05$ to Intact
† $p<0.05$ to ALC
° $p<0.05$ to No RCB

For the PSROM protocol, neutral pronation and supination measured 21.2° (CI: 16.4, 27.4) and 12.6° (CI: 8.8, 17.8), respectively. Final stiffness decreased compared to intact to 0.13 Nm/° (CI: 0.11, 0.15; $p<0.05$) for pronation and 0.17 Nm/° (CI: 0.15, 0.20; $p<0.05$) for supination. At UF75 (max ROM), supination ROM increased by 9.5° to 28.9° (CI: 23.7, 35.1; $p<0.05$), whereas pronation measured 20.3° (CI: 13.5, 30.6) (**Figure 3.5**). Corresponding final stiffness values were 0.11 Nm/° (CI: 0.08, 0.14) for pronation and 0.14 Nm/° (CI: 0.13, 0.16) for supination.

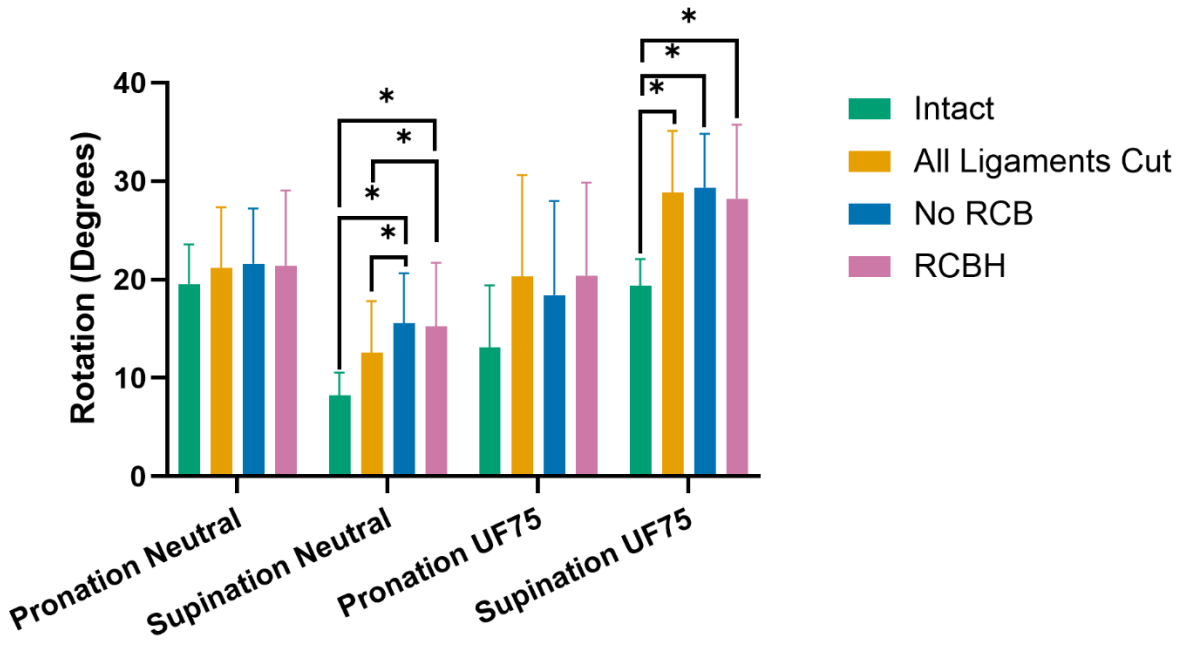

Figure 3.4. Pronation and supination at neutral and maximum range of motion (UF75) (average ± 95% confidence intervals) of the four testing conditions: intact, all ligaments cut (ALC), no radial carpal bone (RCB), and small bone replacement with a radial carpal bone hemiarthroplasty (RCBH). Significant differences (p-values < 0.05) are shown with an asterisk (*).

For the TROM protocol, volar translation (10.2 mm, CI: 8.6, 12.2) exceeded dorsal translation (5.4 mm, CI: 4.0, 7.2; $p<0.05$) (**Figure 3.6**). Volar stiffness (6.25 N/mm, CI: 4.35, 8.97) was lower ($p<0.05$) than both intact and dorsal stiffness (7.47 N/mm, CI: 5.38, 10.38).

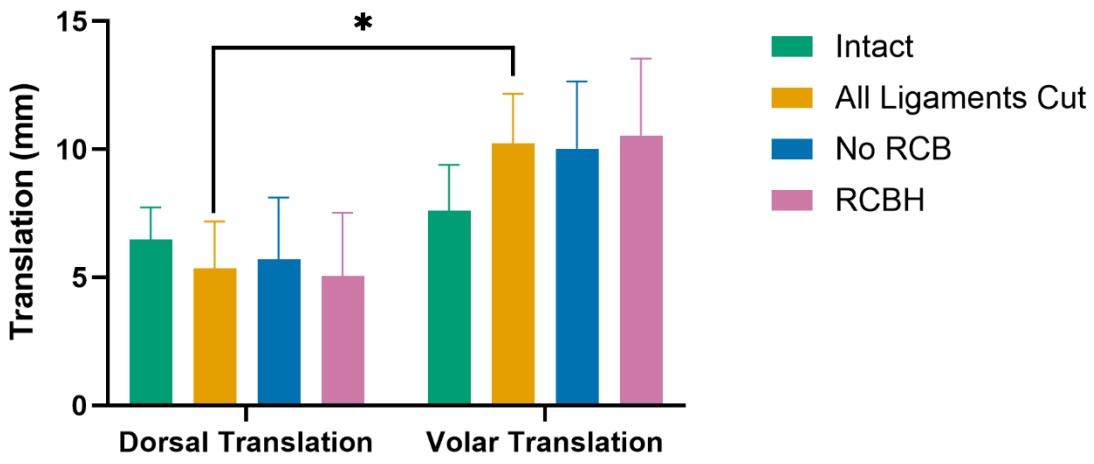

Figure 3.5. Average volar and dorsal translation ± 95% confidence intervals of the metacarpals relative to the radius and ulna for the four testing conditions: intact, all ligaments cut (ALC), no radial carpal bone (RCB), and radial carpal bone hemiarthroplasty (RCBH). Significant differences (p-values < 0.05) are shown with an asterisk (*).

3.4.2. No RCB Biomechanics

Removal of the RCB increased ROM in 19 directions relative to intact and in 12 directions relative to ALC. Among primary anatomical directions, ROM increased ($p<0.05$) compared to intact in extension (+7.4^0 to 16.8^0, CI: 13.5, 20.9) and radial deviation (+7.5^0 to 10.8^0, CI: 7.4, 15.7) (**Figure 3.3**); radial deviation also increased compared to ALC (+0.9^0; $p<0.05$). Average stiffness decreased in 14 directions relative to intact and in 6 directions relative to ALC. Among the primary anatomical directions, decreases were observed in extension (0.05 Nm/°, CI: 0.04, 0.07) and ulnar deviation (0.08 Nm/°, CI: 0.07, 0.11) relative to intact, and in radial deviation (0.10 Nm/°, CI: 0.08, 0.12) relative to both intact and ALC (**Figure 3.4**). Final stiffness increased in 2 directions relative to intact and decreased in 2 directions relative to ALC, including radial deviation (0.62 Nm/^{0}, CI: 0.40, 0.98; $p<0.05$) (**Table 3.1**).

In the PSROM protocol, neutral supination ROM increased ($p<0.05$) by 7.3^0 compared to intact and 3.0^0 compared to ALC to 15.5^0 (CI: 11.7, 20.6), while pronation measured 21.6^0 (CI: 17.2, 27.2). Stiffness decreased compared to intact for supination (-0.05 Nm/^{0} to 0.17 Nm/^{0}, CI: 0.16, 0.18; $p<0.05$) and pronation (-0.06 Nm/^{0} to 0.12 Nm/^{0}, CI: 0.11, 0.14; $p<0.05$). At UF75, supination ROM increased compared to intact by 10.0^0 to 29.4^0 (CI: 24.76, 34.81; $p<0.05$), while pronation measured 18.4^0 (CI: 12.1, 28.0) (**Figure 3.5**). Stiffness at UF75 was unchanged compared to ALC at 0.11 Nm/^{0} (CI: 0.09, 0.14) for pronation and 0.14 Nm/^{0} (CI: 0.11, 0.16) for supination.

In the TROM protocol, volar and dorsal translation measured 10.0 mm (CI: 7.9, 12.7) and 5.7 mm (CI: 4.0, 8.1), respectively (**Figure 3.6**). Volar stiffness (6.23 N/mm, CI: 4.51, 8.59) was lower than dorsal stiffness (7.32 N/mm, CI: 5.18, 10.33; $p<0.05$).

3.4.3. Radial Carpal Bone Hemiarthroplasty Biomechanics

Implantation of the RCBH in the YMP carpus increased ROM in 22 directions compared to intact and 1 direction compared to ALC. ROM did not differ compared to the no RCB condition. The greatest ROM occurred in the UF70 direction at 97.0^0 (CI: 73.1, 128.7). Among primary anatomical directions, ROM increased compared to intact in extension ($+9.0^0$ to 18.5^0, CI: 14.9, 22.8; $p<0.05$) and radial deviation ($+7.9^0$ to 11.2^0, CI: 7.6, 16.7; $p<0.05$) (**Figure 3.3**). ROM in the extension and radial deviation directions did not differ from the ALC and no RCB conditions. Average stiffness decreased ($p<0.05$) in 11 directions relative to intact, with no differences observed relative to ALC and no RCB (**Figure 3.4**). Among the

primary anatomical directions, decreases were observed in extension (0.06 Nm/°, CI: 0.04, 0.08) and radial deviation (0.12 Nm/°, CI: 0.08, 0.17) relative to intact. Final stiffness increased in 2 directions relative to intact, including radial deviation (0.49 Nm/°, CI: 0.13, 1.94; $p<0.05$), and in 1 direction relative to ALC and no RCB (**Table 3.1**).

In the PSROM protocol, neutral supination ROM increased by 7.0° compared to intact and 2.7° compared to ALC to 15.2° (CI: 10.66, 21.70; $p<0.05$), while pronation measured 21.4° (CI: 15.8, 29.1). Supination stiffness at neutral decreased by 0.03 Nm/° relative to intact but remained greater than pronation (0.14 Nm/°, CI: 0.13, 0.16; $p<0.05$). At UF75, supination ROM increased compared to intact by 8.8° to 28.2° (22.2, 35.8; $p<0.05$), while pronation measured 20.4° (CI: 13.95, 29.85) (**Figure 3.5**). Stiffness at UF75 was unchanged compared to ALC and no RCB at 0.14 Nm/° (CI: 0.10, 0.18) for supination and 0.11 Nm/° (CI: 0.09, 0.14) for pronation.

In the TROM protocol, volar translation measured 10.5 mm (CI: 8.2, 13.5) with a stiffness of 14.81 N/mm (CI: 7.22, 30.38), whereas dorsal translation measured 5.1 mm (CI: 3.4, 7.5) with a stiffness of 7.75 N/mm (CI: 5.46, 11.00) (**Figure 3.6**).

3.5. Discussion

The aim of this study was to quantify the YMP carpus biomechanics to assess its suitability as a preclinical model for the human wrist for evaluating osteoarthritis treatments, including carpal bone replacement. Based on prior findings that human wrist ROM increases following ligament transections,[23] we hypothesized that ROM would increase after transection of all ligaments connected

to the RCB, further increase after RCB resection, and return to intact levels following small bone replacement. Consistent with our hypothesis, ROM increased after ligament transection and RCB resection. However, ROM did not return to intact levels after RCBH implantation.

In vitro testing has been widely used to quantify carpal [24–29] and wrist [23] ROM, revealing progressive increases in motion and instability following ligament transection. Prior studies demonstrated increased carpal bone motion following ligament transection. Specifically, SLIL transection increased scaphoid flexion. Additional injury to volar and dorsal SLIL components or secondary stabilizers further increased scaphoid and lunate motion and overall instability.[27–29] For overall wrist motion, Badida et al. reported that isolated SLIL transection did not significantly affect ROM; however, subsequent DIC transection increased ROM by approximately 3.9° in radial deviation, 8.8° in radial extension, and 13° in ulnar flexion. Further transection of the long radiolunate ligament increased ROM across multiple directions.[23] YMP carpus ROM was previously reported by Altieri et al., who mimicked a ligament transection sequence involving the radial intermediate ligament, homologous to the scapholunate interosseous ligament and dorsal intercarpal ligament (DIC); however, only subtle increases in ROM were observed following transection of both ligaments (approximately 3° in extension).[19] Similarly, the YMP carpus demonstrated increased ROM following transection of all ligaments connected to the RCB, including 4.3° in radial flexion, 5.5° in radial extension, 10.3° in ulnar flexion, and 6.4° in ulnar extension.

Few studies have examined wrist biomechanics following removal of a single carpal bone, and existing findings report inconsistent effects on range of motion. However, Sobczak, et al. and Blankenhorn, et al. reported biomechanical outcomes in cadaveric wrists after proximal row carpectomy.[30,31] Blankenhorn, et al. observed substantial reductions in wrist motion, including decreases of 28% in flexion, 30% in extension, 40% in radial deviation, and 12% in ulnar deviation due to radiocarpal impingement, specifically the trapezoid on the radial styloid.[31] In contrast, Sobczak, et al. found no significant differences in ROM compared to intact and capsulotomy conditions, although reductions occurred across all degrees of freedom except palmar flexion.[30] In the YMP carpus, the opposite was observed in the no RCB condition, with ROM increases of approximately 79% in extension, 225% in radial deviation, and 71% ulnar deviation, while flexion decreased minimally (8%). This minimal reduction may reflect measurement limitations due to extreme flexion of the YMP carpus prior to fixture collision during testing. Although the magnitude of these changes differs from human studies, the overall ROM profile of the YMP carpus is comparable, exhibiting an elliptical motion envelope with limited extension.

To our knowledge, no studies have reported human wrist biomechanics following small bone replacement, although related implant procedures have shown variable effects on wrist ROM. However, implant effects on cadaveric wrist ROM have been evaluated in total wrist arthroplasty,[10,11,32] ulnar head arthroplasty,[33] and distal radioulnar joint prosthesis.[34] Following total wrist arthroplasty, Mookerjee et al. reported decreases in flexion, extension, and radial

deviation,[11] whereas Glanville et al. observed no significant differences in maximal flexion, extension, or radial ulnar deviation compared to preoperative values.[32] Studies of distal radioulnar joint prosthesis and ulnar head arthroplasty reported no significant changes in ROM [34] or kinematics,[33] respectively. In the present study, small bone replacement using an RCBH did not restore the YMP carpus to intact ROM; instead, slight increases in ROM were observed relative to the bone resection condition. These increases may reflect factors such as implant fixation, suboptimal implant sizing, or residual joint laxity following repeated testing.

Consistent with the observed changes in ROM, average and final stiffness exhibited contrasting trends across conditions Average stiffness decreased relative to intact in all three conditions, with the greatest values consistently observed in the radial flexion direction, consistent with patterns reported in intact human wrists.[21] In contrast, final stiffness, defined as the slope between 0.75 and 1 Nm, showed a substantial increase relative to intact in specific directions: radial deviation for ALC, radial extension for no RCB, and radial flexion for RCBH. This increase appears to result from minimal displacement occurring as the specimen approaches 1 Nm, likely due to interaction between the RCB and the radial styloid or other lateral stabilizing structures of the YMP carpus, producing an overshoot in load. A similar effect has been observed in spine in vitro testing, where low-stiffness regions (the neutral zone) can lead to large displacement changes with minimal load variation, requiring machine compensation and resulting in overshoot of load targets.[35]

Several limitations should be considered with this study. First, motion of the intact and implant RCBs were not quantified. We quantified overall wrist motion, defined as metacarpal motion relative to the radius and ulna, demonstrating increased ROM following ligament transection and bone resection. Assessing individual carpal kinematics could further support the translatability of the YMP by allowing comparison with human wrist kinematics. Second, all specimens underwent multiple freeze–thaw cycles (~3 cycles) and repeated sequential testing. While the effects of freeze–thaw cycling on animal specimens have not been well characterized, prior studies on human tendons report mixed results on the biomechanical effects of multiple freeze-thaw cycles. Huang, et al. investigated the effects of freeze-thaw cycles on human flexor tendons and found that repetitive freeze-thaw cycles (> 5) declines the structural, mechanical and viscoelastic properties of human tendons.[36] In contrast, Jung, et al. found that there was little effect on the structural properties of the bone-patellar tendon-bone grafts or the mechanical properties of the patellar tendon tissue following eight freeze-thaw cycles.[37] Thus, the impact of repeated freeze–thaw cycles on specimen biomechanics remains uncertain and should be considered when interpreting the results. Implant sizing may have been too small for the YMP carpus, potentially limiting their effect on restoring intact ROM. Although smaller implants are typically selected to avoid overpacking the joint and compromising stability,[38,39] under sizing may have limited articulation with surrounding bones, resulting in a ROM profile similar to the bone-resected condition. Additionally, implant fixation may have loosened during ROM testing, further compromising stability.

In summary, YMP carpus ROM increased compared to intact following ligament transection and subsequent RCB resection. Although small bone replacement was expected to restore intact ROM, only minimal increases were observed compared to the bone resection condition. The similar elliptical ROM envelopes of the YMP and human wrists with findings of increases in ROM, support the potential of the YMP as a preclinical model for the human wrist. Further studies evaluating implant designs and quantifying individual carpal kinematics are needed to strengthen the utility of the YMP for testing emerging osteoarthritis treatments.

3.6. Acknowledgments

The authors would like to acknowledge Landon Begin for his assistance with 3D printing the RCBH implants and preparing suture anchors for testing.

3.7. References

1. Adams BD, Kleinhenz BP, Guan JJ. Wrist Arthrodesis for Failed Total Wrist Arthroplasty. *J Hand Surg*. 2016;41(6):673-679. doi:10.1016/j.jhsa.2016.02.012
2. Rodriguez-Merchan EC, Tabeayo-Alvarez ED, Shojaie B, Kachooei AR. Total Wrist Arthrodesis: An Update on Indications, Technique and Outcomes. *Arch Bone Jt Surg*. 2023;11(3):144-153. doi:10.22038/ABJS.2022.65875.3154
3. Kay HF, Kang HP, Alluri R, Azad A, Ghiassi A. Proximal Row Carpectomy Versus 4-Corner Fusion: Incidence, Conversion to Fusion, and Cost. *J Hand Surg*. Published online February 20, 2020. doi:10.1016/j.jhsa.2019.12.010
4. Chim H, Moran SL. Long-Term Outcomes of Proximal Row Carpectomy: A Systematic Review of the Literature. *J Wrist Surg*. 2012;1(2):141-148. doi:10.1055/s-0032-1329547
5. Dacho AK, Baumeister S, Germann G, Sauerbier M. Comparison of proximal row carpectomy and midcarpal arthrodesis for the treatment of scaphoid nonunion advanced collapse (SNAC-wrist) and scapholunate advanced collapse (SLAC-wrist) in stage II. *J Plast Reconstr Aesthetic Surg JPRAS*. 2008;61(10):1210-1218. doi:10.1016/j.bjps.2007.08.007
6. Wagner ER, Srnec JJ, Fort MW, Barras LA, Rizzo M. Outcomes of Revision Total Wrist Arthroplasty. *J Am Acad Orthop Surg Glob Res Rev*. 2021;5(3). doi:10.5435/JAAOSGlobal-D-21-00035
7. Cavaliere CM, Chung KC. A systematic review of total wrist arthroplasty compared with total wrist arthrodesis for rheumatoid arthritis. *Plast Reconstr Surg*. 2008;122(3):813-825. doi:10.1097/PRS.0b013e318180ece3
8. Nair R. Review article: Total wrist arthroplasty. *J Orthop Surg Hong Kong*. 2014;22(3):399-405.
9. Carlson JR, Simmons BP. Total wrist arthroplasty. *J Am Acad Orthop Surg*. 1998;6(5):308-315.
10. Bain GI, Bellringer SF, Russo MP, Amin D, Costi JJ. Biomechanical analysis of cadaveric wrists before and after MOTEC wrist arthroplasty using a hexapod robot. *J Hand Surg Eur Vol*. Published online September 16, 2024:17531934241274135. doi:10.1177/17531934241274135
11. Mookerjee GG, Werner FW, Short WH. Tendon Force and Range of Motion Changes After In Vitro Total Wrist Replacement. *J Hand Surg*. Published online December 24, 2024:S0363-5023(24)00570-7. doi:10.1016/j.jhsa.2024.11.011
12. Gaspar MP, Lou J, Kane PM, Jacoby SM, Osterman AL, Culp RW. Complications Following Partial and Total Wrist Arthroplasty: A Single-Center Retrospective Review. *J Hand Surg*. 2016;41(1):47-53.e4. doi:10.1016/j.jhsa.2015.10.021
13. Vance MC, Packer G, Tan D, Crisco JJT, Wolfe SW. Midcarpal hemiarthroplasty for wrist arthritis: rationale and early results. *J Wrist Surg*. 2012;1(1):61-68. doi:10.1055/s-0032-1323644

14. Serra CI, Soler C. Animal Models of Osteoarthritis in Small Mammals. *Veterinary Clin North Am Exot Anim Pract*. 2019;22(2):211-221. doi:10.1016/j.cvex.2019.01.004
15. McCoy AM. Animal Models of Osteoarthritis: Comparisons and Key Considerations. *Vet Pathol*. 2015;52(5):803-818. doi:10.1177/0300985815588611
16. Longo UG, Papalia R, De Salvatore S, Picozzi R, Sarubbi A, Denaro V. Induced Models of Osteoarthritis in Animal Models: A Systematic Review. *Biology*. 2023;12(2):283. doi:10.3390/biology12020283
17. Pearce AI, Richards RG, Milz S, Schneider E, Pearce SG. Animal models for implant biomaterial research in bone: a review. *Eur Cell Mater*. 2007;13:1-10. doi:10.22203/ecm.v013a01
18. Behrends DA, Khendek L, Gao C, Zayed N, Henderson JE, Martineau PA. Characterization of a Pre-Clinical Mini-Pig Model of Scaphoid Non-Union. *J Funct Biomater*. 2015;6(2):407-421. doi:10.3390/jfb6020407
19. Altieri MK, Badida R, Vaughan QM, Molino J, Akelman E, Crisco JJ. Biomechanical evaluation of the porcine carpus as a potential preclinical animal model for the human carpus. *J Biomech*. 2024;177:112429. doi:10.1016/j.jbiomech.2024.112429
20. Stoeckl BD, Zlotnick HM, Farrell MJ, et al. The porcine accessory carpal bone as a model for biologic joint replacement for trapeziometacarpal osteoarthritis. *Acta Biomater*. 2021;129:159-168. doi:10.1016/j.actbio.2021.05.011
21. Badida R, Garcia-Lopez E, Sise C, Moore D, Crisco J. An Approach to Robotic Testing of the Wrist Using 3-D Imaging and a Hybrid Control Strategy. *J Biomech Eng*. 2020;142(6):064501. doi:10.1115/1.4046050
22. Vaughan QM, Morton AM, Moore D, Akelman E, Crisco JJ. Development of small bone implants using a mean shape bone in a porcine model for carpal bone replacement. *Proc Inst Mech Eng [H]*. Published online July 24, 2025:9544119251355382. doi:10.1177/09544119251355382
23. Badida R, Akhbari B, Vutescu E, Moore DC, Wolfe SW, Crisco JJ. The Role of Scapholunate Interosseous, Dorsal Intercarpal, and Radiolunate Ligaments in Wrist Biomechanics. *J Biomech*. 2021;125:110567. doi:10.1016/j.jbiomech.2021.110567
24. Figueroa J, Werner FW, Travers PM, Short WH. Carpal Motion in Chronic Geissler IV Scapholunate Interosseous Ligament Wrists. *J Hand Surg*. 2021;46(5):368-376. doi:10.1016/j.jhsa.2020.12.015
25. Fraysse F, Costi JJ, Stanley RM, et al. A novel method to replicate the kinematics of the carpus using a six degree-of-freedom robot. *J Biomech*. 2014;47(5):1091-1098. doi:10.1016/j.jbiomech.2013.12.033
26. Short WH, Werner FW, Sutton LG. Dynamic biomechanical evaluation of the dorsal intercarpal ligament repair for scapholunate instability. *J Hand Surg*. 2009;34(4):652-659. doi:10.1016/j.jhsa.2008.12.009
27. Short WH, Werner FW, Green JK, Sutton LG, Brutus JP. Biomechanical evaluation of the ligamentous stabilizers of the scaphoid and lunate: part III. *J Hand Surg*. 2007;32(3):297-309. doi:10.1016/j.jhsa.2006.10.024

28. Short WH, Werner FW, Fortino MD, Palmer AK, Mann KA. A dynamic biomechanical study of scapholunate ligament sectioning. *J Hand Surg*. 1995;20(6):986-999. doi:10.1016/S0363-5023(05)80147-9
29. Waters MS, Werner FW, Haddad SF, McGrattan ML, Short WH. Biomechanical Evaluation of Scaphoid and Lunate Kinematics Following Selective Sectioning of Portions of the Scapholunate Interosseous Ligament. *J Hand Surg*. 2016;41(2):208-213. doi:10.1016/j.jhsa.2015.11.009
30. Sobczak S, Rotsaert P, Vancabeke M, Van Sint Jan S, Salvia P, Feipel V. Effects of proximal row carpectomy on wrist biomechanics: a cadaveric study. *Clin Biomech*. 2011;26(7):718-724. doi:10.1016/j.clinbiomech.2011.03.002
31. Blankenhorn BD, Pfaeffle HJ, Tang P, Robertson D, Imbriglia J, Goitz RJ. Carpal kinematics after proximal row carpectomy. *J Hand Surg*. 2007;32(1):37-46. doi:10.1016/j.jhsa.2006.10.014
32. Glanville J, Bates KT, Silver N, Karthikappallil D, Fichera S, Brown DJ. Replication of Coupled Movements of the Wrist: A Cadaveric Study of Total Wrist Arthroplasty. *J Hand Surg*. 2025;50(4):424-432. doi:10.1016/j.jhsa.2024.12.006
33. Gordon KD, Dunning CE, Johnson JA, King GJW. Kinematics of ulnar head arthroplasty. *J Hand Surg*. 2003;28(6):551-558. doi:10.1016/s0266-7681(03)00150-5
34. Moradi A, Binava R, Hedjazi A, Eslami Hasanabadi S, Taher Chaharjouy N, Ebrahimzadeh MH. Biomechanical evaluation of intraosseous distal radioulnar joint prosthesis: A prosthesis designed based on Sauvé-Kapandji procedure. *Orthop Traumatol Surg Res OTSR*. 2021;107(5):102975. doi:10.1016/j.otsr.2021.102975
35. Bell KM, Hartman RA, Gilbertson LG, Kang JD. In Vitro Spine Testing Using a Robot-Based Testing System: Comparison of Displacement Control and "Hybrid Control." *J Biomech*. 2013;46(10):1663-1669. doi:10.1016/j.jbiomech.2013.04.007
36. Huang H, Zhang J, Sun K, Zhang X, Tian S. Effects of repetitive multiple freeze-thaw cycles on the biomechanical properties of human flexor digitorum superficialis and flexor pollicis longus tendons. *Clin Biomech*. 2011;26(4):419-423. doi:10.1016/j.clinbiomech.2010.12.006
37. Jung HJ, Vangipuram G, Fisher MB, et al. The effects of multiple freeze-thaw cycles on the biomechanical properties of the human bone-patellar tendon-bone allograft. *J Orthop Res Off Publ Orthop Res Soc*. 2011;29(8):1193-1198. doi:10.1002/jor.21373
38. Van Glabbeek F, Van Riet RP, Baumfeld JA, et al. Detrimental effects of overstuffing or understuffing with a radial head replacement in the medial collateral-ligament deficient elbow. *J Bone Joint Surg Am*. 2004;86(12):2629-2635. doi:10.2106/00004623-200412000-00007
39. Moon JG, Hong JH, Bither N, Shon WY. Can ulnar variance be used to detect overstuffing after radial head arthroplasty? *Clin Orthop*. 2014;472(2):727-731. doi:10.1007/s11999-013-3277-z

Chapter 4: Small Bone Replacement Leads to Greater Gait Asymmetry and Cartilage Damage Compared to Ligament Injury in a Porcine Wrist Model

Chapters 4 and 5 have been combined into the following manuscript.

Vaughan QM, Morton AM, Moore DC, Molino J, Akelman E, Crisco JJ. Small Bone Replacement Leads to Greater Gait Asymmetry, Cartilage Damage, and Osteophyte Formation Than Ligament injury in a Porcine Wrist Model. (UNDER REVIEW: *Osteoarthritis and Cartilage OPEN)*

4.1. Abstract

This study evaluated the Yucatan minipig (YMP) as a translational large-animal model of wrist osteoarthritis (OA) following ligament injury (LI) or small bone replacement (SBR) in a 12-week *in vivo* study. Eight YMPs were assigned to LI or SBR groups (n=4/group). Gait data were collected preoperatively and at 3, 6, 9, and 12 weeks postoperatively. Ratios of surgical to contralateral limbs were calculated for maximum force, impulse, stance time, and stride velocity and compared within and between experimental groups. At study completion, cartilage health was assessed histologically using OARSI scoring. We found that the SBR group demonstrated significant gait asymmetry at week 3, with reduced maximum force, impulse, and stance time relative to preop ($p < 0.05$), followed by partial recovery after 3 weeks postop. Compared to the LI group, the SBR group exhibited greater gait asymmetry ($p<0.05$) at all postoperative timepoints, while stride velocity remained unchanged. Histological analysis revealed significantly higher total OARSI scores in SBR experimental limbs compared to contralateral limbs across the distal radius and proximal carpal bones articular surfaces. The SBR group exhibited greater cartilage degeneration than the LI group ($p<0.05$), whereas contralateral limbs did not differ between groups. These findings support the YMP as a promising translational model of the human wrist for evaluating OA development following ligament injury and small bone replacement. Improved understanding of OA progression and therapeutic effects in this model may facilitate the development of targeted treatment strategies for wrist pathologies including arthroplasties.

4.2. Introduction

The human wrist is a complex joint comprised of multiple bones and ligaments that function collectively to facilitate complex motions while providing stability. Wrist ligaments are classified as primary or secondary stabilizers, with the scapholunate interosseous ligament (SLIL) serving as a key primary stabilizer between the scaphoid and lunate bones.[1,2] Injury to the SLIL is the most common ligamentous injury and when combined with disruption of secondary stabilizers such as the dorsal intercarpal ligament (DIC), can result in wrist instability, altered biomechanics.[2–5] These injuries can be associated with pain during tasks that include pushing, gripping, or grasping and progression to degenerative joint disease, including as osteoarthritis (OA).[3]

Current treatment strategies for wrist OA focus on symptom management during the early stages of disease and often progress to surgical intervention in advanced cases.[6] Treatment options include wrist fusion (arthrodesis),[7,8] proximal row carpectomy,[9–11] and total wrist replacement (arthroplasty).[12–15] Although these treatments aim to alleviate pain and restore function,[16–18] long-term outcomes are limited by complications such as hardware failure,[8] decreased grip strength,[10,11] and component loosening.[13–15,19] Other treatment options include wrist hemiarthroplasties, specifically carpal bone replacements, which offer a potential motion-preserving alternative to fusion or arthroplasty with minimal hardware implantation and bone resection.[20,21] Carpal bone replacements have been found to reduce pain and improve function relative to preoperative results.[22–24] However, long term follow-up has reported mild progression of OA and the development of

osteolysis.[25–27] Despite these findings, carpal bone replacements remain a viable alternative to more aggressive procedures, given favorable patient-reported outcomes and the ability to pursue revision or salvage procedures if failure occurs. To further optimize carpal bone replacement treatments, a clearer understanding of OA development following implantation is necessary.

OA progression is typically evaluated and diagnosed through clinical examination and radiographic imaging.[28] The presence of osteophytes, which are bony outgrowths that often form at joint margins, is a common indicator of disease.[29,30] As OA advances, joint space narrowing becomes evident on radiographs, and in severe cases, subchondral cysts and bone deformities may also appear.[31] However, OA is often diagnosed at a stage when irreversible joint damage has already occurred, limiting the effectiveness of available treatments.[32] Given this challenge, animal models serve as essential tools for studying disease progression, evaluating novel treatment strategies, and assessing the impact of interventions at various stages of OA development.

Animal models have been widely used to study OA progression in large joints, particularly the knee, using chemical, mechanical, or surgical induction methods.[33,34] Small animals such as mice, rats, guinea pigs, and rabbits are commonly used due to their rapid disease progression, lower cost, and ease of housing.[35,36] In contrast, larger animals like sheep and pigs are often preferred for their anatomical and biomechanical similarities to humans.[33,36,37] Surgical models of OA have most frequently targeted the stifle joint, homologous to the knee, as models for medial meniscal tear replication,[38] partial,[38] or total meniscectomy,[39,40] and anterior cruciate ligament (ACL) transection.[40–44] Despite the extensive use of

these models to study OA in large joints, there is a lack of studies focused on OA progression or improvement of treatment options in the wrist.

Assessment of both healthy and OA affected joints is essential for understanding disease progression and evaluating treatment options. Gait analysis is widely used in animal models of OA to quantify alterations under baseline, injury, and treatment conditions. Metrics such as limb idleness, maximum force ratios, stance time, stride velocity, and related gait parameters have demonstrated the capability of detecting OA-related changes in experimental, treated, and contralateral joints.[44–50] Structural severity is further validated through histopathological evaluation of cartilage degeneration.[44,45,47–49,51] Although gait and histopathological analysis are well established for evaluating OA progression in animal models, most studies have focused on stifle joint injuries. There remains a need for a translational large animal model of post-traumatic OA following ligament injury and small bone replacement in the carpus. To address this gap, we identified the Yucatan minipig (YMP) as a promising preclinical animal model for the human wrist due to its similarities in anatomy, size, and bone composition.[37]

This study evaluated the Yucatan minipig as a preclinical animal model for assessing osteoarthritis (OA) progression following either ligament injury (LI) or small bone replacement (SBR) in the carpus. OA progression was monitored through changes in gait over a 12-week *in vivo* study. Based on previous clinical reports of OA development following ligament injury,[52–54] we hypothesized that the ligament injury group would exhibit increased gait asymmetry and more severe histological degeneration of cartilage than animals receiving a small bone replacement at 12 weeks.

4.3. Methods

4.3.1. Animal Acquisition

Following IACUC review and approval, eight Yucatan minipigs (YMP) were acquired from accredited laboratory animal suppliers (Sinclair Bio-Resources, Windham, ME and Premier BioSource, Ramona, CA). The cohort included four females and four males, ranging in age from 24.4 to 29.8 months (mean: 25.7 ± 1.8 months) and weight from 56.9 to 101.2 kg (mean: 84.2 ± 13.6 kg). The animals were assigned to undergo ligament injury alone (LI; 2M/2F) or small bone replacement (SBR; 2M/2F).

4.3.2. Surgical Procedure

Both the LI and SBR surgeries were performed on the right forelimb. Exposure was via a ~3 cm capsular incision over the medial aspect of the dorsal carpus, centered on the proximal row. A second incision (~5 cm) was made on the medial aspect of the volar carpus to access the Deep Radial Carpal Flexor Tendon (DRCFT), which was transected at the musculotendinous junction.

For each animal in the LI group, the deep and superficial attachments of the RIL and DIC were transected between the radial carpal and intermediate carpal bones (**Figure 4.1**). Once the ligaments were cut, the joint capsule, fascia, and skin were closed. For each animal in the SBR group, the radial carpal bone (RCB) was removed and replaced with a comparably sized cobalt-chrome (CoCr) implant.[55] The implant was fixed via a suture anchor (AR-1318FT, Arthrex, Inc., Naples, FL) placed into the medial side of the intermediate carpal bone (ICB), and suturing of the DRCFT to the dorsal ICB after passage through a dorsal-volar hole in the

implant. As with the LI animals, once the implant was fixed in place, the joint capsule, fascia, and skin were closed. All animals were allowed unrestricted weightbearing after surgery prior to euthanasia at week 12.

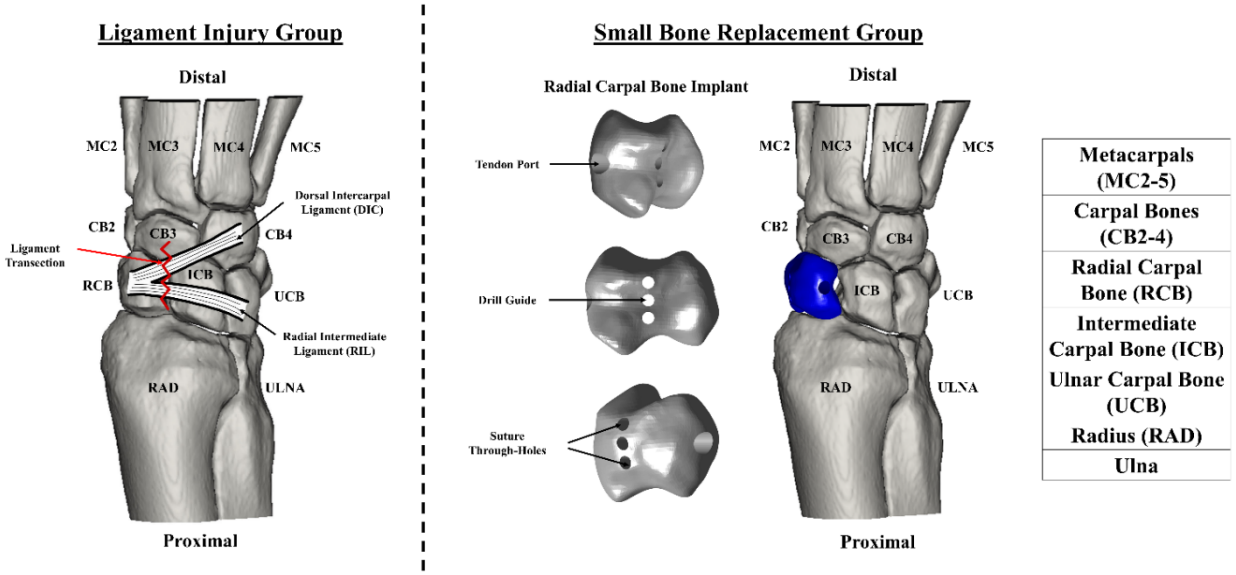

Figure 4.1. Bone models (dorsal view) of the YMP carpus depicting the ligament injury (LI) and small bone replacement (SBR) experimental groups. The YMP carpus consists of four metacarpals, two distinct rows of carpal bones, the radius and ulna. The ligament injury group (left) is a transection of the radial intermediate ligament (RIL) and dorsal intercarpal ligament (DIC), identified as homologous to the stabilizing ligaments of the human wrist. The small bone replacement group (right) shows the replacement of the radial carpal bone (RCB), homologous to the scaphoid, with a small bone implant (blue). The implant design includes a tendon port, drill guide, and suture through-holes.

4.3.3. Gait Measurement

Forelimb gait was evaluated using a digital pressure mat (HRV6 Walkway System; Tekscan Inc.), with video recorded contemporaneously to verify hoof strikes. Gait measurements were made prior to surgery (pre-op) and at 3, 6, 9, and 12 weeks post-operatively. Commercial software (Walkway 7.0; Tekscan Inc) was used for calibration, data collection, and analysis. A minimum of five successful trials were recorded per animal at each timepoint. Trial success was defined as the

animal walking continuously across the mat without stopping or stepping off. Hoof strikes were visualized in the software and labeled automatically (LF- left forelimb; RF- right forelimb; LH- left hindlimb; RH- right hindlimb). The raw gait data were reduced to yield maximum force (kg) and impulse (kg-s) for each hoof strike, each normalized as a percentage of body weight, as well as stance time (sec) and stride velocity (cm/sec). For each gait metric, the ratio of the operated forelimb to contralateral forelimb was calculated and averaged across trials for each animal.

4.3.4. Microscopic Articular Cartilage Analysis

Microscopic analysis of RCB articulations was performed on sagittal sections cut through the radial side of the carpus, and frontal sections cut through the middle of the remaining ulnar side (**Figure 4.2**). To do so, each wrist was grossly cut to yield a radial block, obtained by making a sagittal cut at the midpoint of the radial-ulnar width of the RCB, and dorsal and volar blocks obtained by making a frontal cut at the midpoint of the volar-dorsal depth of the RCB from the remaining ulnar portion of the wrist. After gross sectioning, the radial and dorsal blocks were decalcified, embedded in paraffin, sectioned, and stained with Safranin-O (Saf-O) and fast green. The cartilage surfaces at the articulations of the RCB and radius and the RCB and CB2/CB3 (**Figure 4.2**) were scored by the consensus of 3 reviewers (Q.M.V., D.C.M., and B.C.F.), following the OARSI guidelines for sheep and goat.[53] OARSI scores for each category (structure, chondrocyte density, cell cloning, interterritorial Saf-O, and tidemark) were summed and averaged across the radial and dorsal blocks for both operated and contralateral wrists and compared within and between experimental groups (LI and SBR).

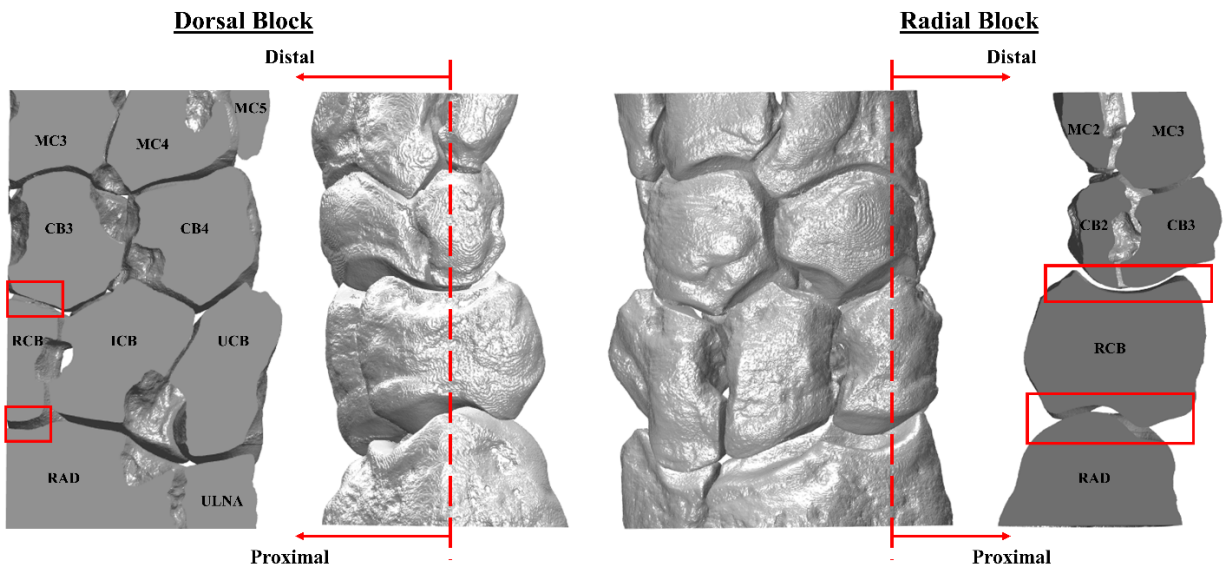

Figure 4.2. Bone models of the YMP carpus and the sectioning planes used for histopathological analysis. The carpus was divided into a dorsal block (left) and a radial block (right) with dashed lines indicating the planes of section. Red boxes denote the articular surfaces scored for histology for each experimental group (Figure 4.4). For the ligament injury group, scored surfaces included the distal radius, proximal and distal RCB, and proximal CB2/CB3. For the small bone replacement group, scored surfaces included the distal radius and proximal CB2/CB3.

4.3.5. Statistical Analysis

Descriptive statistics (mean and confidence intervals) were computed for gait ratios at each time point in the ligament injury and small bone replacement groups, and the results were compared. Data was imported into commercial software (SAS version 9.4, SAS Institute Inc, Cary, NC) for hypothesis testing. Generalized estimating equations (GEE) with fixed effects for experimental group (ligament injury vs small bone replacement), timepoint (preop, WK3, WK6, WK9, WK12), and the interaction between experimental group and timepoint were used to test whether gait metrics differed between the ligament injury and small bone replacement groups. GEEs were chosen as the analytic methods since it allows the

appropriate handling of repeated measurements and maximizes the information from animals with missing values. Classical sandwich estimation was used to protect against possible model misspecification. For microscopic cartilage analysis, mixed models with a binomial distribution and logit link function, a Laplace approximation, and random intercept per specimen were estimated to test if OARSI scores differed between experimental and contralateral limb within and across each experimental (ligament injury vs small bone replacement) group. Mixed effects were chosen as the analytic method as they allow the appropriate handling of repeated measures data and maximize the information from specimens with missing observations. Model residuals were examined to ensure that all model assumptions were satisfied. Post hoc comparisons were conducted within the models via orthogonal contrasts. The Holm test was used to adjust for multiple comparisons, maintaining a two-tailed familywise alpha of 0.05. A p-value < 0.05 was used to determine statistical significance.

4.4. Results

All animals in the LI and SBR groups completed the 12-week postoperative period without major complications. Mild carpal swelling was observed for an average of 4 days postoperatively in the operated limb. One animal exhibited implant subluxation, confirmed by radiography, in the post-op recovery period; the implant was repositioned via manual manipulation, and proper placement was confirmed radiographically. One animal experienced wound dehiscence one day postoperatively; the sutures were repaired under sedation without implant

subluxation. In the SBR group, implant placement was confirmed by radiography immediately after surgery and at 6 and 12 weeks postoperatively.

4.4.1. Gait Analysis

Gait analysis revealed that the SBR animals reduced weightbearing on their operated forelimbs 3 weeks postoperatively, with gradual return to near normal by week 9. Weight bearing was not altered in the LI animals at any time point. Specifically, at 3 weeks post-op the maximum force borne by the operated limb in the SBR animals decreased by 31.4% to a ratio of 0.72 compared to pre-op values (CI: 0.65-0.78; $p<0.001$) (**Figure 4.3A**), impulse decreased by 43.9% to 0.60 (CI: 0.52-0.68; $p<0.001$) (**Figure 4.3B**), and stance time decreased by 13.9% to 0.87 (CI: 0.84-0.90; $p<0.0001$) (**Figure 4.3C**). The asymmetry in maximum force and impulse decreased substantially after post-op week 3 but persisted at a low level when compared to pre-op throughout the study in the SBR group. At 6 weeks postoperative, impulse and stance time were less than pre-op by 21.5% (ratio: 0.84, CI: 0.80-0.89; $p<0.0001$) and 8.9% (ratio: 0.92, CI:0.90-0.95; $p<0.0001$), respectively. At weeks 9 and 12, impulse remained less by 14.0% (ratio: 0.92, CI: 0.88-0.96; $p<0.0001$) and 15.9% (ratio: 0.90, CI:0.81-0.98; $p=0.008$), respectively. Stride velocity in the SBR group did not differ from pre-op values at any time point.

Comparison of the gait asymmetries between the experimental groups revealed that the maximum force born by the operated limb in the SBR group was less than the LI group, by 31.4% at week 3 ($p<0.0001$), 8.5% at week 6 ($p=0.0049$), and 7.4% at week 9 ($p=0.01$) (**Figure 4.3A**). For impulse, the SBR group was less than LI group at all timepoints: by 42.3% at week 3 ($p<0.0001$), 22.9% at week 6

(p<0.0001), 13.2% at week 9 (p=0.0002), and 17.4% at week 12 (p=0.0006) (**Figure 4.3B**). Stance time was less in SBR group by 11.2% at week 3 (p<0.0001), 10.7% at week 6 (p<0.0001), and 7.8% at week 12 (p=0.001) (**Figure 4.3C**). There were no differences in stride velocity between groups at any timepoint (**Figure 4.3D**).

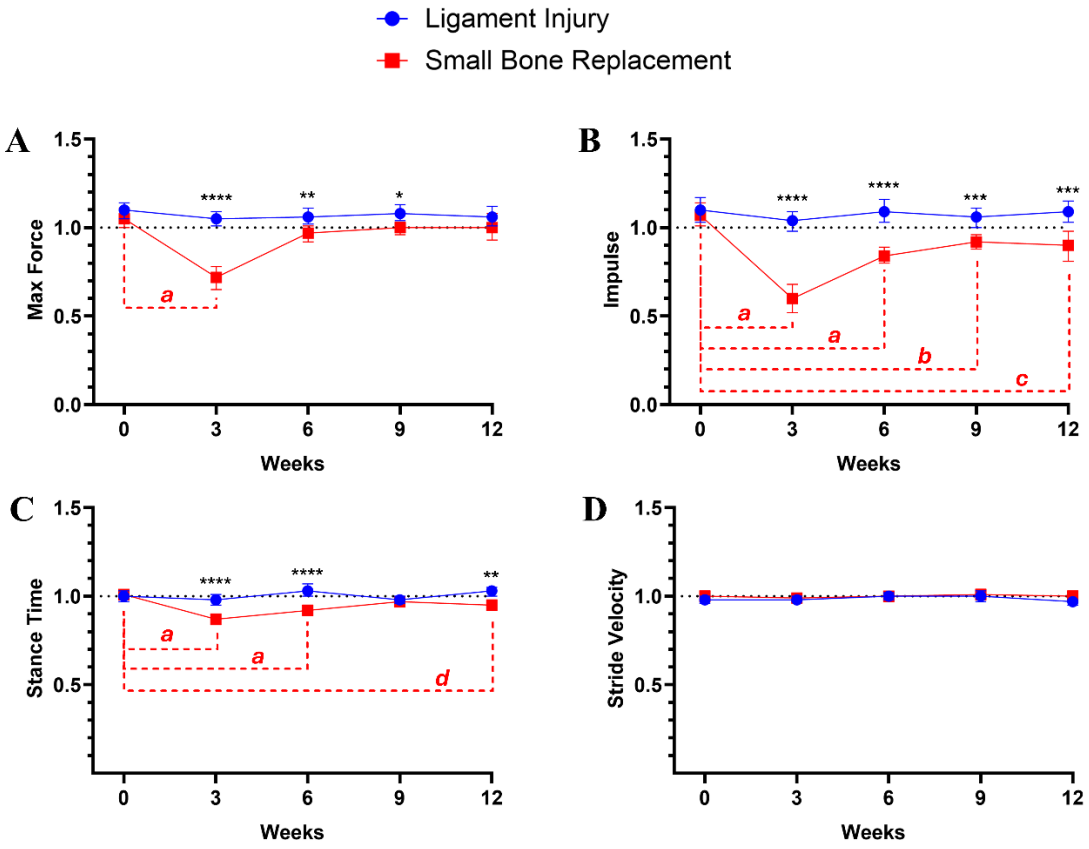

Figure 4.3. Mean gait ratios (surgical/contralateral) ± 95% confidence intervals over the 12-week study for the ligament injury (blue) and small bone replacement (red) groups for (A) max force, (B) impulse, (C) stance time, (D) stride velocity. Significant differences within the small bone replacement group at each timepoint compared to preoperative are indicated by letters (*a* = p ≤ 0.0001; *b* = p ≤ 0.001; *c* = p ≤ 0.01; *d* = p ≤ 0.05). Significant differences between the ligament injury (LI) and small bone replacement (SBR) groups at each timepoint are indicated by asterisks (* = p ≤ 0.05; ** = p ≤ 0.01; *** = p ≤ 0.001; **** = p ≤ 0.0001).

4.4.2. Microscopic Articular Cartilage Scoring

OARSI scores were largely driven by structural changes, particularly cartilage erosion, reduced chondrocyte density, and decreased Saf-O staining (**Figure 4.4**). The operated limb of the SBR group exhibited greater cartilage damage than the contralateral limb. For the distal radius articular surface, the total OARSI score was four times higher in the operated limb (24.0; CI: 19.0, 24.9) compared to the contralateral limb (7.1; CI: 3.4, 12.5; p= 0.006). For the proximal CB2/CB3 articular surface, the operated limb also demonstrated higher OARSI scores (24.0; CI: 18.1, 24.9) compared to the contralateral limb (5.3; CI: 3.5, 7.6; p= 0.008) (**Figure 4.5**).

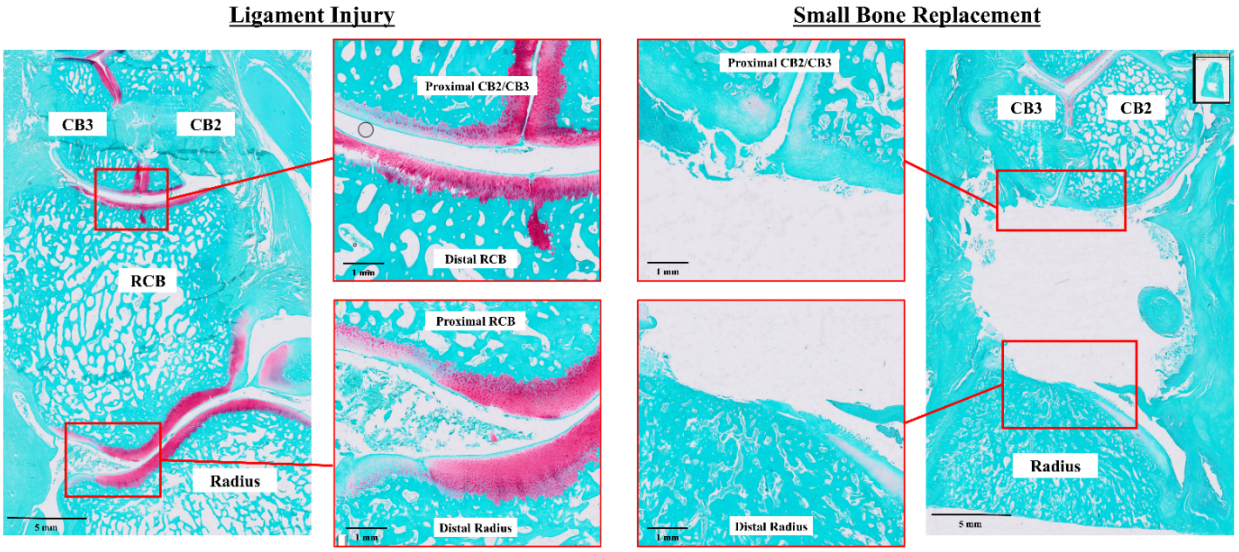

Figure 4.4. Safranin-O/Fast Green staining of representative right carpal sections from the ligament injury (left) and small bone replacement (right) groups. The small bone replacement group demonstrated severe cartilage degeneration of the distal radius and proximal CB2/CB3, characterized by structural erosion, decreased chondrocyte density, and loss of Safranin-O staining. In contrast, the ligament injury group exhibited minimal structural disruption with mild reduction in Safranin-O staining.

Total OARSI scores were missing for the contralateral limb of one animal in the LI group for the proximal and distal RCB and proximal CB2/CB3 articular surfaces, as the relevant bones were missing from the histological slice. No differences were observed between operated and contralateral limbs for any articular surface in the LI group. Mean OARSI scores for the operated limb were 6.8 (CI: 2.7, 13.5) for the distal radius, 8.3 (CI: 4.8, 12.7) for the proximal CB2/CB3, 6.1 (CI: 4.0, 8.9) for the distal RCB, and 5.4 (CI: 3.4, 8.1) for the proximal RCB, compared with 6.5 (CI: 3.6, 10.4), 5.3 (CI: 4.0, 6.7), 4.1 (CI: 1.7, 8.7), and 3.8 (CI: 1.8, 7.1), respectively, for the contralateral limb (**Figure 4.5**).

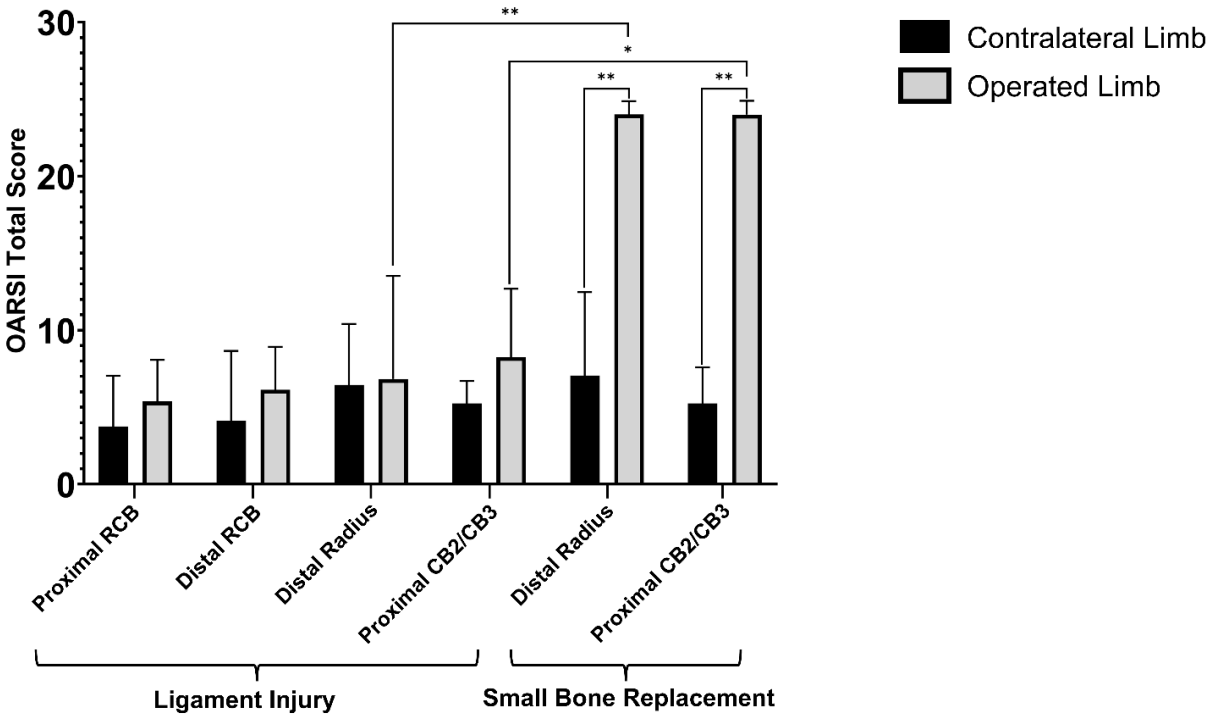

Figure 4.5. Mean total OARSI scores ± 95% confidence intervals for the articular surfaces scored in the ligament injury and small bone replacement groups. Results are displayed for contralateral (black) and operated (grey) limbs. Significant differences are indicated by asterisks (* = $p \leq 0.05$; ** = $p \leq 0.01$).

4.5. Discussion

The aim of this study was to evaluate the YMP as a preclinical animal model for assessing OA progression in the carpus following ligament injury and small bone replacement using gait and histopathological analysis. We hypothesized that the LI group would exhibit greater gait asymmetry than the SBR group, except at the first postoperative gait analysis (week 3), due to transection of homologous ligaments to two key stabilizers of the human wrist that cause instability after injury. We further hypothesized that gait asymmetry would correspond with histological evidence of OA at the conclusion of the 12-week study. On the contrary, the LI group did not demonstrate significant gait alterations following transection of the RIL and DIC, suggesting that the modeled injury may not have been sufficient to induce OA within the study period. This was supported by the absence of differences in total OARSI cartilage scores between experimental and contralateral limbs. In contrast, the SBR group exhibited greater gait asymmetry than the LI group, particularly in maximum force, impulse, and stance time. Although partial recovery occurred over time, gait symmetry did not return to preoperative levels. Histological analysis confirmed severe cartilage degeneration in the SBR group, with total OARSI scores averaging four times higher in the experimental limb compared to the contralateral limb.

Gait analysis using pressure mat systems is an established method for detecting OA-related functional changes in animal models that most commonly report offloading of the affected limb.[44,49,50,57] LaVallee et al. observed no gait differences following monosodium iodoacetate-induced knee OA over 12 weeks,[57] whereas

Karamchedu et al. reported greater hindlimb asymmetry at 4 weeks in a treatment group for ACL repair with a tissue-engineered implant compared to ACL transection.[44] Consistent with Karamchedu et al., SBR animals exhibited early and persistent gait asymmetry at 3 weeks postoperatively, whereas LI animals showed minimal functional change, similar to the limited gait alterations reported by Karamchedu et al. after ACL transection at 12 weeks postoperatively, which remained unchanged through 52 weeks in their study.[44]

Histopathological findings in the SBR group align with prior OA models demonstrating elevated OARSI scores following joint destabilization or reconstruction. Zhao et al. demonstrated higher scores after ACL reconstruction in a porcine model.[49] In contrast, Karamchedu et al. found no significant differences in OARSI scores between ACL transection, ACL reconstruction, and ACL repair with a tissue-engineered implant.[44] Although outcomes vary by species and injury model, the cartilage degeneration characterized by high OARSI scores in the SBR operated limbs demonstrate that the YMP carpus can develop moderate-to-severe OA cartilage pathology.

Several limitations warrant consideration. The YMP is a quadruped; however, approximately 60% of body weight is placed on the forelimbs,[58] representing a high-loading or worst-case condition relative to humans. Although gait analysis trends were comparable to those reported in animal models of knee OA,[44,57] preoperative measurements did not demonstrate perfect symmetry (surgical/contralateral = 1; equal distribution on the surgical and contralateral limbs). This asymmetry may be attributable to the clockwise direction of ambulation across the pressure mat, as animals enter the mat while navigating a

turn, potentially influencing forelimb loading relative to head orientation. The study duration also represents a limitation. While cartilage degeneration was evident at the conclusion of the 12-week study in the small bone replacement group, this time frame may have been insufficient for OA to develop following ligament injury. A longer follow-up period or a more extensive ligament transection protocol may be necessary to induce sufficient carpal instability to promote OA progression. The small sample size limited the ability to explore comparisons such as potential sex-based differences. Nevertheless, the model could detect significant differences in gait and histopathological outcomes. Cartilage degeneration in the YMP was evaluated following implantation of a small bone replacement fabricated only of CoCr. CoCr is an FDA-approved material that has been widely used in orthopedic implants because of its biocompatibility, wear resistance, and mechanical strength. However, evaluation of additional implant materials will be necessary to determine how the model responds to other bearing surfaces for articulation with cartilage in hemiarthroplasty treatment strategies for wrist OA.

In summary, RIL and DIC ligament transection did not induce significant OA within 12 weeks in the YMP carpus, whereas RCB replacement with cobalt chrome implants resulted in persistent gait asymmetry and marked cartilage degeneration. The functional and structural changes observed in the SBR group support the feasibility and translational potential of the YMP as a preclinical model for wrist OA. Longer follow-up periods, additional animals, refined instability models, and evaluation of different implant materials will further clarify the potential of the YMPs carpus for modeling human wrist pathologies and treatments.

4.6. Acknowledgments

We sincerely thank our team members, Scott Mc Allister, Anushka Jerez, Allison D'Amario, Dr. Anne Merley, Dr. Susanna Kurnick, Veronica Bouvier, and Ann Beauregard-Young for assisting with animal acquisition, surgical procedures, and animal care. We also thank Peter Caradonna and his team for their histology work, as well as Braden Fleming for assistance with histological scoring.

4.7. References

1. Short WH, Werner FW, Green JK, Masaoka S. Biomechanical evaluation of ligamentous stabilizers of the scaphoid and lunate. *J Hand Surg*. 2002;27(6):991-1002. doi:10.1053/jhsu.2002.35878
2. Rajan PV, Day CS. Scapholunate Interosseous Ligament Anatomy and Biomechanics. *J Hand Surg*. 2015;40(8):1692-1702. doi:10.1016/j.jhsa.2015.03.032
3. Wessel LE, Wolfe SW. Scapholunate Instability: Diagnosis and Management - Anatomy, Kinematics, and Clinical Assessment - Part I. *J Hand Surg*. Published online July 14, 2023:S0363-5023(23)00284-8. doi:10.1016/j.jhsa.2023.05.013
4. Badida R, Akhbari B, Vutescu E, Moore DC, Wolfe SW, Crisco JJ. The Role of Scapholunate Interosseous, Dorsal Intercarpal, and Radiolunate Ligaments in Wrist Biomechanics. *J Biomech*. 2021;125:110567. doi:10.1016/j.jbiomech.2021.110567
5. Kitay A, Wolfe SW. Scapholunate instability: current concepts in diagnosis and management. *J Hand Surg*. 2012;37(10):2175-2196. doi:10.1016/j.jhsa.2012.07.035
6. Drummer D, McAdam J, Seay R, et al. Osteoarthritis Progression: Mitigation and Rehabilitation Strategies. *Front Rehabil Sci*. 2021;2:724052. doi:10.3389/fresc.2021.724052
7. Adams BD, Kleinhenz BP, Guan JJ. Wrist Arthrodesis for Failed Total Wrist Arthroplasty. *J Hand Surg*. 2016;41(6):673-679. doi:10.1016/j.jhsa.2016.02.012
8. Rodriguez-Merchan EC, Tabeayo-Alvarez ED, Shojaie B, Kachooei AR. Total Wrist Arthrodesis: An Update on Indications, Technique and Outcomes. *Arch Bone Jt Surg*. 2023;11(3):144-153. doi:10.22038/ABJS.2022.65875.3154
9. Kay HF, Kang HP, Alluri R, Azad A, Ghiassi A. Proximal Row Carpectomy Versus 4-Corner Fusion: Incidence, Conversion to Fusion, and Cost. *J Hand Surg*. Published online February 20, 2020. doi:10.1016/j.jhsa.2019.12.010
10. Chim H, Moran SL. Long-Term Outcomes of Proximal Row Carpectomy: A Systematic Review of the Literature. *J Wrist Surg*. 2012;1(2):141-148. doi:10.1055/s-0032-1329547
11. Dacho AK, Baumeister S, Germann G, Sauerbier M. Comparison of proximal row carpectomy and midcarpal arthrodesis for the treatment of scaphoid nonunion advanced collapse (SNAC-wrist) and scapholunate advanced collapse (SLAC-wrist) in stage II. *J Plast Reconstr Aesthetic Surg JPRAS*. 2008;61(10):1210-1218. doi:10.1016/j.bjps.2007.08.007
12. Wagner ER, Srnec JJ, Fort MW, Barras LA, Rizzo M. Outcomes of Revision Total Wrist Arthroplasty. *J Am Acad Orthop Surg Glob Res Rev*. 2021;5(3). doi:10.5435/JAAOSGlobal-D-21-00035
13. Cavaliere CM, Chung KC. A systematic review of total wrist arthroplasty compared with total wrist arthrodesis for rheumatoid arthritis. *Plast Reconstr Surg*. 2008;122(3):813-825. doi:10.1097/PRS.0b013e318180ece3

14. Nair R. Review article: Total wrist arthroplasty. *J Orthop Surg Hong Kong*. 2014;22(3):399-405.
15. Carlson JR, Simmons BP. Total wrist arthroplasty. *J Am Acad Orthop Surg*. 1998;6(5):308-315.
16. Carlson Strother CR, Moran SL, Rizzo M. Small Joint Arthroplasty of the Hand: An Update on Indications, Outcomes, and Complications. *J Am Acad Orthop Surg*. 2023;31(15):793-801. doi:10.5435/JAAOS-D-23-00034
17. Joyce TJ, Unsworth A. A literature review of "failures" of the Swanson finger prosthesis in the metacarpophalangeal joint. *Hand Surg Int J Devoted Hand Up Limb Surg Relat Res J Asia-Pac Fed Soc Surg Hand*. 2002;7(1):139-146. doi:10.1142/s0218810402000881
18. Swanson AB, Swanson GG, Maupin BK, Hynes DE, Jindal P. Failed carpal bone arthroplasty: causes and treatment. *J Hand Surg*. 1989;14(2 Pt 2):417-424. doi:10.1016/0363-5023(89)90128-7
19. Krukhaug Y, Lie SA, Havelin LI, Furnes O, Hove LM. Results of 189 wrist replacements. A report from the Norwegian Arthroplasty Register. *Acta Orthop*. 2011;82(4):405-409. doi:10.3109/17453674.2011.588858
20. Gaspar MP, Lou J, Kane PM, Jacoby SM, Osterman AL, Culp RW. Complications Following Partial and Total Wrist Arthroplasty: A Single-Center Retrospective Review. *J Hand Surg*. 2016;41(1):47-53.e4. doi:10.1016/j.jhsa.2015.10.021
21. Vance MC, Packer G, Tan D, Crisco JJT, Wolfe SW. Midcarpal hemiarthroplasty for wrist arthritis: rationale and early results. *J Wrist Surg*. 2012;1(1):61-68. doi:10.1055/s-0032-1323644
22. Rossello MI. Short-term findings of a custom-made 3D-printed titanium partial scaphoid prosthesis and scapholunate interosseous ligament reconstruction. *BMJ Case Rep*. 2021;14(7):e241090. doi:10.1136/bcr-2020-241090
23. Honigmann P, Oonk J, Dobbe J, Strackee S, Streekstra G, Haefeli M. Patient-specific scaphoid prosthesis: surgical technique. *Arch Orthop Trauma Surg*. 2024;145(1):55. doi:10.1007/s00402-024-05609-7
24. Ferrero M, Carità E, Giacalone F, et al. Prosthetic Replacement of the Scaphoid Proximal Pole: Should It Be the Future? *Hand N Y N*. 2022;17(5):899-904. doi:10.1177/1558944720974120
25. Santos FL, Ferreira A, Grazina R, Sá D, Canela P, Lemos R. APSI scaphoid hemiarthroplasty - long-term results. *Rev Bras Ortop*. 2018;53(5):582-588. doi:10.1016/j.rboe.2018.07.011
26. Corain M, Colombo A, Lavagnolo U. The Adaptive Proximal Scaphoid Implant: Long-Term Follow-Up. *Hand*. Published online January 18, 2026:15589447251404959. doi:10.1177/15589447251404959
27. Spingardi O, Rossello MI. The total scaphoid titanium arthroplasty: A 15-year experience. *Hand N Y N*. 2011;6(2):179-184. doi:10.1007/s11552-010-9315-3
28. Felson DT, Gale DR, Elon Gale M, et al. Osteophytes and progression of knee osteoarthritis. *Rheumatol Oxf Engl*. 2005;44(1):100-104. doi:10.1093/rheumatology/keh411

29. Altman R, Asch E, Bloch D, et al. Development of criteria for the classification and reporting of osteoarthritis. Classification of osteoarthritis of the knee. Diagnostic and Therapeutic Criteria Committee of the American Rheumatism Association. *Arthritis Rheum*. 1986;29(8):1039-1049. doi:10.1002/art.1780290816
30. van der Kraan PM, van den Berg WB. Osteophytes: relevance and biology. *Osteoarthritis Cartilage*. 2007;15(3):237-244. doi:10.1016/j.joca.2006.11.006
31. Kessler S, Guenther KP, Puhl W. Scoring prevalence and severity in gonarthritis: the suitability of the Kellgren & Lawrence scale. *Clin Rheumatol*. 1998;17(3):205-209. doi:10.1007/BF01451048
32. Felson DT. Osteoarthritis as a disease of mechanics. *Osteoarthr Cartil OARS Osteoarthr Res Soc*. 2013;21(1):10-15. doi:10.1016/j.joca.2012.09.012
33. Longo UG, Papalia R, De Salvatore S, Picozzi R, Sarubbi A, Denaro V. Induced Models of Osteoarthritis in Animal Models: A Systematic Review. *Biology*. 2023;12(2):283. doi:10.3390/biology12020283
34. Lampropoulou-Adamidou K, Lelovas P, Karadimas EV, et al. Useful animal models for the research of osteoarthritis. *Eur J Orthop Surg Traumatol Orthop Traumatol*. 2014;24(3):263-271. doi:10.1007/s00590-013-1205-2
35. Serra CI, Soler C. Animal Models of Osteoarthritis in Small Mammals. *Veterinary Clin North Am Exot Anim Pract*. 2019;22(2):211-221. doi:10.1016/j.cvex.2019.01.004
36. McCoy AM. Animal Models of Osteoarthritis: Comparisons and Key Considerations. *Vet Pathol*. 2015;52(5):803-818. doi:10.1177/0300985815588611
37. Pearce AI, Richards RG, Milz S, Schneider E, Pearce SG. Animal models for implant biomaterial research in bone: a review. *Eur Cell Mater*. 2007;13:1-10. doi:10.22203/ecm.v013a01
38. Bendele AM. Animal models of osteoarthritis. *J Musculoskelet Neuronal Interact*. 2001;1(4):363-376.
39. Matsui Y, Iwasaki N, Kon S, et al. Accelerated development of aging-associated and instability-induced osteoarthritis in osteopontin-deficient mice. *Arthritis Rheum*. 2009;60(8):2362-2371. doi:10.1002/art.24705
40. Hayami T, Pickarski M, Zhuo Y, Wesolowski GA, Rodan GA, Duong LT. Characterization of articular cartilage and subchondral bone changes in the rat anterior cruciate ligament transection and meniscectomized models of osteoarthritis. *Bone*. 2006;38(2):234-243. doi:10.1016/j.bone.2005.08.007
41. Proffen BL, McElfresh M, Fleming BC, Murray MM. A comparative anatomical study of the human knee and six animal species. *The Knee*. 2012;19(4):493-499. doi:10.1016/j.knee.2011.07.005
42. Kamekura S, Hoshi K, Shimoaka T, et al. Osteoarthritis development in novel experimental mouse models induced by knee joint instability. *Osteoarthritis Cartilage*. 2005;13(7):632-641. doi:10.1016/j.joca.2005.03.004

43. Batiste DL, Kirkley A, Laverty S, Thain LMF, Spouge AR, Holdsworth DW. Ex vivo characterization of articular cartilage and bone lesions in a rabbit ACL transection model of osteoarthritis using MRI and micro-CT. *Osteoarthritis Cartilage*. 2004;12(12):986-996. doi:10.1016/j.joca.2004.08.010
44. Karamchedu NP, Murray MM, Sieker JT, et al. Bridge-Enhanced Anterior Cruciate Ligament Repair Leads to Greater Limb Asymmetry and Less Cartilage Damage Than Untreated ACL Transection or ACL Reconstruction in the Porcine Model. *Am J Sports Med*. 2021;49(3):667-674. doi:10.1177/0363546521989265
45. Fu SC, Cheuk YC, Hung LK, Chan KM. Limb Idleness Index (LII): a novel measurement of pain in a rat model of osteoarthritis. *Osteoarthritis Cartilage*. 2012;20(11):1409-1416. doi:10.1016/j.joca.2012.08.006
46. LaVallee KT, Maus TP, Stock JD, et al. Quantitation of Gait and Stance Alterations Due to Monosodium Iodoacetate-induced Knee Osteoarthritis in Yucatan Swine. *Comp Med*. 2020;70(3):248-257. doi:10.30802/AALAS-CM-19-000075
47. Jay GD, Elsaid KA, Kelly KA, et al. Prevention of cartilage degeneration and gait asymmetry by lubricin tribosupplementation in the rat following anterior cruciate ligament transection. *Arthritis Rheum*. 2012;64(4):1162-1171. doi:10.1002/art.33461
48. Little D, Johnson S, Hash J, et al. Functional outcome measures in a surgical model of hip osteoarthritis in dogs. *J Exp Orthop*. 2016;3(1):17. doi:10.1186/s40634-016-0053-5
49. Zhao R, Dong Z, Wei X, et al. Inflammatory factors are crucial for the pathogenesis of post-traumatic osteoarthritis confirmed by a novel porcine model: “Idealized” anterior cruciate ligament reconstruction" and gait analysis. *Int Immunopharmacol*. 2021;99:107905. doi:10.1016/j.intimp.2021.107905
50. Donnenfield JI, Karamchedu NP, Proffen BL, Molino J, Murray MM, Fleming BC. Predicting severity of cartilage damage in a post-traumatic porcine model: Synovial fluid and gait in a support vector machine. *PloS One*. 2022;17(6):e0268198. doi:10.1371/journal.pone.0268198
51. Cake M, Read R, Edwards S, et al. Changes in gait after bilateral meniscectomy in sheep: effect of two hyaluronan preparations. *J Orthop Sci Off J Jpn Orthop Assoc*. 2008;13(6):514-523. doi:10.1007/s00776-008-1279-6
52. Fleming BC, Hulstyn MJ, Oksendahl HL, Fadale PD. Ligament injury, reconstruction, and osteoarthritis. *Curr Opin Orthop*. 2005;16:354-362.
53. Gabay O, Gabay C. Hand osteoarthritis: New insights. *Jt Bone Spine Rev Rhum*. Published online August 4, 2012. doi:10.1016/j.jbspin.2012.06.011
54. Kwok WY, Vliet Vlieland TPM, Rosendaal FR, Huizinga TWJ, Kloppenburg M. Limitations in daily activities are the major determinant of reduced health-related quality of life in patients with hand osteoarthritis. *Ann Rheum Dis*. 2011;70(2):334-336. doi:10.1136/ard.2010.133603
55. Vaughan QM, Morton AM, Moore D, Akelman E, Crisco JJ. Development of small bone implants using a mean shape bone in a porcine model for carpal

bone replacement. *Proc Inst Mech Eng [H]*. Published online July 24, 2025:9544119251355382. doi:10.1177/09544119251355382

56. Little CB, Smith MM, Cake MA, Read RA, Murphy MJ, Barry FP. The OARSI histopathology initiative - recommendations for histological assessments of osteoarthritis in sheep and goats. *Osteoarthritis Cartilage*. 2010;18 Suppl 3:S80-92. doi:10.1016/j.joca.2010.04.016
57. LaVallee KT, Maus TP, Stock JD, et al. Quantitation of Gait and Stance Alterations Due to Monosodium Iodoacetate-induced Knee Osteoarthritis in Yucatan Swine. *Comp Med*. 2020;70(3):248-257. doi:10.30802/AALAS-CM-19-000075
58. Kaiser EE, Waters ES, Fagan MM, et al. Characterization of tissue and functional deficits in a clinically translational pig model of acute ischemic stroke. *Brain Res*. 2020;1736:146778. doi:10.1016/j.brainres.2020.146778

Chapter 5: Osteophytes Develop in a Porcine Wrist Model for Ligament Injury and Small Bone Replacement, Yet Joint Space Remains Unchanged

Chapters 4 and 5 have been combined into the following manuscript.

Vaughan QM, Morton AM, Moore DC, Molino J, Akelman E, Crisco JJ. Small Bone Replacement Leads to Greater Gait Asymmetry, Cartilage Damage, and Osteophyte Formation Than Ligament injury in a Porcine Wrist Model. (UNDER REVIEW: *Osteoarthritis and Cartilage OPEN)*

5.1. Abstract

Osteophyte formation and joint space narrowing are indicators of osteoarthritis (OA). While OA has been extensively studied in humans and replicated in animal models for larger joints (e.g., the knee), few studies have quantified these characteristics in animal models of the human wrist. This study evaluates the Yucatan minipig (YMP) carpus as a preclinical model for the human wrist to assess osteophyte volume and joint space following ligament injury and small bone replacement. Eight YMP's were assigned to a ligament injury or small bone replacement group for a 12-week *in vivo* study. After euthanasia, bilateral forelimbs were scanned using micro-computed tomography. Three-dimensional (3D) bone models were generated to quantify osteophyte volume via Boolean subtraction of the contralateral from the experimental bone. Joint space was measured between manually identified articular surfaces. Osteophyte volume, expressed as a percentage of contralateral bone volume, was greater in the small bone replacement group than the ligament injury group for seven of twelve forelimb bones ($p<0.005$). Joint space did not differ between contralateral and experimental limbs nor between experimental limbs across groups. Osteophyte formation in the YMP wrist was evident prior to joint space narrowing following ligament injury and small bone replacement at 12 weeks. Osteophyte volume was greater in the small bone replacement group than in the ligament injury group, with no observed correlation between osteophyte volume and joint space. These findings support the YMP as a feasible preclinical model for assessing OA severity and small bone replacement in the human wrist.

5.2. Introduction

Osteoarthritis (OA) is often characterized by osteophyte formation [1–3] and joint space narrowing.[4–8] Osteophytes are fibrocartilage-capped bony outgrowths that contribute to pain and loss of function,[9–11] while joint space narrowing has been found to correlate with loss of cartilage thickness.[1,12] The extent of osteophyte formation and joint space narrowing, as assessed radiographically, provides a reliable indicator of OA severity.[1,3,4]

Surgical treatment options for end stage OA include wrist fusion (arthrodesis),[13,14] proximal row carpectomy,[15–17] and total wrist replacement (arthroplasty).[18–21] For individuals with advanced OA in the wrist, arthroplasty is often recommended to improve quality of life. For patients with viable articular cartilage on one joint surface, replacing an individual carpal bone offers a motion-preserving alternative to wrist fusion or total arthroplasty.[22,23] There are, however, limited studies investigating the relationship between osteophyte growth and joint space narrowing before and after treatment with a small bone implant in the wrist, specifically in a large animal model.

Animal models play a critical role in advancing our understanding of OA severity and in developing effective treatment options. However, the use of animal models presents several limitations, including anatomical differences, variations in joint dimensions and loading between quadrupeds and bipeds, and differences in cartilage thickness.[24,25] One of the most common methods for studying OA of the knee joint, in an animal model, is by inducing OA through transection of the ACL, which has been widely applied in species such as canines,[26] mice,[27–30]

rabbits,[31] and swine.[32–34] While these models provide valuable insights into OA models for such large joints, there remains a lack of a suitable animal model for smaller, more complex joints such as the human wrist.

Recently, the Yucatan minipig (YMP) has been proposed as an animal model for the human wrist [35–37] due to similarities in bone composition [25] and ligamentous anatomy,[37] making it a desirable model for preclinical testing of implants and treatments for wrist OA. The YMP carpus consists of a radius, ulna, eight carpal bones and four metacarpals, all connected by ligaments, with an overall orientation analogous to the human wrist. The YMP carpus has previously been used to model scaphoid nonunion,[35] in a biologic joint replacement study for trapeziometacarpal OA,[36] and to assess YMP carpus biomechanics after radial intermediate ligament (RIL) and dorsal intercarpal ligament (DIC) transection, to replicate a scapholunate interosseous ligament (SLIL) and DIC injury in the human wrist.[37] However, to further support the use of the YMP carpus as a preclinical model for the human wrist, it is important to characterize its skeletal response to ligament injury and treatment with a small bone replacement.

The specific aim of this study was to assess OA severity in the YMP carpus following ligament injury and small bone replacement. OA severity was quantified by computing osteophyte volume and joint space in the carpus after a 12-week *in vivo* study. We hypothesized that animals in the ligament injury group would exhibit significantly greater osteophyte measures than those receiving a small bone replacement, as ligament injuries are known to lead to OA.[38–40] Furthermore, we hypothesized that joint spaces in the experimental limb of the ligament injury

group would be narrower than those in the small bone replacement group, and within each treatment group, the experimental limb would have narrower joint spaces than the contralateral limb. Based on the established association between osteophyte volume and joint space in human OA,[1,9,41–43] we further hypothesized that increased osteophyte volume would correlate with joint space narrowing.

5.3. Methods

5.3.1. Forelimb Acquisition

Eight Yucatan minipigs (YMP), at least 24 months of age with no prior history of gait asymmetry or forelimb injury, were acquired through purchase for an unblinded *in vivo* study evaluating the YMP as a preclinical animal model for ligament injury and small bone replacement. In this cohort, there were 4 females and 4 males ranging in age from 24.4 to 29.8 months (mean: 25.7 ± 1.8 months) and weight from 56.9 to 101.2 kg (mean: 84.2 ± 13.6 kg) (Sinclair Bio-Resources, Windham, ME; Premier BioSource, Ramona, CA). An additional six YMP's were acquired from naïve animals used in an unrelated knee study. The wrists in this cohort were used to evaluate left to right carpal bone size differences. These animals included 3 females and 3 males ranging in age from 32.1 to 41.3 months (mean: 38.1 ± 3.3 months) and weight from 66.0 to 99.9 kg (mean: 79.6 ± 14.9 kg) (Sinclair Bio-Resources, Windham, ME). All animals were acquired following IACUC review and approval.

For the eight animals included in the *in vivo* study, four animals were assigned to the ligament injury group, in which the radial intermediate ligament (RIL) and dorsal intercarpal ligament (DIC) were transected (n=4; 2F, 2M; ligament injury

group), and a small bone replacement group, in which the radial carpal bone (RCB) was replaced with a custom Cobalt-Chrome (CoCr) implant (n=4; 2F, 2M; implant group).[44] All surgeries were performed on the right forelimb by a board-certified hand surgeon and all animals were post-operatively monitored for 12 weeks and allowed unrestricted weight bearing. Following the end of the 12-week *in vivo* study, the right and left wrists were harvested from each animal by sectioning the midshaft of the radius and ulna, and the midshaft of the metacarpals. For the implant group, the CoCr implant was removed from the right carpus through a small dorsal incision centered over the proximal carpal row. After harvest and preparation, all wrists were fixed in formalin.

5.3.2. Imaging and Bone Model Generation

The wrists harvested from the *in vivo* animals were imaged using a SKYSCAN 1276 micro-computed tomography (μCT) scanner (Bruker, Billerica, MA) with an isometric voxel resolution of 0.1205 mm. The forelimbs harvested from the control group were imaged using a clinical CT scanner (GE Healthcare, Chicago, IL) with an image resolution of 0.4 mm x 0.4 mm in-plane and 0.625 mm slice thickness. The carpal bones, radius and ulna, and metacarpals in each image were segmented in MIMICS v22 (Materialise, Leuven, Belgium) using a density-based threshold and manual editing to delineate the bone's outer cortical surface. Three-dimensional (3D) models of all cortical bone surfaces were exported as closed triangular meshes with no triangle reduction and minimal smoothing (iterations: 1; smooth factor: 0.030). All left bone models were mathematically mirrored to the right for consistent orientation. Coordinate systems for each carpal bone were

constructed by calculating the bones' geometric centroids as the origins and the principal inertial axes as the coordinate axes. The coordinate systems for the metacarpals and the combined radius and ulna were defined using manually identified anatomical landmarks on the bone models.[45] Metacarpal landmarks included the lateral base of MC3, medial base of MC4, and four points around the midshaft of MC3 and MC4. Radius and ulna landmarks included the radial and ulnar styloid, and four midshaft points around the radius and ulna. The directions of the coordinate system axes were defined as X in the volar-dorsal direction, Y in the proximal-distal direction, and Z in the radial-ulnar direction (**Figure 5.1**). Bone volume was calculated for each bone model using custom-written code.

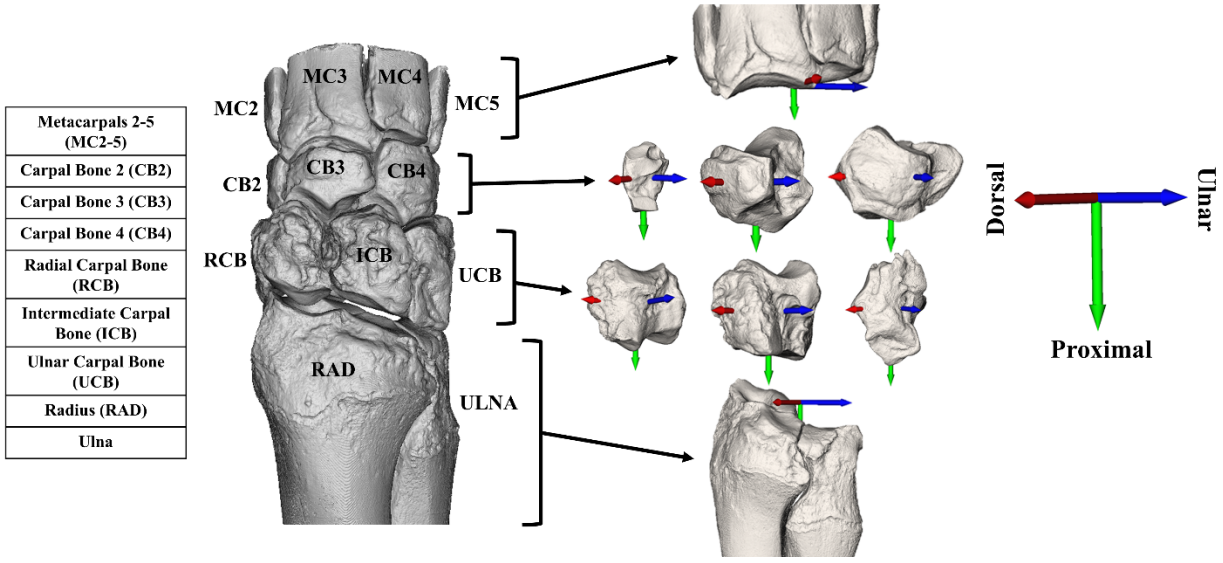

Figure 5.1. 3D model of the right YMP carpus generated from micro-CT images, depicting the radius (RAD), ulna, two carpal rows, and metacarpals. Carpal bones are represented in their inertial coordinate system, while the radius, ulna, and metacarpals are represented in their anatomical coordinate systems. Standardized orientation of the coordinate systems is indicated by the axes: dorsal (positive X; red), proximal (positive Y; green), and ulnar (positive Z; blue).

5.3.3. Osteophyte Volume Calculations

Osteophyte volume was calculated by Boolean subtraction of the contralateral bone model from the experimental bone model following previously established algorithms.[46] To do so, the contralateral bone models were registered to the experimental bone models using the coordinate systems as an initial registration, followed by a dissimilarity-excluding Procrustes (DEP) registration approach, which is a least-squares superimposition (rotation, translation) algorithm that excludes localized dysmorphologies while optimizing alignment of the bone models. Superimposition was performed with DEP without scaling the contralateral bone model. Osteophyte volume calculations were performed for the distal epiphysis of the radius and ulna, and the proximal metaphysis of the metacarpals. To do so, the radius and ulna bone models were digitally trimmed by a transverse plane located at the growth plate. The metacarpals were digitally trimmed 16 mm from the proximal articular surface, the shortest length at which osteophytes were observed. Osteophyte models for all bones were generated using Boolean subtraction (experimental-contralateral); all portions of experimental bone that fell outside of the registered contralateral bone models were considered osteophytes (Geomagic Wrap 2021; 3D Systems, SC) (**Figure 5.2**).[46] For the control group, the steps for registration and Boolean subtraction were repeated by treating the right bones as the experimental model and the left as the contralateral, with the resulting model defined as the bone difference. The volume of each osteophyte model was calculated using open-source code that requires the model to be a closed triangular surface and utilizes a discrete form of the divergence theorem to convert volume integration to an area integral over the boundary of the

triangular surface.[47,48] To account for differences in bone size across animals, osteophyte volumes were normalized by the total volume of the contralateral bones and reported as a percentage (%) of total bone volume. To establish a baseline for detecting normal side-to-side variations in bone size this process was then repeated with the left and right control bone models.

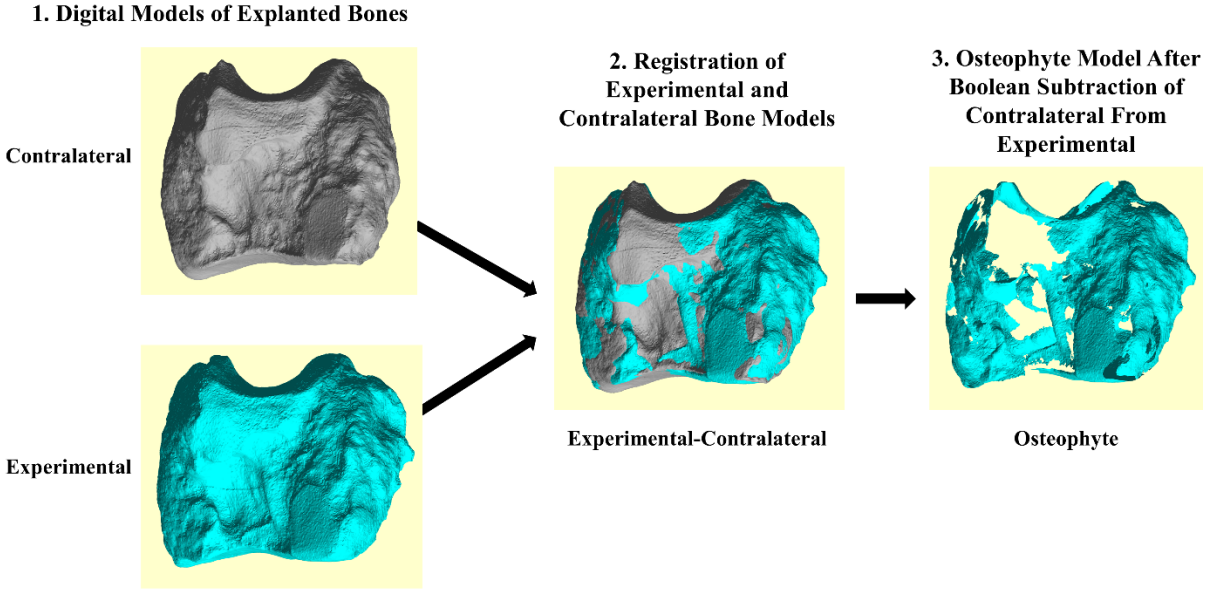

Figure 5.2. The contralateral bone model is registered to the experimental bone model, and a Boolean subtraction is performed on the co-registered models to yield the osteophyte model.

Osteophyte formation on each carpal bone was characterized in terms of new bone formed in each of eight anatomic locations on the bones (e.g. dorsal-distal-radial, dorsal-proximal-radial, dorsal-distal-ulnar, dorsal-proximal-ulnar, volar-distal-radial, volar-proximal-radial, volar-distal-ulnar, volar-proximal-ulnar), defined by a cube fit at the origin of the coordinate system (**Figure 5.3**). For the metacarpals, radius, and ulna, osteophyte volume was characterized by using only four anatomic locations (e.g. dorsal-radial, dorsal-ulnar, volar-radial, volar-ulnar)

to exclude variations associated with differences along the bone shafts. Boolean intersection between the cube and the osteophyte model (Geomagic Wrap 2021; 3D Systems, SC) was used to determine osteophyte volume at each anatomic location and then normalized by the contralateral bone volume and reported as a percentage (%) of total bone volume.

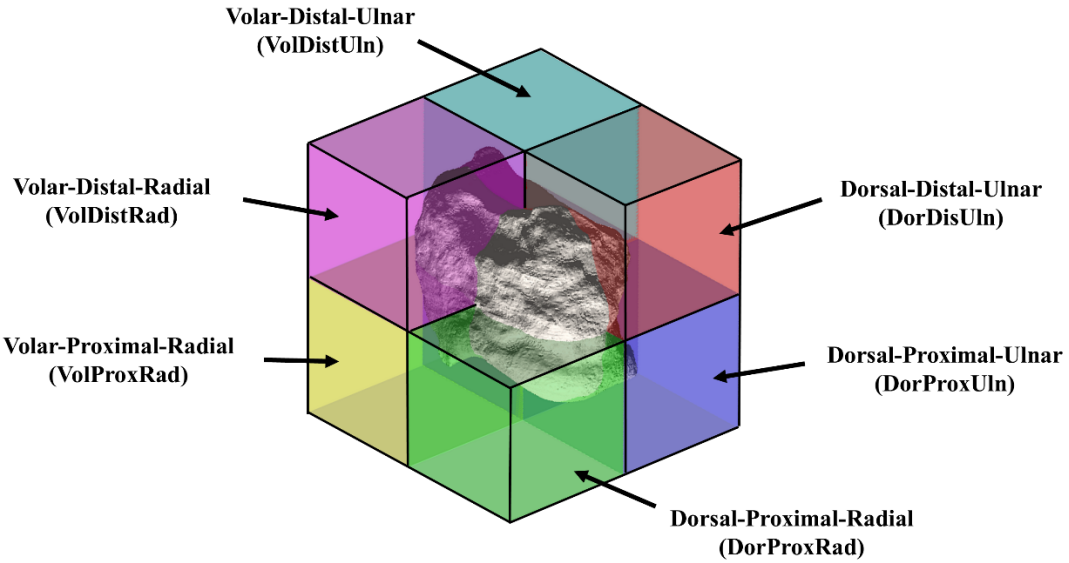

Figure 5.3. Dorsal-radial view of the RCB, with eight cubes positioned at the origin of the RCB inertial coordinate system depicting the eight anatomical regions of the RCB osteophyte bone model separately analyzed for osteophyte development. The dorsal-distal-radial (DorDistRad) location of the RCB osteophyte model is displayed.

5.3.4. Joint Space Measurements

Joint space was computed by calculating the inter-bone spacing between 19 sets of mating bone surfaces for the ligament injury group and 17 sets of surfaces for the small bone replacement group (**Figure 5.4**).

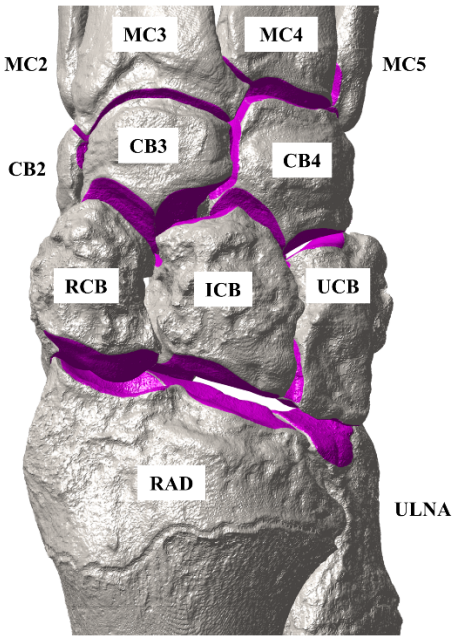

Articular Surfaces
ICB-RAD
ICB-CB3
ICB-CB4
ICB-UCB
UCB-ULNA
UCB-CB4
CB4-MC4
CB4-MC5
MC5-MC4
CB4-CB3
MC3-MC4
CB4-MC3
CB3-MC3
CB2-MC2
CB2-MC3
CB2-CB3
MC2-MC3
RCB-RAD
RCB-CB2/CB3

Figure 5.4. Articular surfaces (purple) analyzed for joint space (mm) for the ligament injury and small bone replacement groups. For the small bone replacement group, surfaces articulating with the RCB were excluded (RCB-RAD and RCB-CB2/CB3).

Each surface within the carpus was manually identified based on the smooth contours of the subchondral bone and defined as a boundary in Geomagic Wrap 2021 (3D Systems, SC). The segmented surfaces were exported (**Figure 5.5**), and the distances between the surface models were computed. Node-to-node distance was computed by identifying, for each node on the surface model (triangular surface mesh vertices), along its corresponding node surface normal, the nearest neighbor node on the articulating pair surface model (dist2surf.m; iso2mesh). The mean and standard deviation of the distances between each surface pair were reported for the contralateral and experimental limbs for each animal in the ligament injury group and small bone replacement group.

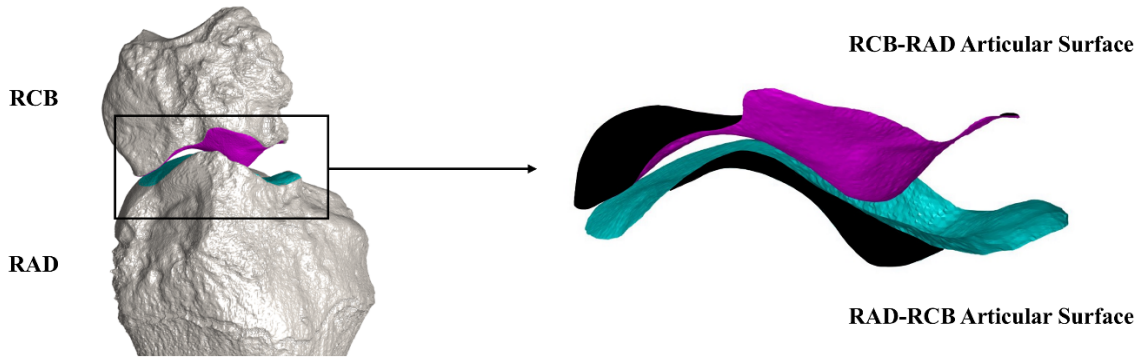

Figure 5.5. 3D models of the manually identified articular surfaces between the RCB (purple) and the radius (blue), used to compute joint space.

5.3.5. Statistical Analysis

Descriptive statistics (mean and standard deviation) were computed for osteophyte and bone volume in the control, ligament injury, and small bone replacement groups, and joint space in the contralateral and experimental forelimbs for both the ligament injury and small bone replacement groups. Generalized estimating equations (GEE) were used to compare osteophyte and bone difference volumes across groups (control, ligament injury, and small bone replacement), and joint space between contralateral and experimental forelimbs within and across the ligament injury and small bone replacement groups. The residuals from each GEE model and the distribution of the osteophyte volume and joint space were used to determine the distribution and link function specified in the regression model. A binomial distribution and logit link function were used to analyze osteophyte volume. For joint space, a Gaussian distribution and identity link function were employed. Classical sandwich estimation was used in all models to protect against possible model misspecification. Post hoc pairwise comparisons between ligament injury and small bone replacement groups, and contralateral

and experimental forelimbs were conducted within the model via orthogonal contrasts. Where appropriate, the Holm test was used to adjust for multiple comparisons and to maintain a two-tailed familywise alpha of 0.05. Linear regression was used to examine the relationship between osteophyte volume and joint space. The residuals from the linear regression model were examined to ensure that all model assumptions were satisfied. Beta values, correlation coefficients, and R-squared values were reported. An interaction term between the independent variable and study group was examined to determine if the relationship between osteophyte volume and joint space differed between ligament injury and small bone replacement groups. A p-value < 0.05 was used to determine statistical significance.

5.4. Results

5.4.1. Healthy Control Bone Volumes

There were no significant differences in bone volume between the left and right carpal bones in the healthy controls (**Appendix, Supplementary Table 5.1**). The variation in bone volume ranged from 0.5 % to 7.1%, with the smallest variation observed in the ICB (0.5 ± 8.2 %) and the greatest in the RCB (7.1 ± 5.6 %).

5.4.2. Osteophyte Volume for Ligament Injury and Small Bone Replacement Groups

In the ligament injury group, the average osteophyte volumes were 10.4 ± 3.3 % for MC2, 9.0 ± 7.9 % for MC3, 6.4 ± 3.0 % for MC4, 6.6 ± 3.3 % for MC5, 7.2 ± 2.8 % for CB2, 7.0 ± 1.7 % for CB3, 5.5 ± 1.4 % for CB4, 10.9 ± 2.0 % for RCB, 7.1 ±

1.8 % for the ICB, 7.8 ± 3.4 % for the UCB, 2.3 ± 0.6 % for radius, and 6.3 ± 1.7 % for ulna (**Figure 5.6**). In the small bone replacement group, osteophyte volumes were significantly greater compared to the ligament injury group by 5.1 % for MC4 ($p=0.05$), 6.8 % for MC5 ($p=0.03$), 20.1 % for CB2 ($p<0.0001$), 10.4 % for CB3 ($p=0.0005$), 12.1 % for CB4 ($p<0.0001$), 14.4 % for ICB ($p=0.002$), and 4.1 % for the radius ($p=0.02$) (**Figure 5.6**). Osteophyte volume did not differ for MC2 ($p=0.10$), MC3 ($p=0.57$), UCB ($p=0.07$), and the ulna ($p=0.89$) between the ligament injury and small bone replacement groups. Compared to the bone differences calculated through Boolean subtraction of the control group, osteophyte volumes in the ligament injury group were significantly greater by 4.2 % for CB3 ($p=0.0005$), 2.7 % for CB4 ($p=0.007$), and 9.1 % for RCB ($p=0.0005$). Compared to the control group, osteophyte volumes in the small bone replacement group were significantly greater by 7.6 % for MC3 ($p=0.02$), 7.0 % for MC4 ($p=0.02$), 23.1 % for CB2 ($p<0.0001$), 14.6 % for CB3 ($p<0.0001$), 14.8 % for CB4 ($p<0.0001$), and 16.9 % for ICB ($p=0.005$).

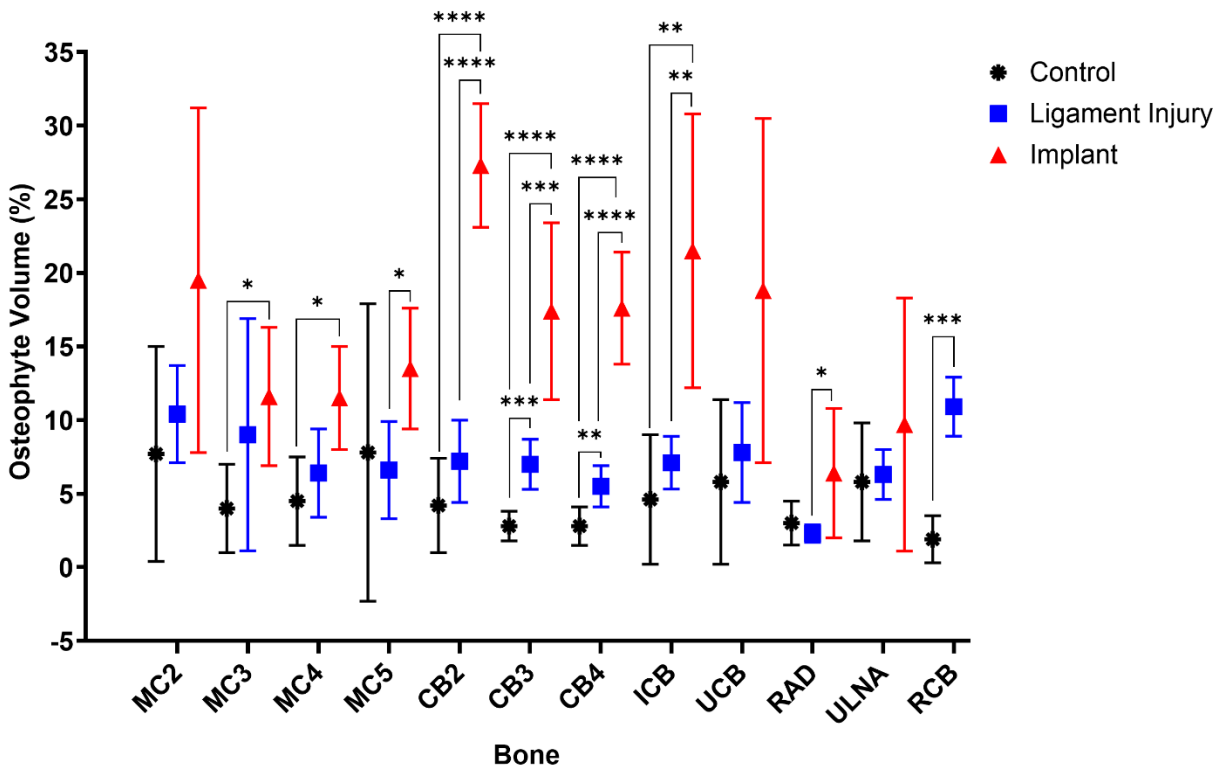

Figure 5.6. Osteophyte volume (average and SD) as a percentage of contralateral bone volume for the ligament injury group (n=4; blue), and the small bone replacement group (n=4; red). Osteophyte volume was significantly more extensive in the small bone replacement group after harvest at 12 weeks. For comparison, the volume of the bone differences of the control group (n=6; black) were significantly smaller in 3 bones compared to the ligament injury group and 6 bones compared to the small bone replacement group. Significant differences are denoted by an asterisk (* = $p<0.05$; ** = $p<0.01$; *** = $p<0.001$; **** = $p<0.0001$).

Osteophyte volume was predominantly observed at the dorsal, proximal, distal, and radial locations in both the ligament injury and small bone replacement groups (**Appendix, Supplementary Table 5.2**). In the ligament injury group, the greatest osteophyte volume was observed at the dorsal-distal-radial location of RCB (mean: 2.7 ± 0.5 %). In the small bone replacement group, the greatest osteophyte volume was observed at the dorsal-proximal-radial location of CB2 (mean: 5.6 ± 1.7 %).

5.4.3. Joint Space for Ligament Injury and Small Bone Replacement Groups

There was no detectable loss in joint space in the operated forelimb of the LI (average across all surfaces analyzed was 1.0 ± 0.5 mm) or in the SBR (average across all articular surfaces was 0.9 ± 0.3 mm) groups, when compared with the joint spaces in the contralateral limbs (approximately 0.9 ± 0.4 mm) (**Table 5.1**).

Table 5.1. Average (± standard deviation) joint space for each articular surface in the contralateral and operated limbs of the ligament injury and small bone replacement groups. No significant differences in joint space were observed within or between groups. The corresponding articular surfaces are illustrated in Figure 5.4.

Articular Surface	Ligament Injury (LI)		Small Bone Replacement (SBR)	
	Contralateral (mm)	Operated (mm)	Contralateral (mm)	Operated (mm)
ICB-RAD	1.9 ± 0.2	2.1 ± 0.1	1.8 ± 0.3	1.6 ± 0.3
ICB-CB3	1.6 ± 0.2	1.6 ± 0.1	1.6 ± 0.3	1.5 ± 0.1
ICB-CB4	0.8 ± 0.2	0.9 ± 0.2	0.8 ± 0.1	0.8 ± 0.0
ICB-UCB	0.6 ± 0.1	0.7 ± 0.1	0.7 ± 0.1	0.7 ± 0.1
UCB-ULNA	1.2 ± 0.1	1.3 ± 0.3	1.1 ± 0.1	1.2 ± 0.1
UCB-CB4	1.1 ± 0.1	1.1 ± 0.0	1.0 ± 0.1	1.1 ± 0.1
CB4-MC4	0.9 ± 0.1	0.9 ± 0.2	1.0 ± 0.1	1.0 ± 0.1
CB4-MC5	1.0 ± 0.4	1.1 ± 0.4	0.9 ± 0.2	1.1 ± 0.3
MC5-MC4	0.8 ± 0.1	0.9 ± 0.0	0.8 ± 0.1	0.9 ± 0.0
CB4-CB3	0.6 ± 0.1	0.6 ± 0.1	0.6 ± 0.1	0.6 ± 0.0
MC3-MC4	0.5 ± 0.0	0.5 ± 0.0	0.5 ± 0.0	0.6 ± 0.0
CB4-MC3	1.1 ± 0.1	1.1 ± 0.4	1.2 ± 0.2	1.2 ± 0.3
CB3-MC3	0.6 ± 0.0	0.6 ± 0.1	0.6 ± 0.1	0.7 ± 0.1
CB2-MC2	0.8 ± 0.2	0.8 ± 0.2	0.9 ± 0.2	0.9 ± 0.2
CB2-MC3	0.7 ± 0.0	0.7 ± 0.1	0.7 ± 0.1	0.8 ± 0.1
CB2-CB3	0.4 ± 0.1	0.4 ± 0.1	0.4 ± 0.1	0.5 ± 0.1
MC2-MC3	0.7 ± 0.1	0.6 ± 0.1	0.6 ± 0.1	0.7 ± 0.1
RCB-RAD	1.7 ± 0.1	1.8 ± 0.2		
RCB-CB2/CB3	1.1 ± 0.1	1.1 ± 0.2		

5.4.4. Correlation Between Osteophyte Volume and Joint Space

No correlation was observed between osteophyte volume and joint space in the ligament injury group ($r= 0.01$, $R^2= 0.0002$) nor small bone replacement group ($r= -0.4$, $R^2= 0.13$).

5.5. Discussion

In this study, we aimed to evaluate OA severity in the YMP carpus following ligament injury and small bone replacement by quantifying osteophyte volume and joint space for the bones in the carpus following a 12-week *in vivo* study involving ligament transection (n=4) and radial carpal bone replacement (n=4) in YMPs. We hypothesized that osteophyte volume would be greater in the ligament injury group compared to the small bone replacement group as ligament injuries are known to lead to OA.[38–40] Contrary to our hypothesis, osteophyte volume was significantly greater in the small bone replacement group compared to the ligament injury group (mean difference: 9.0 %). Additionally, we hypothesized that joint spaces in the experimental limb of the ligament injury group would be narrower compared to the experimental limb of the small bone replacement group. However, no significant differences in joint space were observed between the contralateral and experimental limbs within or across the ligament injury and small bone replacement groups. Finally, we hypothesized a negative correlation between osteophyte volume and joint space but observed no significant correlation in the ligament injury ($r=0.01$; $p=0.96$) or small bone replacement ($r=-0.4$; $p=0.19$) groups.

When analyzing osteophyte volume for the ligament injury or small bone replacement groups, a highlight of our findings was that osteophyte formation was observed on all the bones in the carpus and not limited to the bones that articulate directly with the RCB. In the ligament injury group, osteophyte volume was mainly observed in the dorsal, proximal, distal and radial regions of the metacarpals and carpal bones. In the small bone replacement group, osteophyte volume was mainly located in the volar and dorsal regions of the metacarpals and carpal bones (**Appendix, Supplementary Table 5.2**). These findings suggest that the YMP may have had a biological response to the trauma induced by the surgical procedure since osteophyte formation was not restricted to the bones surrounding the RCB. However, the cause behind the new bone formation remains uncertain.

Osteophyte formation and joint space narrowing have been extensively studied in the context of OA in both the human wrist [6–8,49–54] and knee.[1,12,55] In rodent models of knee OA, osteophyte development has been found to emerge within weeks after joint destabilization. For example, Das Neves Borges et al. observed significant osteophyte formation beginning 4 weeks after medial meniscus destabilization,[56] while similar growth was reported by Hayami et al. following surgical induction via ligament transection and meniscal resection.[28] In our study of the YMP carpus, osteophyte formation was observed at the 12-week post-operative time point in both the ligament injury and small bone replacement groups (**Appendix, Supplementary Figure 5.1**), although the onset timing of osteophytes remains uncertain. To our knowledge, this is the first preclinical

animal model study that utilizes the YMP as a translational model for wrist OA to report both osteophyte volume and joint space.

In contrast, joint space narrowing, another hallmark of OA, was not observed in the experimental limb of either the ligament injury or small bone replacement groups in the YMP model. Although joint space narrowing has not been widely reported in animal models of OA, it has been consistently documented in wrist OA, specifically in the trapeziometacarpal,[6,52] carpometacarpal,[7] and pisotriquetral [54] joints. The presence of osteophytes prior to joint space narrowing in both experimental groups suggests that the study duration may have been insufficient to reproduce end-stage OA with joint space narrowing in the YMP model. Consequently, the lack of joint space narrowing in the experimental limbs explains the absence of a correlation between osteophyte volume and joint space narrowing in the YMP carpus. Our findings in the YMP carpus contrast with clinical findings from Zhang et al., who reported this relationship in older females with prior knee injury,[57] and Nakasa et al., who found a similar relationship in osteochondral lesions of the talus.[41] However, osteophytes can develop in the early stages of OA, often preceding joint space narrowing, as defined by the Kellgren-Lawrence grading scale.[11,58]

Although osteophyte volume and joint space were successfully quantified in a preclinical animal model of ligament injury and small bone replacement, this study has several limitations. The most notable limitation was the sample size (n= 4 per group), which limited our ability to assess sex-specific effects within and across the ligament injury and small bone replacement groups, and to evaluate the

robustness of differences in osteophyte volume between the groups. Another limitation was measurements of osteophyte volume and joint space narrowing at a single time point, which prevented assessment of the timing of the onset and progression of osteophyte formation and joint space narrowing. The 12-week duration of the *in vivo* study may also have been insufficient to detect joint space narrowing. While osteophyte volume was observed, it has previously been reported that the presence of osteophytes precedes joint space narrowing,[11,58] indicating the YMP carpus may have been in the early stages of OA. Additionally, carpal orientation during formalin fixation and post-harvest imaging, as well as the absence of weightbearing during joint space analysis, may have contributed to variability in joint space measurements. Each carpus was placed in a visually neutral position during formalin fixation; however, some articular surfaces were not fully mated as visible in the 3D model of the carpus (**Appendix, Supplementary Figure 5.2**). Future histological analyses are needed to confirm whether the identified osteophyte models represent bone remodeling and whether joint space measurements accurately reflect cartilage degradation.

5.6. Acknowledgments

The authors thank Scott Mc Allister for assistance in specimen acquisition and animal care.

5.7. References

1. Felson DT, Gale DR, Elon Gale M, et al. Osteophytes and progression of knee osteoarthritis. *Rheumatol Oxf Engl*. 2005;44(1):100-104. doi:10.1093/rheumatology/keh411
2. Goldring SR. Alterations in periarticular bone and cross talk between subchondral bone and articular cartilage in osteoarthritis. *Ther Adv Musculoskelet Dis*. 2012;4(4):249-258. doi:10.1177/1759720X12437353
3. Altman R, Asch E, Bloch D, et al. Development of criteria for the classification and reporting of osteoarthritis. Classification of osteoarthritis of the knee. Diagnostic and Therapeutic Criteria Committee of the American Rheumatism Association. *Arthritis Rheum*. 1986;29(8):1039-1049. doi:10.1002/art.1780290816
4. Kortekaas MC, Kwok WY, Reijnierse M, Huizinga TWJ, Kloppenburg M. Osteophytes and joint space narrowing are independently associated with pain in finger joints in hand osteoarthritis. *Ann Rheum Dis*. 2011;70(10):1835-1837. doi:10.1136/ard.2010.147553
5. Poulet B, Staines KA. New developments in osteoarthritis and cartilage biology. *Curr Opin Pharmacol*. 2016;28:8-13. doi:10.1016/j.coph.2016.02.009
6. D'Agostino P, Dourthe B, Kerkhof F, Harry Van Lenthe G, Stockmans F, Vereecke EE. In vivo biomechanical behavior of the trapeziometacarpal joint in healthy and osteoarthritic subjects. *Clin Biomech Bristol Avon*. 2017;49:119-127. doi:10.1016/j.clinbiomech.2017.09.006
7. Halilaj E, Moore DC, Patel TK, et al. Older asymptomatic women exhibit patterns of thumb carpometacarpal joint space narrowing that precede changes associated with early osteoarthritis. *J Biomech*. 2015;48(13):3643-3649. doi:10.1016/j.jbiomech.2015.08.010
8. Lalone EA, MacDermid J, King G, Grewal R. The Effect of Distal Radius Fractures on 3-Dimensional Joint Congruency. *J Hand Surg*. 2021;46(1):66.e1-66.e10. doi:10.1016/j.jhsa.2020.05.027
9. Wong SHJ, Chiu KY, Yan CH. Review Article: Osteophytes. *J Orthop Surg Hong Kong*. 2016;24(3):403-410. doi:10.1177/1602400327
10. Kalshoven JM, Badida R, Morton AM, Molino J, Crisco JJ. Do osteophytes alter thumb carpometacarpal Biomechanics? a preliminary in vitro study. *J Biomech*. 2024;176:112333. doi:10.1016/j.jbiomech.2024.112333
11. van der Kraan PM, van den Berg WB. Osteophytes: relevance and biology. *Osteoarthritis Cartilage*. 2007;15(3):237-244. doi:10.1016/j.joca.2006.11.006
12. Buckland-Wright JC, Macfarlane DG, Lynch JA, Jasani MK, Bradshaw CR. Joint space width measures cartilage thickness in osteoarthritis of the knee: high resolution plain film and double contrast macroradiographic investigation. *Ann Rheum Dis*. 1995;54(4):263-268.
13. Adams BD, Kleinhenz BP, Guan JJ. Wrist Arthrodesis for Failed Total Wrist Arthroplasty. *J Hand Surg*. 2016;41(6):673-679. doi:10.1016/j.jhsa.2016.02.012

14. Rodriguez-Merchan EC, Tabeayo-Alvarez ED, Shojaie B, Kachooei AR. Total Wrist Arthrodesis: An Update on Indications, Technique and Outcomes. *Arch Bone Jt Surg*. 2023;11(3):144-153. doi:10.22038/ABJS.2022.65875.3154
15. Kay HF, Kang HP, Alluri R, Azad A, Ghiassi A. Proximal Row Carpectomy Versus 4-Corner Fusion: Incidence, Conversion to Fusion, and Cost. *J Hand Surg*. Published online February 20, 2020. doi:10.1016/j.jhsa.2019.12.010
16. Chim H, Moran SL. Long-Term Outcomes of Proximal Row Carpectomy: A Systematic Review of the Literature. *J Wrist Surg*. 2012;1(2):141-148. doi:10.1055/s-0032-1329547
17. Dacho AK, Baumeister S, Germann G, Sauerbier M. Comparison of proximal row carpectomy and midcarpal arthrodesis for the treatment of scaphoid nonunion advanced collapse (SNAC-wrist) and scapholunate advanced collapse (SLAC-wrist) in stage II. *J Plast Reconstr Aesthetic Surg JPRAS*. 2008;61(10):1210-1218. doi:10.1016/j.bjps.2007.08.007
18. Wagner ER, Srnec JJ, Fort MW, Barras LA, Rizzo M. Outcomes of Revision Total Wrist Arthroplasty. *J Am Acad Orthop Surg Glob Res Rev*. 2021;5(3). doi:10.5435/JAAOSGlobal-D-21-00035
19. Cavaliere CM, Chung KC. A systematic review of total wrist arthroplasty compared with total wrist arthrodesis for rheumatoid arthritis. *Plast Reconstr Surg*. 2008;122(3):813-825. doi:10.1097/PRS.0b013e318180ece3
20. Nair R. Review article: Total wrist arthroplasty. *J Orthop Surg Hong Kong*. 2014;22(3):399-405.
21. Carlson JR, Simmons BP. Total wrist arthroplasty. *J Am Acad Orthop Surg*. 1998;6(5):308-315.
22. Gaspar MP, Lou J, Kane PM, Jacoby SM, Osterman AL, Culp RW. Complications Following Partial and Total Wrist Arthroplasty: A Single-Center Retrospective Review. *J Hand Surg*. 2016;41(1):47-53.e4. doi:10.1016/j.jhsa.2015.10.021
23. Vance MC, Packer G, Tan D, Crisco JJT, Wolfe SW. Midcarpal hemiarthroplasty for wrist arthritis: rationale and early results. *J Wrist Surg*. 2012;1(1):61-68. doi:10.1055/s-0032-1323644
24. Frisbie DD, Cross MW, McIlwraith CW. A comparative study of articular cartilage thickness in the stifle of animal species used in human pre-clinical studies compared to articular cartilage thickness in the human knee. *Vet Comp Orthop Traumatol VCOT*. 2006;19(3):142-146.
25. Pearce AI, Richards RG, Milz S, Schneider E, Pearce SG. Animal models for implant biomaterial research in bone: a review. *Eur Cell Mater*. 2007;13:1-10. doi:10.22203/ecm.v013a01
26. Pond MJ, Nuki G. Experimentally-induced osteoarthritis in the dog. *Ann Rheum Dis*. 1973;32(4):387-388. doi:10.1136/ard.32.4.387
27. Kamekura S, Hoshi K, Shimoaka T, et al. Osteoarthritis development in novel experimental mouse models induced by knee joint instability. *Osteoarthritis Cartilage*. 2005;13(7):632-641. doi:10.1016/j.joca.2005.03.004
28. Hayami T, Pickarski M, Zhuo Y, Wesolowski GA, Rodan GA, Duong LT. Characterization of articular cartilage and subchondral bone changes in the

rat anterior cruciate ligament transection and meniscectomized models of osteoarthritis. *Bone*. 2006;38(2):234-243. doi:10.1016/j.bone.2005.08.007
29. Hsia AW, Emami AJ, Tarke FD, et al. Osteophytes and fracture calluses share developmental milestones and are diminished by unloading. *J Orthop Res Off Publ Orthop Res Soc*. 2018;36(2):699-710. doi:10.1002/jor.23779
30. Onur TS, Wu R, Chu S, Chang W, Kim HT, Dang ABC. Joint instability and cartilage compression in a mouse model of posttraumatic osteoarthritis. *J Orthop Res Off Publ Orthop Res Soc*. 2014;32(2):318-323. doi:10.1002/jor.22509
31. Yoshioka M, Coutts RD, Amiel D, Hacker SA. Characterization of a model of osteoarthritis in the rabbit knee. *Osteoarthritis Cartilage*. 1996;4(2):87-98. doi:10.1016/s1063-4584(05)80318-8
32. Oláh T, Cucchiarini M, Madry H. Subchondral bone remodeling patterns in larger animal models of meniscal injuries inducing knee osteoarthritis - a systematic review. *Knee Surg Sports Traumatol Arthrosc Off J ESSKA*. 2023;31(12):5346-5364. doi:10.1007/s00167-023-07579-6
33. Bansal S, Miller LM, Patel JM, et al. Transection of the medial meniscus anterior horn results in cartilage degeneration and meniscus remodeling in a large animal model. *J Orthop Res Off Publ Orthop Res Soc*. 2020;38(12):2696-2708. doi:10.1002/jor.24694
34. Pinette MP, Molino J, Proffen BL, Murray MM, Fleming BC. Effects of Male and Female Sex on the Development of Posttraumatic Osteoarthritis in the Porcine Knee After Anterior Cruciate Ligament Surgery. *Am J Sports Med*. 2022;50(9):2417-2423. doi:10.1177/03635465221102118
35. Behrends DA, Khendek L, Gao C, Zayed N, Henderson JE, Martineau PA. Characterization of a Pre-Clinical Mini-Pig Model of Scaphoid Non-Union. *J Funct Biomater*. 2015;6(2):407-421. doi:10.3390/jfb6020407
36. Stoeckl BD, Zlotnick HM, Farrell MJ, et al. The porcine accessory carpal bone as a model for biologic joint replacement for trapeziometacarpal osteoarthritis. *Acta Biomater*. 2021;129:159-168. doi:10.1016/j.actbio.2021.05.011
37. Altieri MK, Badida R, Vaughan QM, Molino J, Akelman E, Crisco JJ. Biomechanical evaluation of the porcine carpus as a potential preclinical animal model for the human carpus. *J Biomech*. 2024;177:112429. doi:10.1016/j.jbiomech.2024.112429
38. Fleming BC, Hulstyn MJ, Oksendahl HL, Fadale PD. Ligament injury, reconstruction, and osteoarthritis. *Curr Opin Orthop*. 2005;16:354-362.
39. Gabay O, Gabay C. Hand osteoarthritis: New insights. *Jt Bone Spine Rev Rhum*. Published online August 4, 2012. doi:10.1016/j.jbspin.2012.06.011
40. Kwok WY, Vliet Vlieland TPM, Rosendaal FR, Huizinga TWJ, Kloppenburg M. Limitations in daily activities are the major determinant of reduced health-related quality of life in patients with hand osteoarthritis. *Ann Rheum Dis*. 2011;70(2):334-336. doi:10.1136/ard.2010.133603
41. Nakasa T, Ikuta Y, Kawabata S, Sakurai S, Moriwaki D, Adachi N. Development of osteophytes and joint space narrowing is associated with cartilage degeneration of the osteochondral fragment in the osteochondral

lesion of the talus. *J Orthop Sci Off J Jpn Orthop Assoc*. 2024;29(5):1242-1247. doi:10.1016/j.jos.2023.08.013
42. Nagaosa Y, Lanyon P, Doherty M. Characterisation of size and direction of osteophyte in knee osteoarthritis: a radiographic study. *Ann Rheum Dis*. 2002;61(4):319-324. doi:10.1136/ard.61.4.319
43. Ozdemir F, Tukenmez O, Kokino S, Turan FN. How do marginal osteophytes, joint space narrowing and range of motion affect each other in patients with knee osteoarthritis. *Rheumatol Int*. 2006;26(6):516-522. doi:10.1007/s00296-005-0016-0
44. Vaughan QM, Morton AM, Moore D, Akelman E, Crisco JJ. Development of small bone implants using a mean shape bone in a porcine model for carpal bone replacement. *Proc Inst Mech Eng [H]*. Published online July 24, 2025:9544119251355382. doi:10.1177/09544119251355382
45. Badida R, Garcia-Lopez E, Sise C, Moore D, Crisco J. An Approach to Robotic Testing of the Wrist Using 3-D Imaging and a Hybrid Control Strategy. *J Biomech Eng*. 2020;142(6):064501. doi:10.1115/1.4046050
46. Morton AM, Akhbari B, Moore DC, Crisco JJ. Osteophyte volume calculation using dissimilarity-excluding Procrustes registration of archived bone models from healthy volunteers. *J Orthop Res Off Publ Orthop Res Soc*. 2020;38(6):1307-1315. doi:10.1002/jor.24569
47. Alyassin AM, Lancaster JL, Downs JH, Fox PT. Evaluation of new algorithms for the interactive measurement of surface area and volume. *Med Phys*. 1994;21(6):741-752. doi:10.1118/1.597333
48. Eberly D, Lancaster J, Alyassin A. On gray scale image measurements: II. Surface area and volume. *CVGIP Graph Models Image Process*. 1991;53(6):550-562. doi:10.1016/1049-9652(91)90005-5
49. Kalshoven JM, Badida R, Morton AM, Molino J, Crisco JJ. Do osteophytes alter thumb carpometacarpal Biomechanics? a preliminary in vitro study. *J Biomech*. 2024;176:112333. doi:10.1016/j.jbiomech.2024.112333
50. Crisco JJ, Morton AM, Moore DC, Kahan LG, Ladd AL, Weiss APC. Osteophyte growth in early thumb carpometacarpal osteoarthritis. *Osteoarthritis Cartilage*. 2019;27(9):1315-1323. doi:10.1016/j.joca.2019.05.008
51. Oura K, Moritomo H, Kataoka T, et al. Three-dimensional analysis of osteophyte formation on distal radius following scaphoid nonunion. *J Orthop Sci Off J Jpn Orthop Assoc*. 2017;22(1):50-55. doi:10.1016/j.jos.2016.06.018
52. de Raedt S, Stilling M, van de Giessen M, Streekstra GJ, Vos FM, Hansen TB. A three-dimensional analysis of osteoarthritic changes in the thumb carpometacarpal joint. *J Hand Surg Eur Vol*. 2013;38(8):851-859. doi:10.1177/1753193412466764
53. Ranota P, Seltser A, Suh N, Grewal R, MacDermid JC, Lalone E. The Effect of Malunited Scaphoid Fractures on Joint Congruency. *J Hand Surg*. 2021;46(11):1024.e1-1024.e8. doi:10.1016/j.jhsa.2021.02.020
54. Ten Berg PWL, Heeg E, Strackee SD, Streekstra GJ. Joint Space Narrowing in Patients With Pisotriquetral Osteoarthritis. *Hand N Y N*. 2017;12(5):490-492. doi:10.1177/1558944716677542

55. Sugiyanto S, Fatimah F, Setia Budi W, Suwondo A, Suyanto H. Comparison of Joint Space Width Determinations in Grade I and II Knee Osteoarthritis Patients Using Manual and Automatic Measurements. *J Biomed Phys Eng*. 2021;11(5):613-620. doi:10.31661/jbpe.v0i0.1912-1003
56. Das Neves Borges P, Vincent TL, Marenzana M. Automated assessment of bone changes in cross-sectional micro-CT studies of murine experimental osteoarthritis. *PLoS ONE*. 2017;12(3). doi:10.1371/journal.pone.0174294
57. Zhang L, Lin C, Jin J, Lin J, Li Z. Respective association of joint space narrowing and osteophyte formation with knee symptoms and function in China. *J Orthop Surg*. 2025;20(1):366. doi:10.1186/s13018-025-05727-x
58. Kessler S, Guenther KP, Puhl W. Scoring prevalence and severity in gonarthritis: the suitability of the Kellgren & Lawrence scale. *Clin Rheumatol*. 1998;17(3):205-209. doi:10.1007/BF01451048

Chapter 6: Conclusion

6.1. Summary

This thesis aimed to evaluate the potential of the Yucatan minipig (YMP) as a preclinical animal model of the human wrist for testing novel implant designs and therapeutics for the treatment of wrist pathologies. In this dissertation, we first developed a methodology to design a set of small bone implants for the radial carpal bone (RCB), which is homologous to the human scaphoid, and a predictive model to estimate which implant sizes would best fit animals included in an *in vivo* study without preoperative imaging. Next, we assessed the biomechanics of the YMP carpus under intact, injury, and post-implantation conditions. Finally, we investigated OA progression and severity following ligament injury and small bone replacement in an *in vivo* model.

For the 1st aim, we designed a set of 9 implants that characterized a range of animals of varying ages and weight, developed a predictive model to estimate the three best-fitting implant sizes based on animal age and weight, and established a surgical approach for optimal implant fixation. Regression analyses demonstrated a strong relationship between animal age, weight, and RCB volume. Model performance was evaluated in 4 *in vivo* animals by comparing model-predicted and surgeon-selected implants to the explanted bone using surface distance calculations. Distances between the model-predicted implant and the explanted bone were greater than those for the surgeon-selected implant. This suggests that the model overestimated implant size for the *in vivo* cohort.

For the 2nd aim, we quantified biomechanics, specifically multidirectional range of motion (ROM), pronosupination ROM, and translational ROM, of 9 YMP carpi

in vitro under ligament transected, RCB resection, and small bone replacement conditions. The greatest ROM was observed in the ulnar flexion direction, and overall carpus ROM increased relative to intact across all conditions in the four primary motion directions, particularly in radial deviation and extension. Supination at neutral increased relative to intact for the no RCB and RCBH conditions, and at maximum ROM, supination increased for all conditions (ALC, No RCB, RCBH). In contrast, pronation remained unchanged across conditions at both neutral and maximum ROM. No differences were observed in volar or dorsal translation relative to intact.

For the 3rd aim, we assessed osteoarthritis progression through serial gait analysis during a 12-week *in vivo* study and evaluated severity at study completion using osteophyte volume, joint space measurements, and histological analysis following either ligament injury (LI) or small bone replacement (SBR). The SBR group exhibited greater gait asymmetry at all postoperative timepoints for maximum force, impulse, and stance time compared to the LI group, while stride velocity remained unchanged. Osteophyte volume was greater in the SBR group in seven of twelve bones, joint space did not differ between limbs or across groups, and SBR operated limbs demonstrated greater cartilage degeneration than LI operated limbs.

The presented work makes the following contributions to the literature on the YMP as an animal model for the human wrist:

- Established a predictive model for estimating bone size based on animal age and weight without the need for preoperative imaging.[1]

- Established an *in vitro* methodology for quantifying the ROM, pronosupination, and volar-dorsal translation of the YMP carpus.[2]
- Identified that the YMP carpus has an elliptical-shaped ROM envelope similar to that of the human wrist.[2]
- Established a surgical approach for small bone implant fixation.[3]
- Demonstrated the feasibility of the YMP as a model of the human wrist for investigating osteoarthritis progression following wrist injury and implant treatment, as evidenced by osteophyte development and cartilage damage following the *in vivo* study.[3]

6.2. Implications and Clinical Significance

The results of these studies characterize the translational potential of the YMP as a preclinical animal model for the human wrist and highlight its relevance for the development and testing of novel therapeutics for wrist osteoarthritis. Characterization of the *in vitro* biomechanics of the YMP carpus enables direct comparison with human wrist biomechanics, despite the limited extension and the weightbearing function of the carpus. Furthermore, the response of the YMP carpus to modeled ligament injury, a common precursor to osteoarthritis, and to small bone replacement, a promising surgical treatment, provides valuable insight into what factors may influence treatment success. The ability to detect changes in gait, osteophyte progression, and cartilage degeneration in the YMP model will help identify optimal implant features, such as material and shape, for treating pathologies of the human wrist.

6.3. Limitations

Several limitations should be considered when interpreting these results. First, the Yucatan minipig (YMP) is a weight-bearing animal, placing approximately 60% of its weight on the forelimbs,[2] and thus represents a worst-case loading scenario for the human wrist. For Aim 1, the predictive model used to estimate bone size from animal age and weight overestimated bone volume by approximately 10%.[1] For aim 2, it remains unclear whether sufficient instability was induced during *in vitro* testing; although ROM increased relative to intact conditions, increases in the primary directions, specifically extension and radial deviation, were limited to at most 8°. Furthermore, due to the increased flexion of the YMP carpus, testing had to be manually stopped, primarily in the ulnar flexion direction, limiting accurate ROM measurement in those directions. For aim 3, imitations include a small sample size, which warrants cautious interpretation despite observed significant differences in gait, osteophyte volume, and histopathology. The short study duration (12 weeks) may explain the absence of differences in gait and joint distance, as well as the subtle osteophyte formation and cartilage damage observed in the LI group. Additionally, the onset and progression of osteoarthritis could not be fully characterized due to the lack of available computed tomography imaging throughout the study. Finally, cartilage damage in the SBR group was evaluated using only a single material (Cobalt–Chrome).

6.4. Future Directions

There are several opportunities to build upon the work presented in this dissertation. First, a model was developed to predict carpal bone size using animal age and weight; however, the model overestimates bone volume because each dimension (volar–dorsal, proximal–distal, radial–ulnar) is treated as independent, despite the interdependence of these dimensions in collectively determining bone volume. Future work should focus on improving the model to reduce this overestimation.

Additionally, while the biomechanics of the YMP carpus under injured and implant conditions were characterized, the motion of individual carpal bones was not determined. Quantifying bone kinematics across multiple degrees of freedom could determine whether the YMP carpus replicates human wrist motion during intact and following ligament injury.

For the *in vivo* study, extending the study duration may better capture the development of osteoarthritis, as limited evidence of gait asymmetry, joint distance, and cartilage damage was observed in the LI group. Finally, evaluating a broader range of implant materials could help identify those that minimize cartilage damage.

6.5. References

1. Vaughan QM, Morton AM, Moore D, Akelman E, Crisco JJ. Development of small bone implants using a mean shape bone in a porcine model for carpal bone replacement. *Proc Inst Mech Eng [H]*. Published online July 24, 2025:9544119251355382. doi:10.1177/09544119251355382
2. Vaughan QM, Badida R, Molino J, Akelman E, Crisco JJ. In Vitro Biomechanics of the Yucatan Minipig Carpus After Ligament Transection, Bone Resection, and Small Bone Replacement. Published online Forthcoming.
3. Vaughan QM, Morton AM, Moore DC, Molino J, Akelman E, Crisco JJ. Small Bone Replacement Leads to Greater Gait Asymmetry, Cartilage Damage, and Osteophyte Formation Than Ligament injury in a Porcine Wrist Model. Published online Forthcoming.
4. Kaiser EE, Waters ES, Fagan MM, et al. Characterization of tissue and functional deficits in a clinically translational pig model of acute ischemic stroke. *Brain Res*. 2020;1736:146778. doi:10.1016/j.brainres.2020.146778
5. Altieri MK, Badida R, Vaughan QM, Molino J, Akelman E, Crisco JJ. Biomechanical evaluation of the porcine carpus as a potential preclinical animal model for the human carpus. *J Biomech*. 2024;177:112429. doi:10.1016/j.jbiomech.2024.112429

Appendix

Chapter 3 Supplementary Data

Supplementary Table 3.1. Estimated marginal mean ROM (°) (95% confidence interval) for each direction of motion by condition during multidirectional testing.

Direction	Condition			
	Intact	ALC	No RCB	RCBH
EX0	9.41 (7.87, 11.24)	17.43 (14.23, 21.34)*	16.84 (13.54, 20.94)*	18.45 (14.94, 22.78)*
FE0	40.77 (23.62, 70.37)	39.61 (21.01, 74.68)	37.58 (29.85, 47.31)	38.38 (27.47, 53.63)
RD0	3.33 (2.46, 4.51)	9.95 (6.73, 14.70)*	10.81 (7.44, 15.71)*†	11.24 (7.56, 16.72)*
RE15	3.45 (2.54, 4.69)	10.10 (6.91, 14.75)*	10.96 (7.60, 15.79)*†	11.34 (7.64, 16.85)*
RE30	3.86 (2.82, 5.29)	10.34 (7.20, 14.86)*	11.24 (7.91, 15.97)*†	11.53 (7.75, 17.14)*
RE45	4.85 (3.54, 6.65)	10.78 (7.70, 15.09)*	11.79 (8.50, 16.36)*†	11.91 (8.01, 17.73)*
RE60	7.01 (5.07, 9.69)	11.72 (8.72, 15.77)*	12.96 (9.67, 17.37)*†	13.12 (9.06, 18.90)*
RE75	10.35 (7.71, 13.88)	14.31 (11.01, 18.61)	15.83 (12.49, 20.05)	16.91 (13.58, 21.06)
RF15	3.42 (2.53, 4.62)	9.85 (6.61, 14.67)*	10.78 (12.49, 20.05)*†	11.20 (7.52, 16.69)*
RF30	3.74 (2.76, 5.07)	9.81 (6.56, 14.68)*	10.85 (7.45, 15.82)*†	11.21 (7.50, 16.74)*
RF45	4.52 (3.37, 6.08)	9.88 (6.62, 14.75)*	11.17 (7.72, 16.15)*†	11.36 (7.59, 16.98)*
RF60	6.15 (4.57, 8.28)	10.32 (7.06, 15.10)*	12.20 (8.69, 17.14)*†	12.09 (8.26, 17.70)*
RF70	8.61 (6.40, 11.60)	11.40 (8.02, 16.21)	14.56 (10.76, 19.70)*†	13.77 (10.03, 18.90)*†
RF75	10.89 (8.07, 14.72)	13.02 (9.13, 18.54)	17.62 (12.89, 24.08)†	15.60 (11.84, 20.56)*
RF80	14.78 (10.85, 20.13)	17.96 (10.58, 30.49)	24.22 (15.97, 36.72)†	18.86 (14.62, 24.33)*
UD0	6.20 (5.01, 7.67)	10.96 (7.85, 15.30)	10.59 (7.69, 14.57)	11.41 (7.77, 16.77)
UE15	5.32 (4.36, 6.49)	10.82 (7.73, 15.12)*	10.43 (7.48, 14.55)*	11.09 (7.48, 16.46)*

UE30	5.60 (4.52, 6.94)	11.17 (8.13, 15.35)*	10.72 (7.72, 14.90)*	11.33 (7.77, 16.53)*
UE45	4.80 (3.50, 6.58)	11.87 (8.80, 16.01)*	11.38 (8.28, 15.64)*	11.96 (8.38, 17.06)*
UE60	6.64 (5.44, 8.10)	13.10 (9.89, 17.35)*	12.60 (9.27, 17.12)*	13.16 (9.46, 18.31)*
UE75	7.69 (6.68, 8.86)	15.29 (11.90, 19.63)*	14.72 (11.19, 19.36)*	15.40 (11.55, 20.54)*
UF15	6.81 (5.61, 8.26)	11.86 (8.78, 16.03)*	11.46 (8.69, 15.11)*	12.55 (8.98, 17.54)*
UF30	9.55 (7.79, 11.70)	14.34 (11.18, 18.38)	13.72 (11.07, 17.01)	15.56 (12.17, 19.90)*
UF45	12.69 (9.17, 17.55)	21.13 (16.79, 26.59)*	20.13 (16.73, 24.21)*	24.17 (19.59, 29.82)*
UF60	38.94 (32.14, 47.19)	52.70 (41.84, 66.39)	52.84 (42.14, 66.25)*	66.35 (53.34, 82.28)*
UF70	84.95 (69.03, 104.53)	93.73 (82.53, 106.45)	103.74 (84.64, 127.15)	97.01 (73.12, 128.70)
UF75	87.16 (73.82, 102.90)	109.41 (95.73, 125.04)*	105.23 (90.38, 122.52)	95.30 (79.76, 113.86)
UF80	77.81 (55.79, 108.51)	86.55 (65.06, 115.15)	81.46 (70.07, 94.70)	85.23 (65.18, 111.45)

* p<0.05 to intact
† p<0.05 to ALC

Supplementary Table 3.2. Pronation/supination ROM (°) in neutral by condition.

Direction	Intact	ALC	No RCB	RCBH
Pronation	19.54 (16.18, 23.59)	21.20 (16.43, 27.36)	21.62 (17.18, 27.21)	21.42 (15.80, 29.05)
Supination	8.25 (6.45, 10.55)£	12.55 (8.84, 17.82)	15.54 (11.70, 20.64)*†	15.21 (10.66, 21.70)*†

* p<0.05 to intact
† p<0.05 to ALC
£ p<0.05 to pronation

Supplementary Table 3.3. Stiffness (Nm/°) in pronation/supination in neutral by condition.

Direction	Intact	ALC	No RCB	RCBH
Pronation	0.18 (0.14, 0.21)	0.13 (0.11, 0.15)*	0.12 (0.11, 0.14)*	0.14 (0.13, 0.16)
Supination	0.22 (0.21, 0.23)£	0.17 (0.15, 0.20)*£	0.17 (0.16, 0.18)*£	0.19 (0.16, 0.21)*£

* p<0.05 to intact
† p<0.05 to ALC
£ p<0.05 to pronation

Supplementary Table 3.4. Pronation/supination ROM (°) in UF75 by condition.

Direction	Intact	ALC	No RCB	RCBH
Pronation	13.07 (8.80, 19.40)	20.31 (13.46, 30.63)	18.40 (12.10, 27.97)	20.40 (13.95, 29.85)
Supination	19.39 (17.02, 22.08)	28.85 (23.68, 35.13)*	29.36 (24.76, 34.81)*	28.20 (22.23, 35.75)*

* p<0.05 to intact
† p<0.05 to ALC
£ p<0.05 to pronation

Supplementary Table 3.5. Stiffness (Nm/°) in pronation/supination in UF75 by condition.

Direction	Intact	ALC	No RCB	RCBH
Pronation	0.17 (0.13, 0.20)	0.11 (0.08, 0.14)	0.11 (0.09, 0.14)	0.11 (0.09, 0.14)
Supination	0.16 (0.14, 0.19)	0.14 (0.13, 0.16)	0.14 (0.11, 0.16)	0.14 (0.10, 0.18)

* p<0.05 to intact
† p<0.05 to ALC
£ p<0.05 to pronation

Supplementary Table 3.6. Volar/dorsal translations (mm) by condition.

Direction	Intact	ALC	No RCB	RCBH
Dorsal	6.48 (5.44, 7.73)	5.36 (4.00, 7.18)	5.71 (4.02, 8.12)	5.06 (3.41, 7.52)
Volar	7.60 (6.15, 9.39)	10.23 (8.59, 12.17)£	10.02 (7.93, 12.65)	10.54 (8.21, 13.54)

* p<0.05 to intact
† p<0.05 to ALC

£ p<0.05 to dorsal

Supplementary Table 3.7. Stiffness (N/mm) in volar/dorsal translations by condition.

Direction	Intact	ALC	No RCB	RCBH
Dorsal	7.38 (5.46, 9.97)	7.47 (5.38, 10.38)	7.32 (5.18, 10.33)	7.75 (5.46, 11.00)
Volar	6.71 (4.58, 9.83)	6.25 (4.35, 8.97)*£	6.23 (4.51, 8.59)£	14.81 (7.22, 30.38)

* p<0.05 to intact
† p<0.05 to ALC
£ p<0.05 to dorsal

Chapter 5 Supplementary Data

Supplementary Table 5.1. The average of osteophyte volume (mm^3), osteophyte volume as a percentage of contralateral bone volume (%), and total bone volume for each bone model in the left and right carpus, comparing the control (n=6), ligament injury group (n=4) and implant group (n=4).

	Osteophyte Volume (mm^3)			% Osteophyte Volume (op vol/left bone vol)			Right Bone Volume (mm^3)			Left Bone Volume (mm^3)		
	Cont	Lig Inj	Imp	Cont	Lig Inj	Imp	Cont	Lig Inj	Imp	Cont	Lig Inj	Imp
CB2	15.5 ± 12.0	29.5 ± 12.4	105.4 ± 6.7	4.5 ± 3.4	7.2 ± 2.8	27.3 ± 4.2	339.2 ± 27.6	417.8 ± 79.1	481.2 ± 46.9	347.6 ± 30.3	409.4 ± 67.7	392.2 ± 57.5
CB3	52.1 ± 20.0	136.1 ± 26.4	325.5 ± 114.9	3.0 ± 1.0	7.0 ± 1.7	17.4 ± 6.0	1665.9 ± 149.5	2085.7 ± 367.8	2154.9 ± 407.8	1686.9 ± 138.5	1990.8 ± 372.4	1871.1 ± 328.4
CB4	53.8 ± 24.4	144.2 ± 55.1	428.9 ± 64.2	2.5 ± 1.2	5.5 ± 1.4	17.6 ± 3.8	2155.9 ± 103.0	2656.2 ± 473.6	2801.2 ± 406.9	2187.5 ± 127.1	2565.4 ± 419.6	2476.5 ± 352.3
ICB	123.0 ± 117.7	215.3 ± 85.2	580.2 ± 220.1	5.0 ± 4.9	7.1 ± 1.8	21.5 ± 9.3	2539.1 ± 250.3	3114.5 ± 588.9	3277.2 ± 512.7	2531.7 ± 226.3	2963.9 ± 526.9	2753.6 ± 450.2
UCB	106.9 ± 98.4	159.2 ± 97.6	347.4 ± 180.6	6.5 ± 6.0	7.8 ± 3.4	18.8 ± 11.7	1704.0 ± 122.0	2066.5 ± 493.4	2231.6 ± 304.0	1702.4 ± 191.9	1946.8 ± 417.5	1930.3 ± 307.6
RAD	233.9 ± 86.6	210.5 ± 46.0	562.6 ± 328.4	3.4 ± 1.3	2.3 ± 0.6	6.4 ± 4.4	7025.4 ± 515.2	9230.1 ± 547.1	9295.7 ± 513.2	6974.3 ± 487.9	9069.2 ± 679.9	9101.1 ± 721.2
ULNA	132.8 ± 91.0	80.1 ± 20.7	102.7 ± 74.9	6.2 ± 4.3	6.3 ± 1.7	9.7 ± 8.6	2291.4 ± 352.2	1674.0 ± 135.7	1519.3 ± 227.0	2249.2 ± 373.9	1277.8 ± 144.2	1200.1 ± 221.1
MC2	14.8 ± 5.0	27.0 ± 6.5	48.1 ± 21.4	4.7 ± 1.3	10.4 ± 3.3	19.5 ± 11.7	307.3 ± 46.6	281.6 ± 17.8	303.6 ± 31.2	311.4 ± 44.5	265.4 ± 24.3	263.3 ± 41.4
MC3	70.9 ± 56.6	192.1 ± 150.9	254.6 ± 91.4	3.3 ± 2.7	9.0 ± 7.9	11.6 ± 4.7	2187.4 ± 153.8	2290.9 ± 155.4	1835.5 ± 1004.2	2154.9 ± 107.3	2260.7 ± 247.1	2224.4 ± 210.2
MC4	56.4 ± 38.8	105.0 ± 41.4	181.4 ± 55.3	3.7 ± 2.6	6.4 ± 3.0	11.5 ± 3.5	1563.7 ± 79.6	1611.3 ± 69.6	1263.6 ± 759.1	1552.9 ± 102.7	1667.8 ± 144.7	1585.5 ± 207.7
MC5	14.0 ± 17.4	17.1 ± 9.0	37.5 ± 13.0	4.1 ± 5.1	6.6 ± 3.3	13.5 ± 4.1	338.8 ± 52.7	262.0 ± 44.6	308.6 ± 30.9	353.5 ± 61.9	258.0 ± 42.1	274.9 ± 16.2
RCB	32.5 ± 28.4	256.1 ± 75.9		1.4 ± 1.2	10.9 ± 2.0		2150.0 ± 223.3	2526.6 ± 334.3		2320.9 ± 282.4	2316.1 ± 283.2	

Supplementary Table 5.2. Average percentage of osteophyte volume (± standard deviation), computed for each cube, corresponding to the anatomical location of the bone, for the ligament injury group (Lig Inj) and the small bone replacement group (Imp).

	CB2		CB3		CB4		ICB		UCB		RAD		ULNA		MC2		MC3		MC4		MC5		RCB	
	Lig Inj	Imp	Lig Inj	Imp	Lig Inj	Imp	Lig Inj	Imp	Lig Inj	Imp	Lig Inj	Imp	Lig Inj	Imp	Lig Inj	Imp	Lig Inj	Imp	Lig Inj	Imp	Lig Inj	Imp	Lig Inj	Imp
DorDistRad	1.1 ± 0.8	5.7 ± 3.4	1.0 ± 0.4	3.3 ± 1.7	0.8 ± 0.2	3.7 ± 1.9	0.8 ± 0.2	2.6 ± 1.2	0.8 ± 0.3	2.7 ± 1.9													2.7 ± 0.5	
DorDistUln	0.7 ± 0.5	1.9 ± 0.7	1.3 ± 0.4	2.5 ± 1.0	0.7 ± 0.3	2.7 ± 1.8	1.6 ± 0.9	4.9 ± 1.2	0.8 ± 0.3	1.1 ± 0.6													0.7 ± 0.1	
DorProxRad	0.9 ± 0.3	5.6 ± 1.7	0.8 ± 0.4	3.6 ± 1.5	0.8 ± 0.3	2.8 ± 1.0	1.3 ± 0.6	2.9 ± 2.0	0.9 ± 0.3	4.0 ± 1.9													2.0 ± 1.3	
DorProxUln	0.9 ± 0.4	2.0 ± 0.5	0.7 ± 0.6	3.1 ± 1.3	0.7 ± 0.3	1.7 ± 0.9	1.0 ± 0.6	3.1 ± 1.6	0.7 ± 0.3	1.5 ± 1.2													1.6 ± 0.4	
VolDistRad	0.8 ± 0.3	3.4 ± 1.5	0.7 ± 0.3	1.5 ± 0.8	0.5 ± 0.1	1.5 ± 1.1	0.6 ± 0.1	1.3 ± 0.4	1.4 ± 0.5	2.3 ± 2.3													0.9 ± 0.3	
VolDistUln	1.0 ± 0.3	2.3 ± 0.4	0.8 ± 0.2	1.3 ± 0.7	0.6 ± 0.3	1.7 ± 1.4	0.7 ± 0.2	1.6 ± 0.8	1.3 ± 0.9	2.0 ± 1.6													1.3 ± 0.3	
VolProxRad	0.9 ± 0.4	4.6 ± 2.1	0.5 ± 0.2	1.3 ± 0.7	0.5 ± 0.2	1.8 ± 0.7	0.6 ± 0.2	2.1 ± 1.5	0.6 ± 0.4	1.5 ± 1.1													1.1 ± 0.1	
VolProxUln	0.8 ± 0.3	1.8 ± 0.5	0.8 ± 0.2	0.8 ± 0.4	0.9 ± 0.4	1.6 ± 0.6	0.6 ± 0.1	3.0 ± 1.8	1.4 ± 0.9	3.8 ± 2.2													0.6 ± 0.03	
DorRad											0.4 ± 0.1	1.9 ± 1.6	0.5 ± 0.3	1.4 ± 1.7	0.8 ± 0.2	1.8 ± 1.8	0.8 ± 0.3	2.0 ± 1.4	0.9 ± 0.3	1.4 ± 0.3	0.6 ± 0.6	1.4 ± 0.7		
DorUln											0.2 ± 0.1	0.6 ± 0.2	0.4 ± 0.2	0.9 ± 0.9	1.2 ± 0.4	2.7 ± 0.8	0.7 ± 0.4	1.3 ± 1.0	0.4 ± 0.1	0.8 ± 0.3	1.0 ± 0.6	2.0 ± 1.2		
VolRad											0.5 ± 0.2	1.3 ± 1.3	0.6 ± 0.6	1.1 ± 1.0	1.4 ± 1.1	3.3 ± 2.6	0.9 ± 0.7	1.9 ± 0.7	0.5 ± 0.2	1.6 ± 0.6	0.5 ± 0.2	1.1 ± 0.7		
VolUln											0.3 ± 0.1	0.3 ± 0.3	1.2 ± 0.4	1.7 ± 1.5	1.9 ± 0.6	1.8 ± 1.1	1.0 ± 0.5	2.5 ± 1.4	0.9 ± 0.7	2.4 ± 0.9	0.4 ± 0.2	1.2 ± 0.6		

Supplementary Figure 5.1. Osteophyte models of the carpal bones for the ligament injury group (left column) and the small bone replacement group (right column), with colormaps depicting the distance (mm) from each osteophyte model to the surface of the corresponding contralateral bone model.

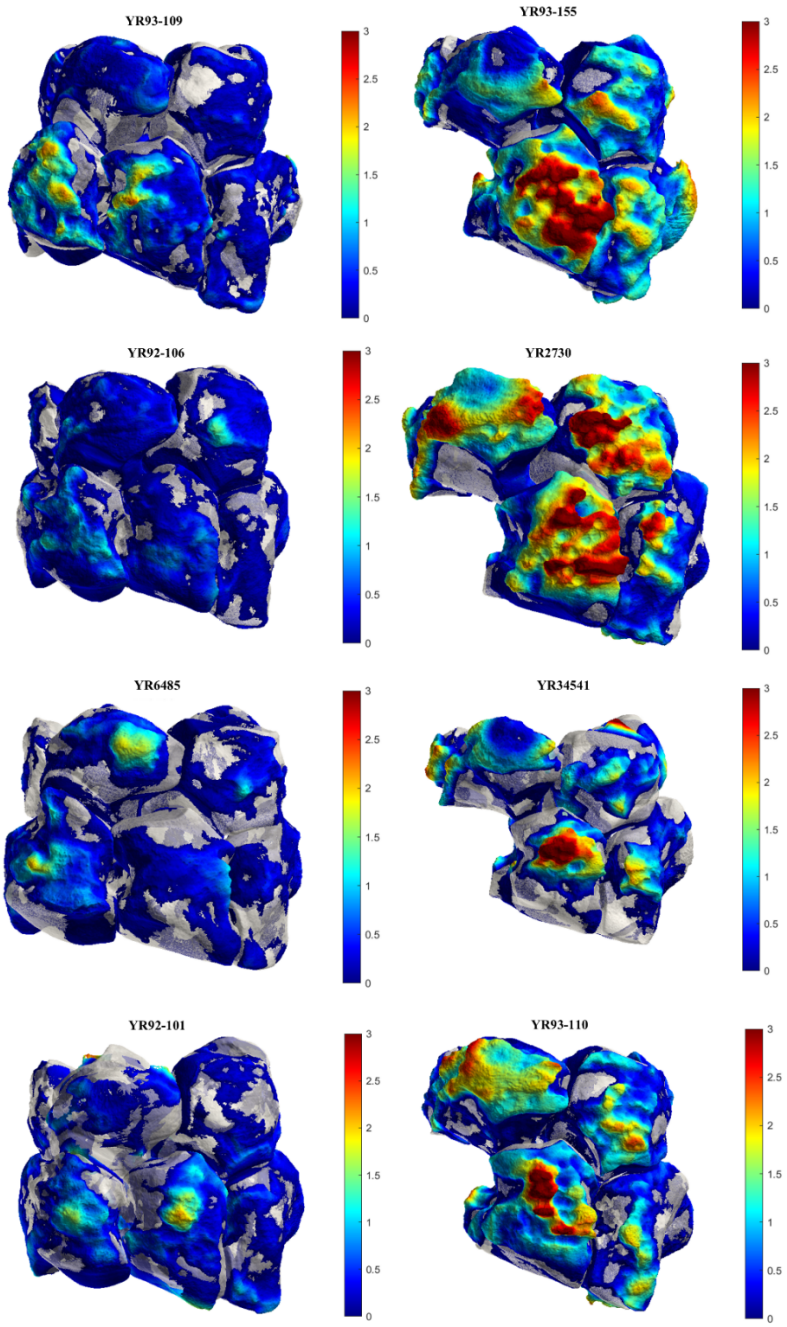

Supplementary Figure 5.2. Radial (left), dorsal (middle), and ulnar (right) views of a right YMP carpus following formalin fixation. Gapping is observed between the distal and proximal carpal rows, the proximal carpal row and the radius/ulna, suggesting the carpus was fixed in a minimally flexed orientation.